

Lattice Boltzmann Studies of Wetting and Spreading on Patterned Surfaces

Halim Kusumaatmaja

Balliol College



Department of Physics, The Rudolf Peierls Centre for Theoretical Physics
University of Oxford

Thesis submitted in partial fulfilment of the requirements for the degree of Doctor of Philosophy in the University of Oxford

· Trinity Term, 2008 ·

Lattice Boltzmann Studies of Wetting and Spreading on Patterned Surfaces

Halim Kusumaatmaja

Balliol College

Department of Physics, The Rudolf Peierls Centre for Theoretical Physics
University of Oxford

Thesis submitted in partial fulfilment of the requirements for the degree of Doctor of Philosophy in the University of Oxford

· Trinity Term, 2008 ·

ABSTRACT

Wetting and spreading are ubiquitous surface phenomena which occur when a liquid is brought into contact with a solid surface. They are part of Nature's toolbox in the functional adaptation of many biological systems and we often make use of them in our technological processes. Wetting is driven by surface forces, the so-called surface tensions, and it becomes increasingly important as the typical region occupied by the liquid becomes smaller. As miniaturisation of fluidic operations lead to surface structures on the micron and nanoscale, wetting phenomena become very rich, partly because the length scale of the surface heterogeneities is now comparable to the size of the system. This is the focal point of this thesis. We are interested in how micron-scale surface patterning can alter the wettability of the surface.

Two types of patterning are addressed in the thesis, chemical and topological. Both patternings lead to complex drop morphologies that depend sensitively on the parameters of the patterns, as well as the path by which the system is prepared. The contact angle of the drop is no longer uniquely determined, leading to a phenomenon called contact angle hysteresis, and the drop shape may differ considerably from a spherical cap. This anisotropy can, in return, be exploited for microfluidic operations. We show how appropriate patterns may be used to control drop size and polydispersity, as well as to enhance or slow down capillary filling.

Topological patterning may also lead to superhydrophobic behaviour. This can occur in two different ways. When a liquid drop is placed on a superhydrophobic surface, it can either be suspended on top of the corrugations or fill the space in between the posts. We discuss in particular how the apparent contact angle and the contact angle hysteresis are affected by the surface roughness in these two states, and investigate when a transition may occur from the suspended to the collapsed state as the drop evaporates.

Analytical descriptions of drop morphologies are often not possible and numerical modelling is needed. This is done using a mesoscale modelling technique called the lattice Boltzmann method. We present three models which may be used to model wetting phenomena: the liquid gas, the binary, and the binary liquid gas model and discuss the relative strengths and weaknesses of each approach.

CONTENTS

Acknowledgments	iv
Publications	v
1 Introduction	1
2 The Lattice Boltzmann Models	11
2.1 The Liquid Gas Model	12
2.1.1 Thermodynamics of the Fluid	12
2.1.2 Hydrodynamics of the Fluid	13
2.1.3 The Lattice Boltzmann Implementation	14
2.1.4 Boundary Conditions	16
2.2 The Binary Model	19
2.2.1 Thermodynamics and Hydrodynamics of the Fluid	19
2.2.2 The Lattice Boltzmann Implementation: Single Relaxation Time	20
2.2.3 The Lattice Boltzmann Implementation: Multiple Relaxation Time . .	21
2.3 The Binary Liquid Gas Model	25
2.4 Discussion	26
3 The Influence of Chemical Patterning on the Dynamics of Micron-scale Liquid Drops	28
3.1 Drop Dynamics on Chemically Striped Surfaces	29
3.1.1 Simulations	29
3.1.2 Experiments	30
3.1.3 Results	30
3.2 Controlling Drop Size and Polydispersity Using Chemically Patterned Surfaces	34
3.2.1 Sorting Drops by Size and Wetting Properties	36
3.2.2 Generating Monodisperse Drops	40
3.3 Discussion	41
4 Modelling Contact Angle Hysteresis on Patterned Surfaces	43
4.1 Two Dimensional Drop on a Chemically Patterned Surface	46
4.2 Three Dimensional Drop on a Chemically Patterned Surface	50
4.3 Two Dimensional Suspended Drop on a Topologically Patterned Surface . . .	60
4.4 Two Dimensional Collapsed Drop on a Topologically Patterned Surface . . .	62
4.5 Three Dimensional Suspended Drop on a Topologically Patterned Surface . .	65
4.6 Three Dimensional Collapsed Drop on a Topologically Patterned Surface . .	67
4.7 Discussion	70

5 The Collapse Transition on Superhydrophobic Surfaces	73
5.1 Drop Collapse in Two dimensions: Analytical Results	75
5.2 Drop Collapse in Two Dimensions: Lattice Boltzmann Simulations	79
5.3 Drop Collapse in Three Dimensions: Analytic Results for Circular Ridges . . .	81
5.4 Drop Collapse in Three Dimensions: Square Lattice of Hydrophobic Posts . . .	83
5.5 Discussion	86
6 Capillary Filling in Patterned Channels	88
6.1 Washburn's Law	89
6.2 Capillary Filling in Smooth Channels	90
6.2.1 Liquid Gas Model: The Evaporation-Condensation Problem	90
6.2.2 Binary Model	92
6.3 Capillary Filling in Patterned Channels	96
6.3.1 Two Dimensional Results	96
6.3.2 Three Dimensional Results	99
6.4 Discussion	101
7 Concluding Remarks	103
Bibliography	109

ACKNOWLEDGMENTS

First of all, I would like to thank my supervisor, Professor Julia Yeomans, for her help, guidance and endless patience throughout my stay in Oxford. I also benefitted greatly from discussions and exchange of ideas with many people: Professor Anna Balazs for all her encouragement and help, especially during my fourth year; Dr. Olivier Pierre Louis for proofreading parts of this thesis and for the many interesting discussions on wetting phenomena; Dr. Alexandre Dupuis for teaching me about lattice Boltzmann simulations; Dr. Chris Pooley for collaborating with me on the capillary filling problem and for the many discussions on improving the lattice Boltzmann implementations; Dr. Julien Leopoldes for performing the experiments on drop dynamics on chemically patterned surfaces; Dr. Dario Pisignano for performing the experiments on capillary filling; Matthew Blow for proof reading this thesis and for collaborating with me on the drop collapse problem; Robert Vrancken for collaborating with me on the spreading of drops on corrugated surfaces; Javier Montes for the useful discussions on contact angle hysteresis and contact angle multiplicity; and Gareth Alexander for the fruitful discussions on many topics, from research to undergraduate teaching.

On a personal note, I would like to thank my wonderful colleagues at Theoretical Physics, my fellow korfballers, basketballers and friends, for distracting me from work and for making my Oxford experience very enjoyable. Thank you for being my family in Oxford and thank you for all the great memories. I hope this is only the beginning of our life-long friendships.

Finally, a special thanks to my family, particularly my Mom and Dad. I would not have been able to write this thesis without their love and support. I am sorry I have been away from home for so long.

PUBLICATIONS

Most of the work presented in chapter 3, 4, 5 and 6 has been published in the following journals:

- H. Kusumaatmaja, J. Leopoldes, A. Dupuis, and J. M. Yeomans, “Drop Dynamics on Chemically Patterned Surfaces”, *Europhys. Lett.* **73**, 740 (2006).
- H. Kusumaatmaja and J. M. Yeomans, “Controlling Drop Size and Polydispersity Using Chemically Patterned Surfaces”, *Langmuir* **23**, 956 (2007).
- H. Kusumaatmaja and J. M. Yeomans, “Modeling Contact Angle Hysteresis on Chemically Patterned and Superhydrophobic Surfaces”, *Langmuir* **23**, 6019 (2007).
- H. Kusumaatmaja, M. L. Blow, A. Dupuis and J. M. Yeomans, “The Collapse Transition on Superhydrophobic Surfaces”, *Europhys. Lett.* **81**, 36003 (2008).
- H. Kusumaatmaja, C. M. Pooley, S. Girardo, D. Pisignano and J. M. Yeomans, “Capillary Filling in Patterned Channels”, *Phys. Rev. E* **77**, 067301 (2008).

Parts of the work contained in chapter 2 and 6 are currently being prepared for publication:

- C. M. Pooley, H. Kusumaatmaja and J. M. Yeomans, “Contact Line Dynamics in Binary Lattice Boltzmann Simulations”.

The author has also been involved in the following publications:

- H. Kusumaatmaja, A. Dupuis, and J. M. Yeomans, “Lattice Boltzmann Simulations of Drop Dynamics”, *Mathematics and Computers in Simulation* **72**, 160 (2006).
- J. M. Yeomans and H. Kusumaatmaja, “Modelling Drop Dynamics on Patterned Surfaces”, *Bulletin of the Polish Academy of Sciences, Technical Sciences* **55**, 203 (2007).
- H. Kusumaatmaja, R. J. Vrancken, C. W. M. Bastiaansen and J. M. Yeomans, “Anisotropic Drop Morphologies on Corrugated Surfaces”, *Langmuir* **24**, 7299 (2008).
- C. M. Pooley, H. Kusumaatmaja and J. M. Yeomans, “Modelling Capillary Filling Dynamics Using Lattice Boltzmann Simulations”, accepted for publication in *Eur. Phys. J. Special Topics* (2008).
- H. Kusumaatmaja and J. M. Yeomans, “Modelling Drop Dynamics and Wetting Phenomena Using the Lattice Boltzmann Methods”, a book chapter contribution to *Modelling of Complex Systems by Cellular Automata*, Springer (publisher), J. Kroc and P. M. A. Sloot (editors), in preparation.

CHAPTER 1

Introduction

“God created the solids, the devil their surfaces.”

- Wolfgang Pauli

When a liquid is brought into contact with a solid surface, the liquid will spread. The degree of the spreading depends on the surface chemistry: the competition between the interfacial energies of the solid, liquid, and gas. This concept was first proposed by Thomas Young [1] and Pierre-Simon Laplace [2] in 1805. Young and Laplace realised that when there is an interface between two materials, there is a specific energy, termed the interfacial energy, which is proportional to the number of molecules present at that interface. In other words, this energy is proportional to the surface area of the interface and the constant of proportionality is called the surface tension. Since in wetting phenomena we typically have a liquid, a solid and a surrounding gas, there are three types of surface tensions: the liquid-gas σ_{LG} , the gas-solid σ_{GS} and the liquid-solid σ_{LS} surface tensions.

As a consequence of this concept, liquid drops are spherical when they are in air, to minimise the surface energy. When they are in contact with a solid, the liquid-gas interface maintains a spherical cap profile and the angle at which the liquid drop joins the solid is called the contact angle θ , where

$$\cos \theta = \frac{\sigma_{GS} - \sigma_{LS}}{\sigma_{LG}}. \quad (1.1)$$

This equilibrium contact angle is often called the Young's angle. In the literature, a solid surface is called hydrophilic¹ when $\theta < 90^\circ$, neutrally wetting when $\theta = 90^\circ$ and hydrophobic when $\theta > 90^\circ$. This is illustrated in the schematic diagram shown in Fig. 1.1.

¹Strictly speaking, the terms hydrophilic and hydrophobic are appropriate only when the liquid is water. Nonetheless, in the literature, they are typically used irrespective of the types of liquid and gas.

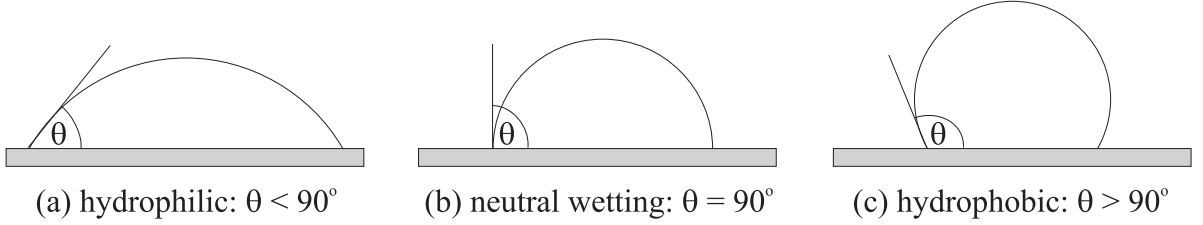


Figure 1.1: Schematic diagrams of a liquid drop on (a) a hydrophilic, (b) a neutrally wetting and (c) a hydrophobic surface.

Another important concept associated with the surface tension is the Laplace pressure. When crossing a curved interface, the pressure of the system on the two sides of the interface differs by

$$\Delta P = \sigma_{LG} \kappa, \quad (1.2)$$

where κ is the total curvature of the interface. In static or quasi-static situations, the Laplace pressure, and hence the curvature of the drop is constant. This is an important condition that will be useful later to help understand some of the morphologies we obtained from our simulations.

So far we have only considered surface tension effects and the majority of work we present here deals with systems where surface tension is the dominant force in the problem. It is therefore important to know when this approximation holds, in particular the typical length scale below which we can neglect gravity. The energy associated with surface tension scales as $\sigma_{LG} R^2$, where R is the size of the drop. On the other hand, the gravitational energy of a drop scales as $\Delta n g R^4$, where Δn is the density difference between the liquid and gas phase and g is the gravitational acceleration. Therefore we can safely neglect gravity if $\sigma_{LG} R^2 \gg \Delta n g R^4$, or alternatively when the size of the drop is much smaller than the so-called capillary length, λ_C , where

$$\lambda_C = \sqrt{\frac{\sigma_{LG}}{\Delta n g}}. \quad (1.3)$$

Putting the typical values of $\sigma_{LG} = 10^{-2} \text{ N.m}^{-1}$, $\Delta n = 10^3 \text{ kg.m}^{-3}$ and $g = 10 \text{ m.s}^{-2}$, we find $\lambda_C \sim 1 \text{ mm}$. Since we are interested in systems where the typical length scale is of order $10 - 100 \mu\text{m}$, we shall neglect gravity when considering the static or quasi-static behaviours of the drops. We also neglect thermal fluctuations and line tension effects, which may become an important effect if the size of the system is nanoscopic.

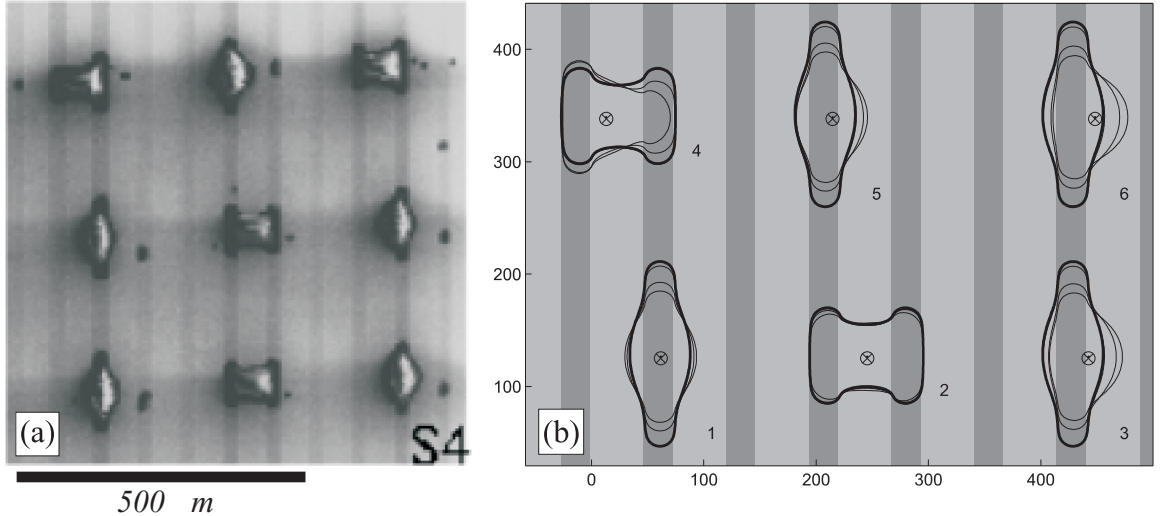


Figure 1.2: Drop spreading on a chemically striped surface. (a) Scanning electron micrographs of inkjet drops. (b) Numerical simulations of drops hitting the surface at various impact points indicated by encircled crosses. For each drop the bold and faint lines represent the extent of the drop at equilibrium and at intermediate times, respectively. Relatively hydrophilic and hydrophobic stripes appear dark and pale, respectively. The figures are taken from [6].

Another important length scale we need to consider is that of the surface heterogeneities. Real solids are chemically heterogeneous and rough, and are thus far from being the ideally smooth and homogeneous surface we have assumed when deriving Eq. (1.1). These heterogeneities are often at micron-scale, although some recent works [3–5] suggest that nanometric scale heterogeneities may play an important role too, especially on superhydrophobic surfaces. In this thesis, however, we shall neglect the latter and concentrate mainly on the effect of micron-scale heterogeneities. We are typically interested in wetting phenomena on modelled patterned surfaces, where the surfaces are regularly patterned either chemically or topologically.

The presence of these imperfections has several important consequences. Firstly, they may qualitatively change the shape of the drop from a spherical cap. Fig. 1.2 shows experimental and simulation results of drops spreading on a chemically striped surface [6]. Depending on the initial conditions, the drop can take two final configurations, the so-called ‘diamond’ and ‘butterfly’ shapes. Both configurations differ considerably from the spherical cap shape, which occurs when the surface is smooth. The presence of multiple stable configurations also introduces us to the concept of energy barrier and multiple local minima, which turns out to be extremely important for understanding the behaviours of drops spreading on patterned surface.

For drops on such patterned surfaces, measuring the contact angle of the drop becomes problematic, since its value can vary considerably along the contact line. In many cases, however, the drop shape remains roughly spherical and the contact angle is still a well-defined quantity. Here the effect of surface heterogeneities are summarised in two quantities: the effective (or apparent) contact angle and the contact angle hysteresis. The effective contact angle measures the average properties of the surface, while the contact angle hysteresis measures the variability of the contact angle measurements. The largest static angle is called the advancing contact angle, θ_A , while the smallest angle is called the receding contact angle, θ_R . The contact angle hysteresis is defined as $\Delta\theta = \theta_A - \theta_R$. In chapter 4, the concept of effective contact angle and contact angle hysteresis will be discussed in details for both chemically patterned and superhydrophobic surfaces.

Superhydrophobic Surfaces

Superhydrophobic surfaces are perhaps the prime example of how surface heterogeneities can alter the wettability of a surface. When a liquid drop spreads on a smooth hydrophobic surface, the highest contact angle one can achieve is of order $120 - 130^\circ$ [7]. For example, this may be attainable when a water drop spreads on fluorinated solids.

When the hydrophobic surface is made rougher, however, higher contact angles are possible. Several natural materials exhibit this so-called superhydrophobicity, with contact angles between 150° and 165° . The most famous example is the leaves of lotus plant [8], shown in Fig. 1.3(a). Here, there are two scales of roughness of $10\ \mu m$ and $1\ \mu m$, and these bumps promote superhydrophobicity by trapping the gas phase in between the corrugations. This behaviour is actually quite common in plants [8] and many animals, for example, water strider legs [9], butterfly wings [10] and duck feathers [11], have also been shown to exhibit superhydrophobicity.

Recently, many research groups have been able to reproduce superhydrophobic surfaces. The earlier superhydrophobic surfaces were made by patterning hydrophobic surfaces by regular posts of the same material [12]. This is shown, for example, in Fig. 1.3(b). However, it has been recently shown than neither the regular patterning nor the intrinsic hydrophobicity [13,14] of the material is an absolute requirement to promote superhydrophobicity. Several authors have even shown the possibility of fabricating multiscale roughness [3–5] to mimic

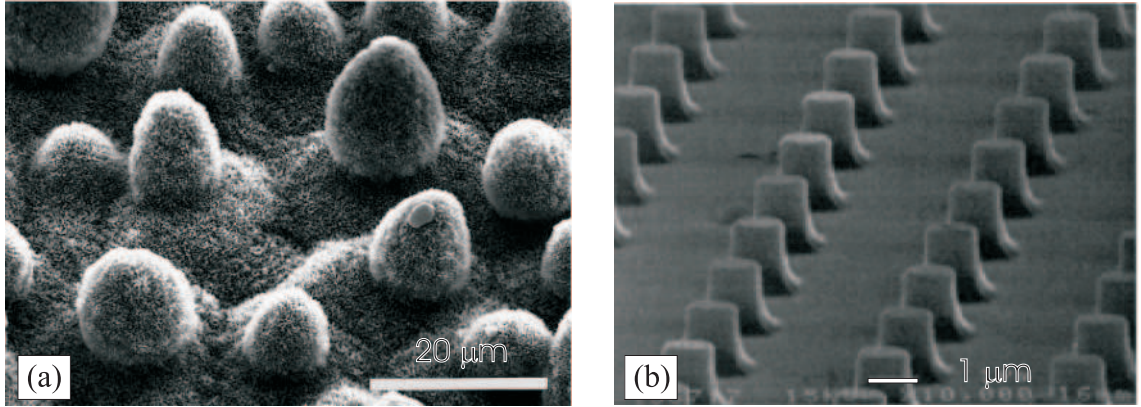


Figure 1.3: Scanning electron micrographs of (a) a lotus leaf [8] and (b) a hydrophobic surface patterned regularly with posts [12].

those found in nature. For simplicity, we shall focus on the case where the superhydrophobic surfaces are patterned with regular rectangular posts in this thesis. Whilst the quantitative details may differ from one superhydrophobic surface to another, we expect that the qualitative descriptions we present in this thesis will remain valid.

There are two ways in which superhydrophobic behaviour can occur. When the drop is suspended on top of the surface roughness, as shown in Fig. 1.4(a), the substrate is effectively a composite of liquid-solid and liquid-gas sections. If the length scale of the posts is much smaller than the drop size, the effective liquid-substrate surface tension is given by $\Phi \sigma_{LS} + (1 - \Phi) \sigma_{LG}$, while the effective gas-substrate surface tension is given by $\Phi \sigma_{GS}$. Here Φ is the solid (area) fraction of the substrate on top of the posts. Substituting these to the Young's equation (Eq. (1.1)), we obtain the so-called Cassie-Baxter equation [11]

$$\cos \theta_{CB} = \Phi \cos \theta_e - (1 - \Phi). \quad (1.4)$$

This state is called the suspended or Cassie-Baxter state. On the other hand, if the liquid drop fills the space between the posts, as shown in Fig. 1.4(b), both the liquid-solid and gas-solid contact area are increased by a roughness factor r . In this case, the macroscopic contact angle is given by the Wenzel equation [15]

$$\cos \theta_W = r \cos \theta_e. \quad (1.5)$$

This state is called the collapsed or Wenzel state.

While the drop contact angle is increased both in the Wenzel and Cassie-Baxter states,

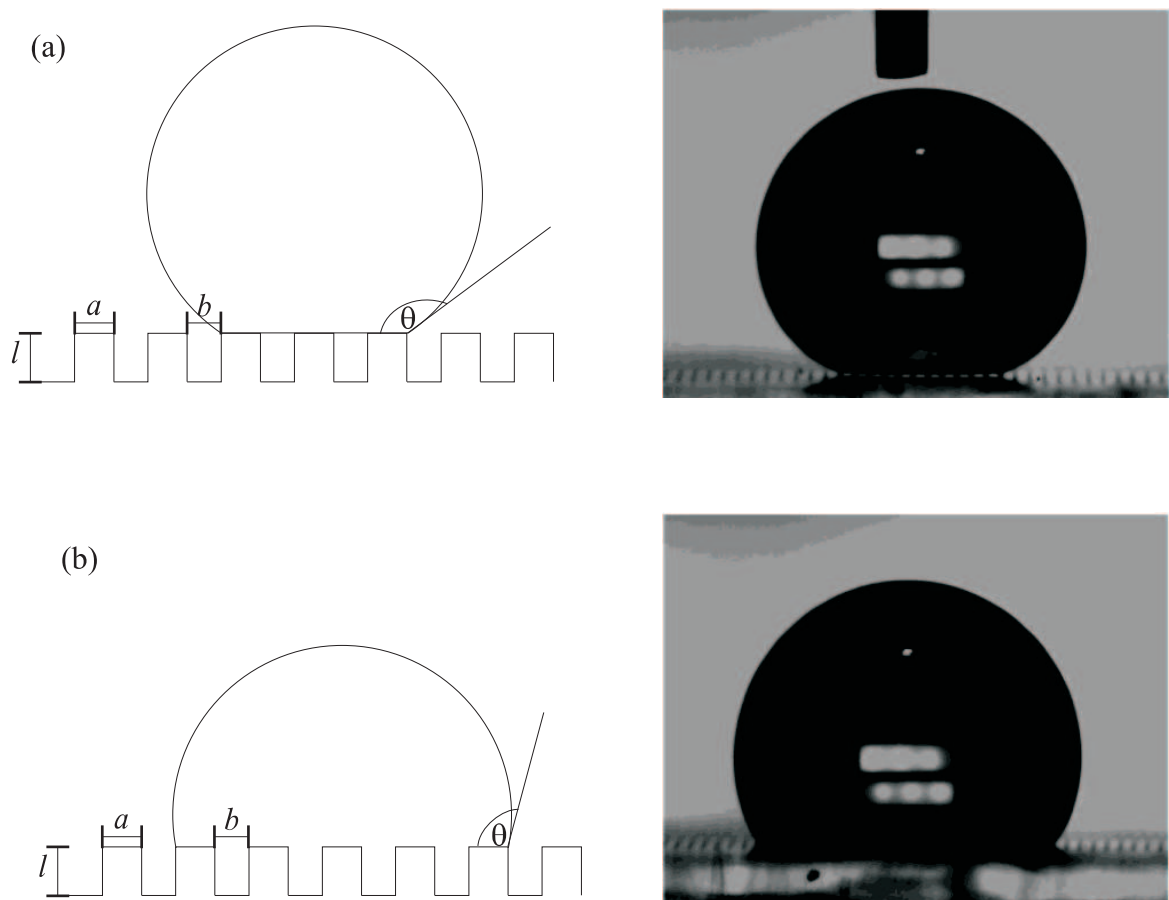


Figure 1.4: A liquid drop in (a) the Cassie-Baxter state and (b) the Wenzel state. The pictures on the right hand side are taken from [16].

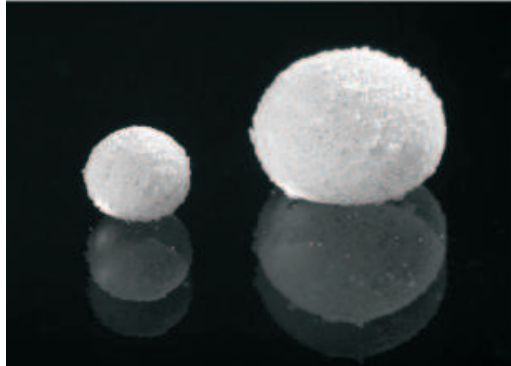


Figure 1.5: An example of liquid marbles. Here the water droplets were coated with a lygodium powder and were then deposited on a glass [24].

their dynamical behaviours are very different. A liquid drop in the suspended state is very mobile, while that in the collapsed state is very immobile. The high mobility of the suspended state is typically associated with the fact that the drop has a small contact angle hysteresis and a large slip length [17–21]. Conversely, a drop in the collapsed state is immobile because it has a large contact angle hysteresis and zero slip length [17–21]. The problem of contact angle hysteresis on a superhydrophobic surface will be discussed in chapter 4.

Considering their different dynamical properties, it is important to understand how and when the collapsed and suspended states are stable, and when the transitions between these two states occur. Both states are often metastable and there is a finite energy barrier opposing the transition between them. The magnitude of the energy barrier has been shown to depend on both the size of the drop and the roughness of the surface [22, 23]. In chapter 5, we consider the situation for which the energy barrier disappears and the drop spontaneously collapses as it evaporates.

We would like to note here that there is an alternative way of creating water-repellent systems. Rather than treating the solid surface, one can treat the liquid-gas interface by coating the liquid drop with a hydrophobic powder. This renders the drop non-wetting, because the hydrophobic grains sit on the interface and stop the liquid drop from making contact with the solid surface. An example of these so-called liquid marbles is shown in Fig. 1.5.

Microfluidics

One of the major reasons that the field of wetting has received renewed interest in the past few years is its relevance to microfluidic applications. Recently there has been a huge effort

in the scientific community to miniaturize fluidic operations, down to micron and nanoscales. Not only has this changed the way scientists think about fluids, but also it potentially has far-reaching technological implications, analogous to the miniaturization of electronics. The goal is to engineer so-called ‘lab on a chip’ devices, where numerous biological and chemical experiments can be performed rapidly and in parallel, while consuming little reagent.

There are two important aspects of flow on micron length scales which we shall comment on here, and which differ greatly from what we are accustomed to in everyday life.

Firstly, microfluidic flow is at low Reynolds number. The Reynolds number is defined as the ratio between inertial and viscous forces,

$$Re = \frac{nvR}{\eta}, \quad (1.6)$$

where n , v , R and η are respectively the density, typical velocity, lengthscale and viscosity of the system. When the Reynolds number is small, mass transport is dominated by viscous dissipation and inertial effects are negligible. The consequences of low Reynolds number are numerous and puzzling at times. For example, in the everyday high Reynolds number world, fluid mixes through turbulent mixing. Since inertia provides the nonlinearity that is responsible for numerous instabilities and for turbulence itself, turbulent mixing does not occur in microfluidic devices and mixing has to occur by diffusion alone, which can take an unacceptably long time.

Secondly, as argued above, when one manipulates fluids on micron and nanoscale, surface effects may dominate over volume effects and wetting can become an extremely important tool to control the fluid behaviour. In chapter 3, we investigate the competition between chemical patterning and a gravity-like body force in determining the motion of liquid drops, while in chapter 6, we study the problem of fluid penetration through a capillary, when the walls of the capillary is patterned with posts and ridges. When the fluid motion is driven by capillary forces, there are two important dimensionless numbers that we will need to consider, the capillary and the Bond number. The capillary number measures the ratio of viscous to surface tension forces

$$Ca = \eta v / \sigma_{LG}. \quad (1.7)$$

The Bond number measures the relative size of an applied body force to the surface tension

force

$$Bo = naR^2/\sigma_{LG}, \quad (1.8)$$

where a is the acceleration associated with the body force.

Summary of the Thesis

This thesis focuses on the computational modeling of wetting and spreading on chemically and topologically patterned surfaces. We start by describing the computational model we have used throughout the thesis in chapter 2, the lattice Boltzmann method. We present three models that can be used to simulate wetting phenomena: the liquid gas, binary, and binary liquid gas model and discuss the relative advantages of each model.

In chapter 3, we look at innovative ways to use chemical patterning to control drop dynamics. We first consider the case where a liquid drop is moving across an array of alternating hydrophobic and hydrophilic stripes. This simple setup allows us to understand the role of the surface forces and compare our numerical results to experiments. We then explore numerically the feasibility of using chemical patterning to control the size and polydispersity of micron-scale drops. The simulations suggest that it is possible to sort drops by size or wetting properties by using an array of hydrophilic stripes of different widths. We also demonstrate that monodisperse drops can be generated by exploiting the pinning of a drop on a hydrophilic stripe.

Next in chapter 4 we study the problem of contact line pinning and contact angle hysteresis, in the presence of both regular chemical and topological patterning. We consider the problem both in two, and three, dimensions using analytical and numerical approaches to minimise the free energy of the drop. In two dimensions we calculate the advancing and receding contact angles on the different surfaces analytically and we use numerical results to argue that these provide bounds for the three dimensional cases. Simulation results further show that a simple average over the disorder is not sufficient to predict the details of the contact angle hysteresis, and that the contact angle hysteresis is indeed much lower for the suspended drops than for the collapsed drops on superhydrophobic surfaces.

The concepts of contact line pinning and contact angle hysteresis turn out to be very important in understanding both the transition between superhydrophobic states and capillary filling over patterned surfaces, which we discuss in chapter 5 and 6 respectively.

In chapter 5, we investigate in particular the transition between the Cassie-Baxter and Wenzel states of a slowly evaporating, micron-scale drop on a superhydrophobic surface. In two dimensions, analytical results show that there are two collapse mechanisms. For long posts the drop collapses when it is able to overcome the free energy barrier presented by the hydrophobic posts. For short posts, as the drop loses volume, its curvature increases allowing it to touch the surface below the posts. We emphasise the importance of the contact line retreating across the surface as the drop becomes smaller: this often preempts the collapse. In three dimensions, we find similar behaviour, with the additional feature that a collapsing drop will first touch the base surface at the centre of the drop. This behaviour is very pronounced when we consider a square lattice of hydrophobic posts. Here the drop can de-pin from all but the peripheral posts, so that the liquid gas interface underneath the drop resembles an inverted bowl.

The capillary filling of microchannels is studied in chapter 6. For smooth capillaries, we find that the liquid gas model does not reproduce the correct dynamical behaviour due to the condensation of the gas phase at the interface. On the other hand, very good agreement is obtained for the binary model when the viscosity of the penetrating fluid is much larger than the displaced fluid. This large viscosity ratio requires us to use the multiple relaxation time lattice Boltzmann method. Otherwise, the advancing contact angle is not reproduced accurately. We then proceed to consider capillary filling over patterned surfaces. Our results show that ridges perpendicular to the flow direction introduce contact line pinning which slows, or sometimes prevents, filling; whereas ridges parallel to the flow provide extra surface which may enhance filling. We further find that patterning the microchannel surface with square posts has little effect on the ability of a channel to fill for equilibrium contact angle $\theta_e < 30^\circ$. For $\theta_e > 60^\circ$, however, even a small number of posts can pin the advancing liquid front.

We finish this thesis in chapter 7, where we summarise our results and discuss areas for future research.

CHAPTER 2

The Lattice Boltzmann Models

“*Computers are incredibly fast, accurate and stupid;
humans are incredibly slow, inaccurate and brilliant;
together they are powerful beyond imagination.*”

- Albert Einstein

In this chapter, we shall describe the models that we have used to obtain the numerical results presented in the subsequent chapters. They belong to a class of hydrodynamic models, called diffuse interface models [25–28], where the interface has a finite width. Far away from the contact line, these models solve the hydrodynamic equations of motion of the fluid, while close to the contact line, the finite interface width allows an effective slip length to be generated by either an evaporation-condensation mechanism [26, 27] or a diffusive transport across the interface [25, 28]. The effective slip length is needed to remove the stress singularity at the contact line (see e.g. [29–31]).

We shall start in section 2.1 by describing the simplest model, the liquid gas model, where the two fluids are the liquid and the gas phase of the same substance. The binary model is then introduced in section 2.2. Here the two fluid components contain particles of different types. In the standard binary model, the two fluid components have the same density. We therefore propose in section 2.3 a binary liquid gas model that allows binary systems with large density ratios to be simulated.

The hydrodynamic equations of motion of diffuse interface models can be solved in many different ways, but in this thesis, this is done using a particular mesoscopic modelling technique called the lattice Boltzmann method. It has proved to be a powerful tool to study many complex fluids problems [32–41], but here we shall only focus on its use to study wetting

phenomena on chemically and topologically patterned surfaces. The algorithms we present in this chapter are based on the so-called free energy lattice Boltzmann method, first introduced by Swift *et al.* [38, 39], and later modified by Briant *et al.* [27, 28] to include the surface wetting term. We shall follow the models suggested by Briant *et al.* closely here, and explain, where appropriate, the improvements we have made to them. In particular, when there is a viscosity difference between the two fluid components, the binary model cannot be reliably simulated using the standard BGK binary lattice Boltzmann algorithm. We shall suggest an improved method based on the multiple relaxation time lattice Boltzmann method which significantly suppresses the unwanted spurious currents.

2.1 The Liquid Gas Model

2.1.1 Thermodynamics of the Fluid

The equilibrium properties of a one-component, two-phase fluid can be described by a Landau free energy functional [27]

$$\Psi = \int_V (\psi_b + \frac{\kappa}{2}(\partial_\alpha n)^2) dV + \int_S \psi_s dS - \mu_b \int_V n dV. \quad (2.1)$$

The first term ψ_b describes the bulk free energy of the system, which we choose for convenience to have the form [27]

$$\begin{aligned} \psi_b &= p_c(\nu_n + 1)^2(\nu_n^2 - 2\nu_n + 3 - 2\beta\tau_w) \\ &= p_c(\nu_n^2 - \beta\tau_w)^2 + \mu_b n - p_0, \end{aligned} \quad (2.2)$$

where $\nu_n = (n - n_c)/n_c$, $\tau_w = (T_c - T)/T_c$, $\mu_b = \partial_n \psi_b|_{n=n_b} = \frac{4p_c}{n_c}(1 - \beta\tau_w)$, $p_0 = p_c(1 - \beta\tau_w)^2$ and n , n_c , n_b , T , T_c , p_0 and p_c are the local density, critical density, the density of the bulk phases, local temperature, critical temperature, equilibrium bulk pressure and critical pressure of the fluid respectively. β is a free parameter in the model that may be used to change the liquid gas density ratio. One can easily see from Eq. (2.2) that this choice of free energy will lead to two coexisting bulk phases of density $n_b = n_c(1 \pm \sqrt{\beta\tau_w})$.

The second term in Eq. (2.1) models the free energy associated with any interfaces in the system. The parameter κ is related to two physical quantities [27]: the surface tension via

$\sigma_{LG} = (4\sqrt{2\kappa p_c}(\beta\tau_w)^{3/2}n_c)/3$, and the interface width via $\xi = \sqrt{(\kappa n_c^2)/(4\beta\tau_w p_c)}$.

The surface term in Eq. (2.1) describes the interactions between the fluid and the solid surface. Following Cahn [42], the surface energy density is taken to be $\psi_s = -h n_s$, where n_s is the value of the fluid density at the surface, so that the strength of interaction is parameterised by the variable h . Minimising the free energy gives an equilibrium boundary condition

$$\kappa \partial_\perp n = \frac{d\psi_s}{dn_s} = -h. \quad (2.3)$$

We would like to stress here that the variable h is in general a function of position and is related to the contact angle θ by [27]

$$h = 2\beta\tau_w \sqrt{2p_c\kappa} \operatorname{sign}\left(\frac{\pi}{2} - \theta\right) \sqrt{\cos\left(\frac{\alpha}{3}\right) \left\{1 - \cos\left(\frac{\alpha}{3}\right)\right\}}, \quad (2.4)$$

where $\alpha = \cos^{-1}(\sin^2 \theta)$ and the function sign returns the sign of its argument. Any variation in the contact angle θ can be modelled easily by constraining the normal derivative $\partial_\perp n$ at different regions of the surface to take the appropriate values given by Eq. (2.4).

Finally, the last term in Eq. (2.1) corresponds to a Lagrange multiplier that conserves the total mass of the system.

2.1.2 Hydrodynamics of the Fluid

The hydrodynamics of the fluid is described by the continuity (2.5) and the Navier-Stokes (2.6) equations for a nonideal fluid

$$\partial_t n + \partial_\alpha(nv_\alpha) = 0, \quad (2.5)$$

$$\partial_t(nv_\alpha) + \partial_\beta(nv_\alpha v_\beta) = -\partial_\beta P_{\alpha\beta} + \partial_\beta[n\nu(\partial_\beta v_\alpha + \partial_\alpha v_\beta) + n\lambda\delta_{\alpha\beta}\partial_\gamma v_\gamma] + na_\alpha, \quad (2.6)$$

where \mathbf{v} , \mathbf{P} , ν and \mathbf{a} are the local velocity, pressure tensor, shear kinematic viscosity and acceleration provided by the body force respectively. The bulk kinematic viscosity is given by $\lambda + \frac{d}{2}\nu$, where d is the dimension of the system. The thermodynamic properties of the system enter the hydrodynamic description through the pressure tensor \mathbf{P} , which satisfies [27]

$$P_{\alpha\beta} = (p_b - \frac{\kappa}{2}(\partial_\gamma n)^2 - \kappa n \partial_{\gamma\gamma} n) \delta_{\alpha\beta} + \kappa (\partial_\alpha n)(\partial_\beta n), \quad (2.7)$$

$$p_b = p_c(\nu_n + 1)^2(3\nu_n^2 - 2\nu_n + 1 - 2\beta\tau_w).$$

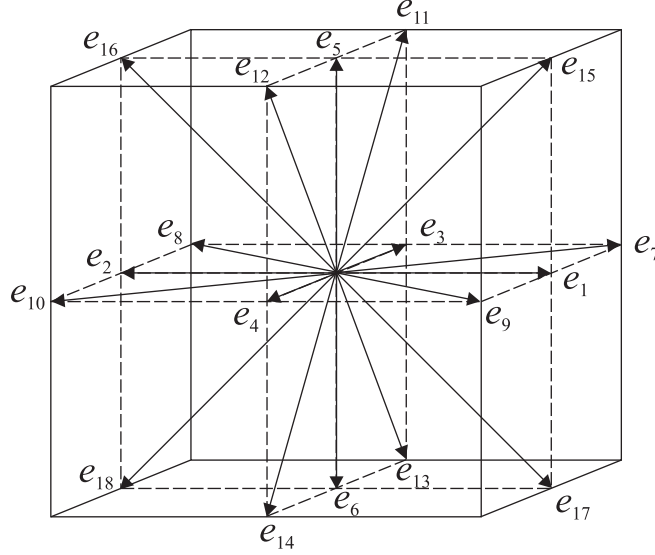


Figure 2.1: The directions of the lattice velocity vectors in the 19-velocity lattice Boltzmann model.

p_b is the bulk pressure term and is related to the speed of sound in the model via $c_s^2 = \frac{dp_b}{dn}$.

2.1.3 The Lattice Boltzmann Implementation

The basic idea of a lattice Boltzmann algorithm [37] is to associate distribution functions $f_i(x, t)$, discrete in time and space, to a set of velocity directions \mathbf{e}_i . For a 19-velocity model¹,

$$\begin{aligned} \begin{pmatrix} e_{x0-6} \\ e_{y0-6} \\ e_{z0-6} \end{pmatrix} &= \begin{bmatrix} 0 & c & -c & 0 & 0 & 0 & 0 \\ 0 & 0 & 0 & c & -c & 0 & 0 \\ 0 & 0 & 0 & 0 & 0 & c & -c \end{bmatrix}, \\ \begin{pmatrix} e_{x7-18} \\ e_{y7-18} \\ e_{z7-18} \end{pmatrix} &= \begin{bmatrix} c & -c & c & -c & 0 & 0 & 0 & c & -c & c & -c \\ c & c & -c & -c & c & -c & c & -c & 0 & 0 & 0 \\ 0 & 0 & 0 & 0 & c & c & -c & -c & c & c & -c & -c \end{bmatrix}. \end{aligned}$$

c is the lattice velocity parameter defined by $c = \Delta x / \Delta t$, where Δx and Δt represent the discretisation in space and time respectively. The directions of the velocity vectors are shown in Fig. 2.1.

¹In this chapter, we only describe our latest implementation of the lattice Boltzmann algorithm. Some of the results presented in this thesis were obtained using the 15-velocity model, but we expect essentially the same results whether we use the 15 or 19-velocity model.

The distributions are related to the physical variables by

$$\sum_i f_i = n, \quad \sum_i f_i e_{i\alpha} = n u_\alpha, \quad (2.8)$$

where \mathbf{u} is defined as $\mathbf{u} = \mathbf{v} - \mathbf{a}\Delta t/2$, and \mathbf{a} here is the acceleration associated with an applied body force. This distinction is required so that the lattice Boltzmann equation recover the continuity (2.5) and Navier-Stokes (2.6) equations in the continuum limit².

Taking a single-time relaxation approximation, the evolution equation for a given distribution function f_i takes the form

$$\text{Collision step : } f'_i(\mathbf{r}, t) = f_i(\mathbf{r}, t) - \frac{1}{\tau} [f_i - f_i^{eq}] + F_i, \quad (2.9)$$

$$\text{Propagation step : } f_i(\mathbf{r} + \mathbf{e}_i \Delta t, t + \Delta t) = f'_i(\mathbf{r}, t),$$

where f_i^{eq} is a local equilibrium distribution function, τ is the relaxation time and F_i is a term that corresponds to an external body force. The relaxation time τ is related to the viscosities ν and λ via

$$\nu = (c^2 \Delta t (\tau - 1/2)) / 3, \quad (2.10)$$

$$\lambda = \nu (1 - 3c_s^2/c^2). \quad (2.11)$$

The value of the relaxation time τ has to be larger than 1/2.

It can be shown [38] that Eq. (2.9) reproduces Eqs. (2.5) and (2.6) in the continuum limit if the correct thermodynamic and hydrodynamic information is input to the simulation by a suitable choice of local equilibrium functions and forcing terms, i.e. if the following constraints are satisfied

$$\begin{aligned} \sum_i f_i^{eq} &= n, \quad \sum_i f_i^{eq} e_{i\alpha} = n u_\alpha, \\ \sum_i f_i^{eq} e_{i\alpha} e_{i\beta} &= P_{\alpha\beta} + n u_\alpha u_\beta + \lambda [u_\alpha \partial_\beta n + u_\beta \partial_\alpha n + \delta_{\alpha\beta} u_\gamma \partial_\gamma n], \\ \sum_i f_i^{eq} e_{i\alpha} e_{i\beta} e_{i\gamma} &= \frac{nc^2}{3} [u_\alpha \delta_{\beta\gamma} + u_\beta \delta_{\gamma\alpha} + u_\gamma \delta_{\alpha\beta}], \\ \sum_i F_i &= 0, \quad \sum_i F_i e_{i\alpha} = \Delta t n a_\alpha, \quad \sum_i F_i e_{i\alpha} e_{i\beta} = \Delta t (n u_\alpha a_\beta + n u_\beta a_\alpha). \end{aligned} \quad (2.12)$$

²In practice, the value of \mathbf{v} is typically two to three order of magnitudes larger than \mathbf{a} in our simulations. Hence the distinction between \mathbf{u} and \mathbf{v} can be neglected.

A possible choice for f_i^{eq} and F_i that satisfies the constraints above is a power series expansion in the velocity [43]

$$\begin{aligned} f_i^{eq} &= \frac{w_i}{c^2} \left(p_b - \kappa n \nabla^2 n + e_{i\alpha} n u_\alpha + \frac{3}{2c^2} \left[e_{i\alpha} e_{i\beta} - \frac{c^2}{3} \delta_{\alpha\beta} \right] (n u_\alpha u_\beta + \lambda [u_\alpha \partial_\beta n + u_\beta \partial_\alpha n + \delta_{\alpha\beta} u_\gamma \partial_\gamma n]) \right) \\ &\quad + \frac{\kappa}{c^2} \left(w_i^{xx} \partial_x n \partial_x n + w_i^{yy} \partial_y n \partial_y n + w_i^{zz} \partial_z n \partial_z n + w_i^{xy} \partial_x n \partial_y n + w_i^{yz} \partial_y n \partial_z n + w_i^{zx} \partial_z n \partial_x n \right), \\ F_i &= \frac{w_i}{c^2} \left[e_{i\alpha} n a_\alpha + \frac{3}{2c^2} \left(e_{i\alpha} e_{i\beta} - \frac{c^2}{3} \delta_{\alpha\beta} \right) (n u_\alpha a_\beta + n u_\beta a_\alpha) \right], \end{aligned} \quad (2.13)$$

where the appropriate coefficients that minimise the spurious velocities [43] are given by

$$\begin{aligned} w_{1-6} &= \frac{1}{6}, & w_{7-18} &= \frac{1}{12}, \\ w_{1,2}^{xx} &= w_{3,4}^{yy} = w_{5,6}^{zz} = \frac{5}{12}, \\ w_{3-6}^{xx} &= w_{1,2,5,6}^{yy} = w_{1-4}^{zz} = -\frac{1}{3}, \\ w_{7-10}^{xx} &= w_{15-18}^{xx} = w_{7-14}^{yy} = w_{11-18}^{zz} = -\frac{1}{24}, \\ w_{11-14}^{xx} &= w_{15-18}^{yy} = w_{7-10}^{zz} = \frac{1}{12}, \\ w_{1-6}^{xy} &= w_{1-6}^{yz} = w_{1-6}^{zx} = 0, \\ w_{7,10}^{xy} &= w_{11,14}^{yz} = w_{15,18}^{zx} = \frac{1}{4}, \\ w_{8,9}^{xy} &= w_{12,13}^{yz} = w_{16,17}^{zx} = -\frac{1}{4}, \\ w_{11-18}^{xy} &= w_{7-10}^{yz} = w_{15-18}^{yz} = w_{7-14}^{zx} = 0. \end{aligned}$$

We note that the choice for implementing the liquid gas model is not unique. There are equivalent models in the literature, for example [44–46], that have been used to model liquid gas systems with considerable success. There has also been extensive work in the literature that aims to improve both the stability [47] and accuracy of the model [43, 48, 49].

2.1.4 Boundary Conditions

In our lattice Boltzmann simulations, there are two important boundary conditions: the wetting boundary condition, given by Eq. (2.3), and the no-slip boundary condition. While these boundary conditions are simple conceptually, their implementation can be difficult for complex geometries.

In our simulations, the no-slip condition is implemented using a link bounce back rule proposed by Ladd and Verberg [36]. A schematic diagram of this rule is shown in Fig. 2.2(a),

where we shall describe the one dimensional case. In one dimension, there are two distribution functions, $f_1[k]$ and $f_2[k]$, for a given lattice node k . When the lattice node k is located next to a wall, as shown in Fig. 2.2(a), the distribution function $f_1^*[k]$ is undetermined after the propagation step. To determine $f_1^*[k]$, there are two cases to consider. If the distance of the wall from the fluid node, d_{wall} , is less than half of a lattice spacing, we interpolate a value between $f_2[k]$ and $f_2[k+1]$, such that it travels exactly one lattice spacing to bounce off the wall and arrive at $f_1^*[k]$. On the other hand, if d_{wall} is more than half of a lattice spacing, we first bounce $f_2[k]$ to the wall for exactly one lattice spacing. We then interpolate the value of $f_1^*[k]$ from $f_2[k]$ and $f_1[k]$. In summary,

$$d_{\text{wall}} < 0.5 : f_1^*[k] = f_2[k] \times 2d_{\text{wall}} + f_2[k+1] \times (1 - 2d_{\text{wall}}), \quad (2.14)$$

$$d_{\text{wall}} > 0.5 : f_1^*[k] = f_2[k]/2d_{\text{wall}} + f_1[k] \times (1 - 1/(2d_{\text{wall}})).$$

An alternative way of imposing the no-slip condition is given by Dupuis and Yeomans [50]. In their method, the values of the missing distribution functions are determined by imposing $\mathbf{v}_{\text{wall}} = 0$ as well as by using symmetry considerations.

We use two ways to implement the wetting boundary condition. A schematic diagram of the two implementations is shown in Fig. 2.2(b). In the first method, one sets $\partial n / \partial z$ to take the value given by Eq. (2.3) at the $n0$ lattice node and calculates $\partial^2 n / \partial z^2$ by Taylor expanding $n5$ with respect to $n0$ and neglecting the third derivatives in n and higher,

$$\partial^2 n / \partial z^2 = 2 \times (n5 - n0 - \partial n / \partial z). \quad (2.15)$$

The main advantage of this implementation is that one does not need to simulate any solid nodes.

An alternative implementation of the wetting boundary condition is to assign appropriate density values to the solid nodes neighbouring the boundary, so that Eq. (2.3) is satisfied. In the schematic diagram shown in Fig. 2.2(c), this corresponds to assigning a value for $n6$ using

$$n6 = n5 - 2 \partial n / \partial z. \quad (2.16)$$

The main advantage of this implementation is that $\nabla^2 n$ can be calculated in exactly the same way as in the bulk. Furthermore, since all the nearest and next nearest neighbour nodes have

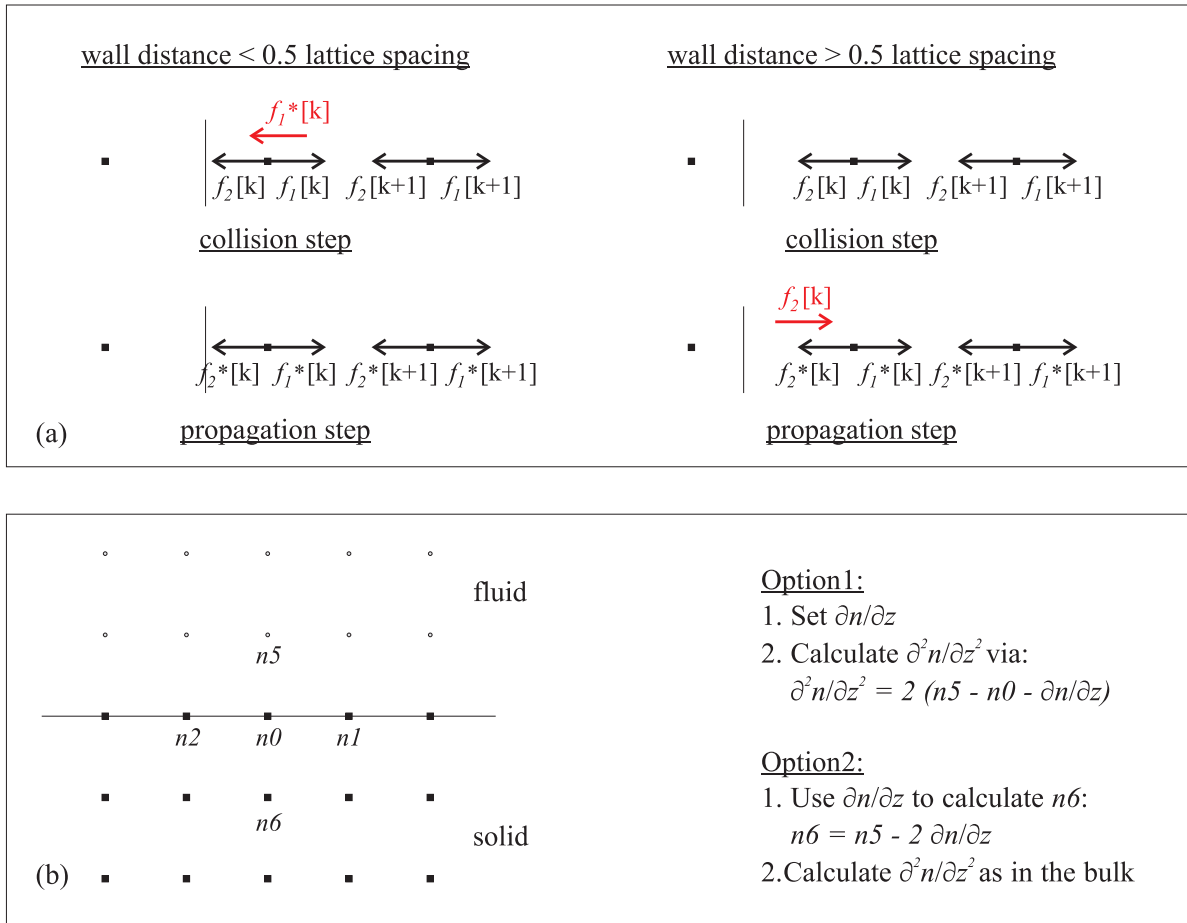


Figure 2.2: Schematic diagram of the no-slip and wetting boundary conditions. (a) Link bounce back rule. (b) Implementations of the wetting boundary condition.

the appropriate density values, one can achieve better accuracy if an appropriate stencil is used to calculate the derivatives [43].

2.2 The Binary Model

2.2.1 Thermodynamics and Hydrodynamics of the Fluid

In a similar way to the liquid gas model, the equilibrium properties of a binary fluid can be described by a Landau free energy functional [28]

$$\Psi = \int_V (\psi_b + \frac{\kappa}{2}(\partial_\alpha \phi)^2) dV + \int_S \psi_s dS, \quad (2.17)$$

where the bulk free energy density ψ_b is taken to have the form

$$\psi_b = \frac{c^2}{3} n \ln n + A \left(-\frac{1}{2} \phi^2 + \frac{1}{4} \phi^4 \right). \quad (2.18)$$

In this model, n is the fluid density, ϕ is the order parameter and $c = \Delta x / \Delta t$ as before. This choice of ψ_b gives binary phase separation into two phases with $\phi = \pm 1$.

The gradient term in Eq. (2.17) represents an energy contribution from variations in ϕ and is related to the surface tension between the two phases through $\sigma_{LG} = \sqrt{8\kappa A/9}$ and to the interface width through $\xi = \sqrt{\kappa/A}$ [28].

The second integral in Eq. (2.17) is over the system's solid surface and is used to describe the interactions between the fluid and the solid surface. Similar to section 2.1, the surface energy density is taken to be $\psi_s = -h\phi_s$ [42], where ϕ_s is the value of the order parameter at the surface. Minimisation of the free energy shows that the gradient in ϕ at the solid boundary is [28]

$$\kappa \partial_\perp \phi = -\frac{d\psi_s}{d\phi_s} = -h. \quad (2.19)$$

The value of the phenomenological parameter h is related to the equilibrium contact angle θ (θ is taken with respect to the $\phi = 1$ component) via [28]:

$$h = \sqrt{2\kappa A} \operatorname{sign}\left(\frac{\pi}{2} - \theta\right) \sqrt{\cos\left(\frac{\alpha}{3}\right) \left\{1 - \cos\left(\frac{\alpha}{3}\right)\right\}}, \quad (2.20)$$

where $\alpha = \cos^{-1}(\sin^2 \theta)$ and the function sign returns the sign of its argument.

The hydrodynamic equations for the binary fluid are the continuity equation (2.5), the Navier-Stokes equation (2.6) and the convection diffusion equation

$$\partial_t \phi + \partial_\alpha (\phi u_\alpha) = M \nabla^2 \mu. \quad (2.21)$$

where M here is a mobility. The equilibrium properties of the fluid appear in the equations of motion through the pressure tensor and the chemical potential. Both the pressure tensor and chemical potential of the fluid can be obtained in the usual way from the free energy and are given by [28]

$$\mu = \frac{\delta \psi_b}{\delta \phi} = A (-\phi + \phi^3) - \kappa \nabla^2 \phi, \quad (2.22)$$

$$P_{\alpha\beta} = (p_b - \frac{\kappa}{2}(\partial_\gamma \phi)^2 - \kappa \phi \partial_{\gamma\gamma} \phi) \delta_{\alpha\beta} + \kappa (\partial_\alpha \phi)(\partial_\beta \phi), \quad (2.23)$$

$$p_b = \frac{c^2}{3} n + A \left(-\frac{1}{2} \phi^2 + \frac{3}{4} \phi^4 \right).$$

2.2.2 The Lattice Boltzmann Implementation: Single Relaxation Time

In the binary model, we need two particle distribution functions $f_i(\mathbf{r}, t)$ and $g_i(\mathbf{r}, t)$ on each lattice point. As in the liquid gas model, the first distribution function $f_i(\mathbf{r}, t)$ is related to the fluid density and momentum. The second particle distribution function, on the other hand, is related to the concentration ϕ via

$$\phi = \sum_i g_i. \quad (2.24)$$

The time evolution equation for the particle distribution functions, using the standard BGK approximation, can be broken down into two steps

$$\text{Collision step : } f'_i(\mathbf{r}, t) = f_i(\mathbf{r}, t) - \frac{1}{\tau} [f_i - f_i^{eq}] + F_i, \quad (2.25)$$

$$g'_i(\mathbf{r}, t) = g_i(\mathbf{r}, t) - \frac{1}{\tau_\phi} [g_i - g_i^{eq}],$$

$$\begin{aligned} \text{Propagation step : } & f_i(\mathbf{r} + \mathbf{e}_i \Delta t, t + \Delta t) = f'_i(\mathbf{r}, t), \\ & g_i(\mathbf{r} + \mathbf{e}_i \Delta t, t + \Delta t) = g'_i(\mathbf{r}, t). \end{aligned}$$

f_i^{eq} and g_i^{eq} are equilibrium distribution functions, again, defined as a power series in the

velocity. The appropriate choices for f_i^{eq} and g_i^{eq} are taken to be

$$\begin{aligned} f_i^{eq} &= \frac{w_i}{c^2} \left(p_b - \kappa \phi \nabla^2 \phi + e_{i\alpha} n u_\alpha + \frac{3}{2c^2} \left[e_{i\alpha} e_{i\beta} - \frac{c^2}{3} \delta_{\alpha\beta} \right] (n u_\alpha u_\beta + \lambda [u_\alpha \partial_\beta n + u_\beta \partial_\alpha n + \delta_{\alpha\beta} u_\gamma \partial_\gamma n]) \right) \\ &\quad + \frac{\kappa}{c^2} \left(w_i^{xx} \partial_x \phi \partial_x \phi + w_i^{yy} \partial_y \phi \partial_y \phi + w_i^{zz} \partial_z \phi \partial_z \phi + w_i^{xy} \partial_x \phi \partial_y \phi + w_i^{yz} \partial_y \phi \partial_z \phi + w_i^{zx} \partial_z \phi \partial_x \phi \right), \\ g_i^{eq} &= \frac{w_i}{c^2} \left(\Gamma \mu + e_{i\alpha} \phi u_\alpha + \frac{3}{2c^2} \left[e_{i\alpha} e_{i\beta} - \frac{c^2}{3} \delta_{\alpha\beta} \right] \phi u_\alpha u_\beta \right), \end{aligned} \quad (2.26)$$

where the coefficients w_i 's take the same values as before. The choice of f_i^{eq} satisfies the constraints shown in Eq. (2.12), while that for g_i^{eq} satisfies the following

$$\begin{aligned} \sum_i g_i^{eq} &= \phi, \quad \sum_i g_i^{eq} e_{i\alpha} = \phi u_\alpha, \\ \sum_i g_i^{eq} e_{i\alpha} e_{i\beta} &= \Gamma \mu \delta_{\alpha\beta} + \phi u_\alpha u_\beta. \end{aligned} \quad (2.27)$$

The lattice Boltzmann equations (2.25) for $g_i(\mathbf{r}, t)$ lead to the convection diffusion equation (2.21) in the limit of long length and time scales. The relaxation parameter τ_ϕ is related to the mobility through

$$M = \Delta t \Gamma \left(\tau_\phi - \frac{1}{2} \right), \quad (2.28)$$

where Γ is a tunable parameter that appears in the equilibrium distribution. As for τ_n , the value of the relaxation time τ_ϕ has to be larger than 1/2.

2.2.3 The Lattice Boltzmann Implementation: Multiple Relaxation Time

We next summarise the basic methodology behind the multi-relaxation-timescale lattice Boltzmann [51, 52]. The idea behind the multiple relaxation time lattice Boltzmann method is that different relaxation parameters are used for different linear combinations of the distribution functions. In particular, we set the relaxation parameters responsible for generating the viscous terms in the Navier-Stokes equation (2.6) to τ_n , those connected to conserved quantities to ∞ and all others to 1. This choice for the relaxation parameters is justified below.

In the multiple relaxation time lattice Boltzmann method, the relaxation term $\frac{1}{\tau_n} [f_i - f_i^{eq}]$ on the right hand side of the lattice Boltzmann equation for f_i (2.25) is replaced by

$$\mathbf{M}^{-1} \mathbf{S} \mathbf{M} [\mathbf{f} - \mathbf{f}^{eq}], \quad (2.29)$$

where the particle distributions f_i and f_i^{eq} are written as column vectors and \mathbf{M} is the matrix [53]

$$\mathbf{M} = \begin{pmatrix} 1 & 1 & 1 & 1 & 1 & 1 & 1 & 1 & 1 & 1 & 1 & 1 & 1 & 1 & 1 & 1 & 1 & 1 & 1 \\ -30 & -11 & -11 & -11 & -11 & -11 & -11 & -11 & 8 & 8 & 8 & 8 & 8 & 8 & 8 & 8 & 8 & 8 & 8 \\ 12 & -4 & -4 & -4 & -4 & -4 & -4 & -4 & 1 & 1 & 1 & 1 & 1 & 1 & 1 & 1 & 1 & 1 & 1 \\ 0 & 1 & -1 & 0 & 0 & 0 & 0 & 0 & 1 & -1 & 1 & -1 & 0 & 0 & 0 & 0 & 1 & -1 & 1 & -1 \\ 0 & -4 & 4 & 0 & 0 & 0 & 0 & 0 & 1 & -1 & 1 & -1 & 0 & 0 & 0 & 0 & 1 & -1 & 1 & -1 \\ 0 & 0 & 0 & 1 & -1 & 0 & 0 & 0 & 1 & 1 & -1 & -1 & 1 & -1 & 1 & -1 & 0 & 0 & 0 & 0 \\ 0 & 0 & 0 & -4 & 4 & 0 & 0 & 0 & 1 & 1 & -1 & -1 & 1 & -1 & 1 & -1 & 0 & 0 & 0 & 0 \\ 0 & 0 & 0 & 0 & 0 & 1 & -1 & 0 & 0 & 0 & 0 & 0 & 1 & 1 & -1 & -1 & 1 & 1 & -1 & -1 \\ 0 & 0 & 0 & 0 & 0 & -4 & 4 & 0 & 0 & 0 & 0 & 0 & 1 & 1 & -1 & -1 & 1 & 1 & -1 & -1 \\ 0 & 0 & 0 & 0 & 0 & 0 & -4 & 4 & 0 & 0 & 0 & 0 & 0 & 1 & 1 & -1 & -1 & 1 & 1 & -1 & -1 \\ 0 & 2 & 2 & -1 & -1 & -1 & -1 & 1 & 1 & 1 & 1 & -2 & -2 & -2 & -2 & 1 & 1 & 1 & 1 & 1 \\ 0 & -4 & -4 & 2 & 2 & 2 & 2 & 1 & 1 & 1 & 1 & -2 & -2 & -2 & -2 & 1 & 1 & 1 & 1 & 1 \\ 0 & 0 & 0 & 1 & 1 & -1 & -1 & 1 & 1 & 1 & 1 & 0 & 0 & 0 & 0 & -1 & -1 & -1 & -1 & -1 \\ 0 & 0 & 0 & -2 & -2 & 2 & 2 & 1 & 1 & 1 & 1 & 0 & 0 & 0 & 0 & -1 & -1 & -1 & -1 & -1 \\ 0 & 0 & 0 & 0 & 0 & 0 & 0 & 1 & -1 & -1 & 1 & 0 & 0 & 0 & 0 & 0 & 0 & 0 & 0 & 0 \\ 0 & 0 & 0 & 0 & 0 & 0 & 0 & 0 & 0 & 0 & 0 & 1 & -1 & -1 & 1 & 0 & 0 & 0 & 0 & 0 \\ 0 & 0 & 0 & 0 & 0 & 0 & 0 & 0 & 0 & 0 & 0 & 0 & 0 & 0 & 0 & 0 & 1 & -1 & -1 & 1 \\ 0 & 0 & 0 & 0 & 0 & 0 & 0 & 0 & 1 & -1 & 1 & -1 & 0 & 0 & 0 & 0 & -1 & 1 & -1 & 1 \\ 0 & 0 & 0 & 0 & 0 & 0 & 0 & 0 & -1 & -1 & 1 & 1 & 1 & -1 & 1 & -1 & 0 & 0 & 0 & 0 \\ 0 & 0 & 0 & 0 & 0 & 0 & 0 & 0 & 0 & 0 & 0 & -1 & -1 & 1 & 1 & 1 & 1 & 1 & 1 & -1 \end{pmatrix}. \quad (2.30)$$

Each of the rows in \mathbf{M} is mutually orthogonal so the inverse follows easily as

$$\mathbf{M}_{ij}^{-1} = \frac{1}{\sum_k \mathbf{M}_{jk}^2} \mathbf{M}_{ji}. \quad (2.31)$$

The matrix \mathbf{M} performs a change of basis. The new basis is designed to contain more physically relevant variables. For our purpose, the important terms are as follows. The first row corresponds to the density n . Similarly, the fourth, sixth and eighth lines calculate the momentum densities nu_x , nu_y and nu_z respectively. These are the conserved moments. The tenth, twelfth, fourteenth, fifteenth and sixteenth lines correspond to the components of the symmetric traceless viscous stress tensor $3\sigma_{xx}$, $\sigma_{yy} - \sigma_{zz}$, σ_{xy} , σ_{yz} and σ_{xz} .

The matrix \mathbf{S} in Eq. (2.29) is diagonal and has the values

$$\mathbf{S} = \text{diag}(0, 1, 1, 0, 1, 0, 1, 0, 1, \omega, 1, \omega, 1, \omega, \omega, \omega, 1, 1, 1), \quad (2.32)$$

where $\omega = 1/\tau_n$ now determines the fluid viscosity ν and λ . Note that some of these values are zero. This choice is arbitrary as these modes correspond to the conserved moments, for which $M_{ji} [f_i - f_i^{eq}] = 0$ for $j = 0, 3, 5, 7$. The choice of unity for the other terms is to minimise

the spurious velocities. This is an acceptable choice because they do not correspond to any physical variables important for the problems we are interested in in this thesis.

The Need for the Multiple Relaxation Time Lattice Boltzmann Method

In this section we will show that the single relaxation time lattice Boltzmann method does not give the correct equilibrium contact angle at the three phase contact point when there is a viscosity difference between the two fluid components. We shall then propose an algorithm based on multiple relaxation time lattice Boltzmann to significantly suppress these spurious currents at the contact point.

In Eq. (2.20), we have an equation that relates the parameter h to the contact angle θ . We performed simulations to verify this relation. Initially, a semi-circle of fluid of radius $R = 35$ was placed on the surface with a corresponding contact angle of 90° . This was achieved by setting $\partial_\perp \phi|_b = 0$ and the system was evolved for 3×10^4 time-steps, such that it reached equilibrium. The contact angle was then varied by changing the gradient of the order parameter at the solid boundary, $\partial_\perp \phi|_b$, over the course of 10^6 times step. This is done for both increasing and decreasing values of $\partial_\perp \phi|_b$. The lattice Boltzmann system size was set to be 300×100 lattice units and the parameters used were $A = 0.04$, $\tau_\phi = 1$, $\Gamma = 0.5$, $\Delta t = \Delta x = 1$, and $\kappa = 0.04$, giving an interface width of $W = 1$ lattice site and an interfacial tension of $\sigma_{lg} = 0.038$ in lattice units. The relaxation parameter τ_n is determined by

$$\tau_n = \tau_{nB} + \frac{\phi+1}{2} (\tau_{nA} - \tau_{nB}), \quad (2.33)$$

such that it changes smoothly through the interface and has the bulk values τ_{nA} and τ_{nB} in the liquid and gas phases, respectively. The values $\tau_{nA} = 3$ and $\tau_{nB} = 0.7$ were chosen to give a viscosity ratio of $R_\nu = \frac{\tau_{nA}-0.5}{\tau_{nB}-0.5} = 12.5$.

Numerical measurements of contact angle were performed in the following way: Each link between neighbouring lattice sites was examined to see if at one end it was liquid ($\phi > 0$) and at the other end gas ($\phi < 0$). If this was the case then a linear interpolation was used to predict the point on the link where $\phi = 0$. The equilibrium contact angle was estimated by performing a least squares fit of these points to a circular section and then calculating the contact angle the section makes with the surface.

The lattice Boltzmann simulation results for the equilibrium contact angle are shown in Fig.

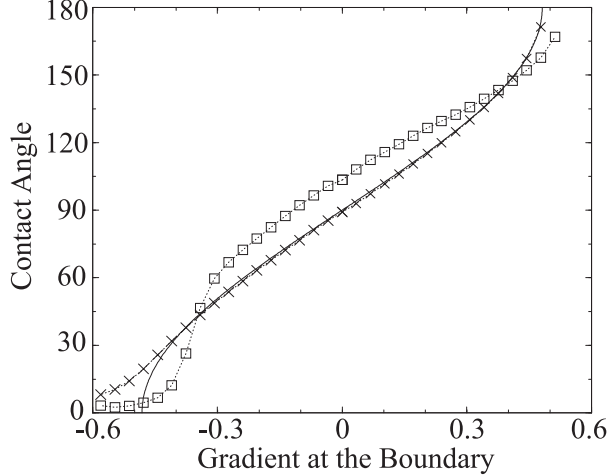


Figure 2.3: The equilibrium contact angle as a function of the gradient in ϕ at the boundary, $\partial_\perp \phi|_b$, for $\tau_{nA} = 3$, $\tau_{nB} = 0.7$. Squares and crosses are simulation results obtained using the standard BGK and multi-relaxation-timescale lattice Boltzmann respectively. The solid curve is the theoretical expression, Eq. (2.20).

2.3 for both the standard BGK approximation and multiple relaxation time lattice Boltzmann method. The exact result given in Eq. (2.20) is also shown for comparison. There are large errors for the standard BGK approximation. This discrepancy is caused by strong spurious currents near the contact point which continuously push the system out of equilibrium and result in the deformation of the drop. Similar behaviour is obtained in the liquid gas model, but since the spurious velocities are typically an order of magnitude smaller than in the binary model, the effect is less pronounced. The origin of these spurious velocities come from two contributions: one from long range effects and another from the bounce back method. These are discussed in details in [54].

Suppressing the spurious currents

We now describe how an algorithm based on the multiple relaxation time lattice Boltzmann approach can be used to significantly reduce the spurious currents at the contact point. The approach comprises the following steps:

Step 1: We calculate the density, concentration and velocity using the moments described in Eqs. (2.8) and (2.24).

Step 2: Set the velocity of the boundary nodes to zero.

Step 3: We use the multiple relaxation time lattice Boltzmann method described in section 2.2.3 to perform the collision step.

Step 4: We perform the streaming step with link bounce back at the boundaries.

This approach works because we have kept the velocity correlations correctly by choosing the relaxation time of the viscous stress tensor terms to τ_n , while at the same time removing the incorrect information fed into the distribution functions by the boundary after each collision step by choosing $\tau = 1$ for the non-hydrodynamic modes.

For a system with variable viscosity it would seem necessary to recalculate the collision matrix $\mathbf{C} = \mathbf{M}^{-1}\mathbf{SM}$ at each lattice node and at each time-step. This would be extremely computationally slow and not very practical. The approach we take is to create a lookup table with $\sim 10^4$ different values of viscosity and simply pick the closest match.

We find the implementing the algorithm presented above leads to a significant improvement in the accuracy of the equilibrium contact angle. The simulation results are shown in Fig. 2.3 for $\tau_{nA} = 3$, $\tau_{nB} = 0.7$. Deviations at small angles are expected due to finite interface width effects.

2.3 The Binary Liquid Gas Model

For situations in which inertia is important, it is necessary to not only attain a large viscosity ratio between the liquid and gas phases, but also a large density difference. We present here a modification to the free energy which allows this. Specifically, the bulk free energy term in Eq. (2.18) is replaced by

$$\psi_b = A \left(-\frac{1}{2}\phi^2 + \frac{1}{4}\phi^4 \right) + \gamma \left[n - \left(\frac{n_l - n_g}{2}\phi + \frac{n_l + n_g}{2} \right) \right]^2. \quad (2.34)$$

The first two terms induce the usual phase separation into $\phi = 1$ and $\phi = -1$, which we identify as liquid and gas respectively. The final term in Eq. (2.34) couples the density n to the order parameter ϕ . For example, in the liquid phase, this term becomes $\gamma [n - n_l]^2$. It has a quadratic potential profile around a minimum of $n = n_l$ and hence the system is pushed towards this value in equilibrium. Similarly, the gas phase has a density n_g in equilibrium. The variation in n between the two phases is smooth and follows the tanh profile of the order parameter.

One unusual property of this model is that the speed of sound,

$$c_s^2 = \partial_n p_0 = \partial_n (n\partial_n \psi + \phi\partial_\phi \psi - \psi) = \gamma (n_l + n_g), \quad (2.35)$$

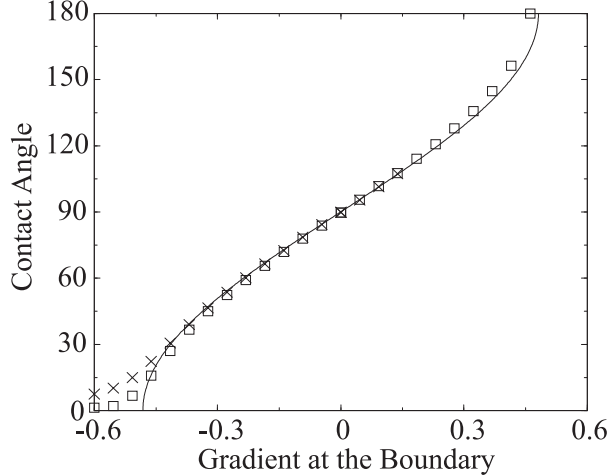


Figure 2.4: The equilibrium contact angle as a function of the gradient in ϕ at the boundary, $\partial_\perp \phi|_b$, for the binary-liquid-gas system (squares for $n_g = 0.5$, $n_l = 2$, crosses for $n_g = 0.5$, $n_l = 10$).

is constant throughout the system, *i.e.* it is the same in both the liquid and gas phases. This is, of course, unphysical, as the sound speed in the liquid phase should be faster due to particles being more closely packed together. However, in many situations the velocities in the system are much smaller than c_s and hence this is not an important quantity (this is why assuming fluid incompressibility is such a good approximation in most cases).

Figure 2.4 shows the result of simulations measuring the equilibrium contact angle using the binary-liquid-gas model. The model is implemented using the multiple relaxation time lattice Boltzmann method described in section 2.2. The squares denote results using a density ratio of $R_n = n_l/n_g = 4$. Agreement is to within a few degrees over a large range of contact angles. However, at large contact angle the deviation is quite marked when compared to the binary case shown in Fig. 2.3. We have not yet established the reasons behind this discrepancy. The crosses in Fig. 2.4 denote results using a larger density ratio of $R_n = 20$. In this case, it was found that, for contact angles larger than $\sim 110^\circ$, the simulations were no longer stable. This was because the density in the gas phase at the wall became negative as a result of the wetting boundary conditions.

2.4 Discussion

In this chapter, we have described three models that can be used to simulate wetting phenomena on patterned surfaces. In the liquid gas model, the two fluid phases are of the same

substance and, as a result, the liquid (gas) phase can evaporate (condense) to the gas (liquid) phase. The evaporation-condensation mechanism is important close to the contact line, where it provides a way to relax the no-slip boundary condition and hence allow the contact line to move. The main difficulty with this model is that the liquid gas density ratio is often limited to unphysically small values by the stability of the algorithm and as we shall see later in chapters 3 and 6, this may lead to an unphysical dynamical behaviour. By fine tuning the parameters in the simulations, the model presented in this chapter can be made numerically stable for a density ratio of up to about 15-20. Nonetheless, this only works for a small range of parameters and a higher density ratio is not possible. An important area of future research, therefore, is to devise a better equation of state, *i.e.* a better form of the bulk free energy, where density ratios of order 100 or more can be achieved over a large range of parameter values.

In the binary model, on the other hand, the two fluids are of different substances and the evaporation-condensation mechanism is forbidden. Here the contact line moves via diffusion and the effective slip length at the contact line can be tuned by choosing a free parameter called the mobility M . This is a very advantageous feature of the binary model, although thus far, no study has been made to determine the value of M that corresponds to experiments. Unfortunately, the binary model is not without its drawbacks. Firstly, it is always slower than the liquid gas model, because we have to evolve twice as many distribution functions. Secondly, in the standard binary model, the fluid densities and viscosities are the same. In this chapter, we have proposed how viscosity and density differences may be simulated accurately. The former is done by using an algorithm based on the multiple relaxation time lattice Boltzmann method, while the latter can be done by coupling the density of the fluid to the order parameter. In the future, we plan to assess the bulk stability of the binary liquid gas model and devise a better way of implementing the wetting boundary condition.

CHAPTER 3

The Influence of Chemical Patterning on the Dynamics of Micron-scale Liquid Drops

“*Science is always wrong.*

It never solves a problem without creating ten more.”

- George Bernard Shaw

The question of how liquid drops wet and move across a solid surface has long caught the interests of academic and industrial communities alike, with applications ranging from microfluidic devices to ink-jet printing and surface coating. Though much progress has been made since the first pioneering work by Young and Laplace, many interesting, unanswered questions remain. One which has recently come to the fore because of experimental advances allowing the fabrication of surfaces with mesoscopic hydrophobic and hydrophilic regions is the behaviour of drops on chemically patterned substrates. Several authors [6, 55–61] have shown that the wetting behaviour on these substrates can be very rich, with the drop shapes depending sensitively on parameters such as the dimensions and contact angles of the patterning. In this chapter we build on this work to address the *dynamics* of drops moving across chemically patterned surfaces, focussing on the centre of mass motion as well as the morphological transitions induced by the imposed external flow. The drop is pushed by a constant gravity-like acceleration as opposed to [62, 63] where a thermal or chemical gradient is applied to generate the drop motion.

We first present numerical and experimental results following the dynamics of micron-scale drops moving across a surface patterned with alternating hydrophobic and hydrophilic stripes perpendicular to the drop motion. The drop behaviour is determined by the balance between

the driving force and the variation in the surface force as it moves between regions of different wettability. As the wettability contrast increases there are large deviations of the drop shape from spherical as it moves across the surface. We further show that there is close agreement between results of the lattice Boltzmann simulations and experiments. This gives us confidence in using the lattice Boltzmann simulations for designing new ways of controlling the motion of liquid drops on patterned surfaces.

One application where one might envisage a use for surface patterning is in controlling the size and polydispersity of an array of drops, an important consideration in many microfluidic technologies, e.g. [64–77] and the references therein. We explore numerically two ways in which this might be possible. The first uses hydrophilic stripes of different widths to sort drops by size or wetting properties. The second produces monodisperse drops by exploiting their tendency to remain pinned on the hydrophilic regions of the surface.

3.1 Drop Dynamics on Chemically Striped Surfaces

In this section we present numerical and experimental results following the dynamics of micron-scale drops moving across a chemically striped surface. The orientation of the stripes is perpendicular to the direction of the drop motion. We shall focus on three cases. First we consider the simplest case of a drop moving across a boundary between stripes of different contact angle which are much wider than the drop radius. This allows us to demonstrate the different roles of the applied force and the surface force which arise from the change in free energy as the drop crosses a stripe boundary. We then look at stripes of width of order the drop radius and choose the simulation parameters to reproduce as closely as possible the experimental values. We find pleasing agreement between simulations and experiments. We next consider a substrate on which there is a much larger difference in contact angle between the hydrophobic and hydrophilic regions. The shape of the drop shows strong oscillations as it is pushed across this surface, and spreading across the surface perpendicular to the flow becomes important.

3.1.1 Simulations

In this chapter, we use the liquid gas lattice Boltzmann model. We consider a simulation box of size (L_x, L_y, L_z) . The surface at $z = 0$ is patterned by (relatively) hydrophilic and hydrophobic

stripes of contact angles θ_1 and θ_2 and widths δ_1 and δ_2 respectively. A drop of initial radius R lies on this surface and is pushed along the x -direction by a constant acceleration a_x . No-slip boundary conditions are imposed on the velocity field at $z = 0$ and $z = L_z - 1$. We record the drop shape and the position of the centre of mass of the drop as a function of time. Simulation parameters are chosen so that $\nu_{\text{liquid}} = \nu_{\text{gas}} = 0.1$, $n_{\text{liquid}} = 4.11$, $n_{\text{gas}} = 2.89$, $\sigma_{LG} = 7.7 \times 10^{-4}$ and $\xi = 1.81$, while those specific to a particular simulation are given in the corresponding figure's caption.

3.1.2 Experiments

(The experiments in this chapter were performed by Dr. Julien Leopoldes)

The experiments were performed by dispensing drops of ethylene glycol (volume $\sim 2 \text{ mm}^3$, surface tension $\sigma_{LG} = 47.7 \text{ mN.m}^{-1}$, dynamic viscosity $\eta = 16.1 \text{ mPa.s}$, and density 1.15 g.cm^{-3}) on surfaces (length = 5 cm, width = 2 cm) patterned by microcontact printing. The surfaces were silicon wafers coated by a bilayer of 2 nm of chromium and a 10 nm layer of gold. First, a PDMS stamp was moulded on a striped master achieved by standard lithographic techniques [78]. Then a 1 mmol solution of octadecanethiol in hexane was poured onto the stamp. The stamp was applied to the surface and was followed by a quick wash with a 1 mmol solution of 1F, 1F, 2F, 2F perfluorodecanethiol in hexane. This resulted in alternating striped layers of octadecanethiol (0.8 mm) and perfluorodecanethiol (1.0 mm) on which the contact angles of ethylene glycol are 80° and 90° respectively. The rms roughness of the surfaces after patterning was $\sim 2 - 3 \text{ nm}$ as determined by AFM in contact mode.

A CCD camera (25 frames per second) linked to a computer was used to record the evolution of the drop after it had slid 3 cm from the top of the substrate. This ensured that a stationary regime had been reached. The images were then analyzed using ImageJ software, which allowed the position of the centroid of the drop to be followed as a function of time.

3.1.3 Results

First, as a simple test case, we present numerical results for two wide stripes ($\delta_1/R = \delta_2/R = 200/25 = 8.0$) of different contact angles, $\theta_1 = 110^\circ$ and $\theta_2 = 130^\circ$. The hydrophilic and hydrophobic stripes are labelled 1 and 2 respectively. Figs. 3.1(a) and 3.1(b) show the drop position as a function of time, and its velocity as a function of position respectively. Away from the borders between stripes the drop attains a constant velocity as expected. It moves

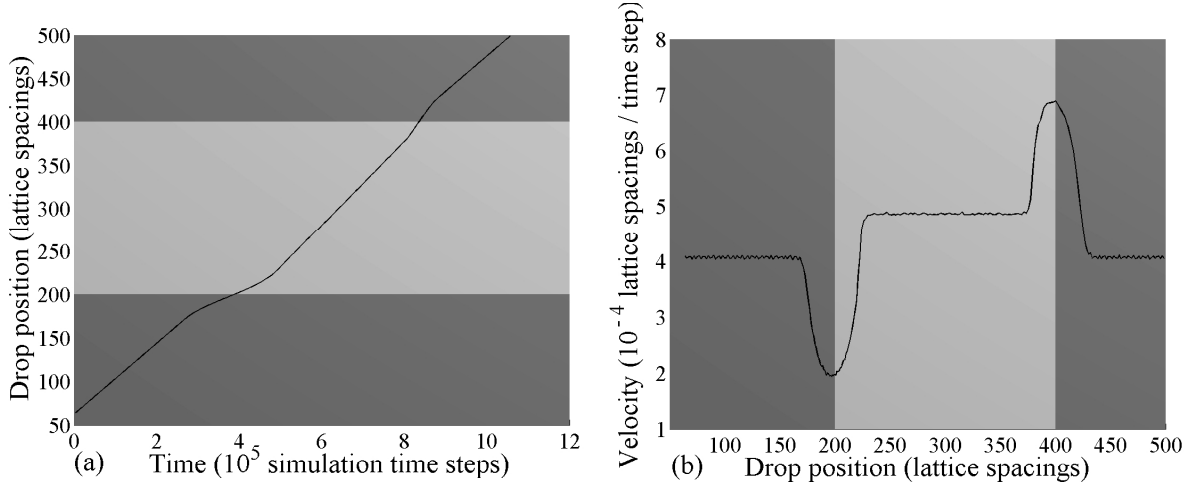


Figure 3.1: Drop dynamics on stripes wide compared to the drop diameter: (a) drop position as a function of time. (b) drop velocity as a function of position. Simulation parameters: $(L_x, L_y, L_z) = (400, 100, 80)$, $\theta_1 = 110^\circ$ (dark grey), $\theta_2 = 130^\circ$ (light grey), $\delta_1/R = 200/25 = 8$, $\delta_2/R = 200/25 = 8$, and $a_x = 10^{-7}$.

faster in the region of higher contact angle. This is because it is subject to a velocity profile which increases with height above the substrate; the higher the contact angle the further from the surface the drop centre of mass, and therefore the faster the drop moves.

As the drop moves from the hydrophilic to the hydrophobic stripe there is a pronounced dip in its velocity. This is due to the increase in the surface contribution to the free energy as the drop starts wetting the hydrophobic region. If the total force drops to zero we would expect the drop to remain pinned at the boundary. For the parameters we consider here, however, the applied force is strong enough to overcome pinning at the hydrophilic-hydrophobic boundary. Note also that there is a slight increase in the width of the drop along the y -direction as it reaches the hydrophobic boundary, as it prefers to spread on the hydrophilic substrate rather than move across onto the hydrophobic region of the surface. However this is disfavoured by the increase in the free energy of the liquid-gas interface and is, for the small difference in surface energies considered here, a minor effect. Similarly the competition between the attractive wetting force and the decreased efficiency of the applied force account for the peak in velocity as the drop passes back into the hydrophilic region.

We next consider the case where the stripe width is smaller than the drop diameter, $\delta_1/R = 33/25 = 1.32$ and $\delta_2/R = 27/25 = 1.08$, and the wettability contrast is not too large, $\theta_1 = 80^\circ$ and $\theta_2 = 90^\circ$. These parameters were chosen to match the experimental results as closely as possible. The case of a larger wettability contrast will be discussed later.

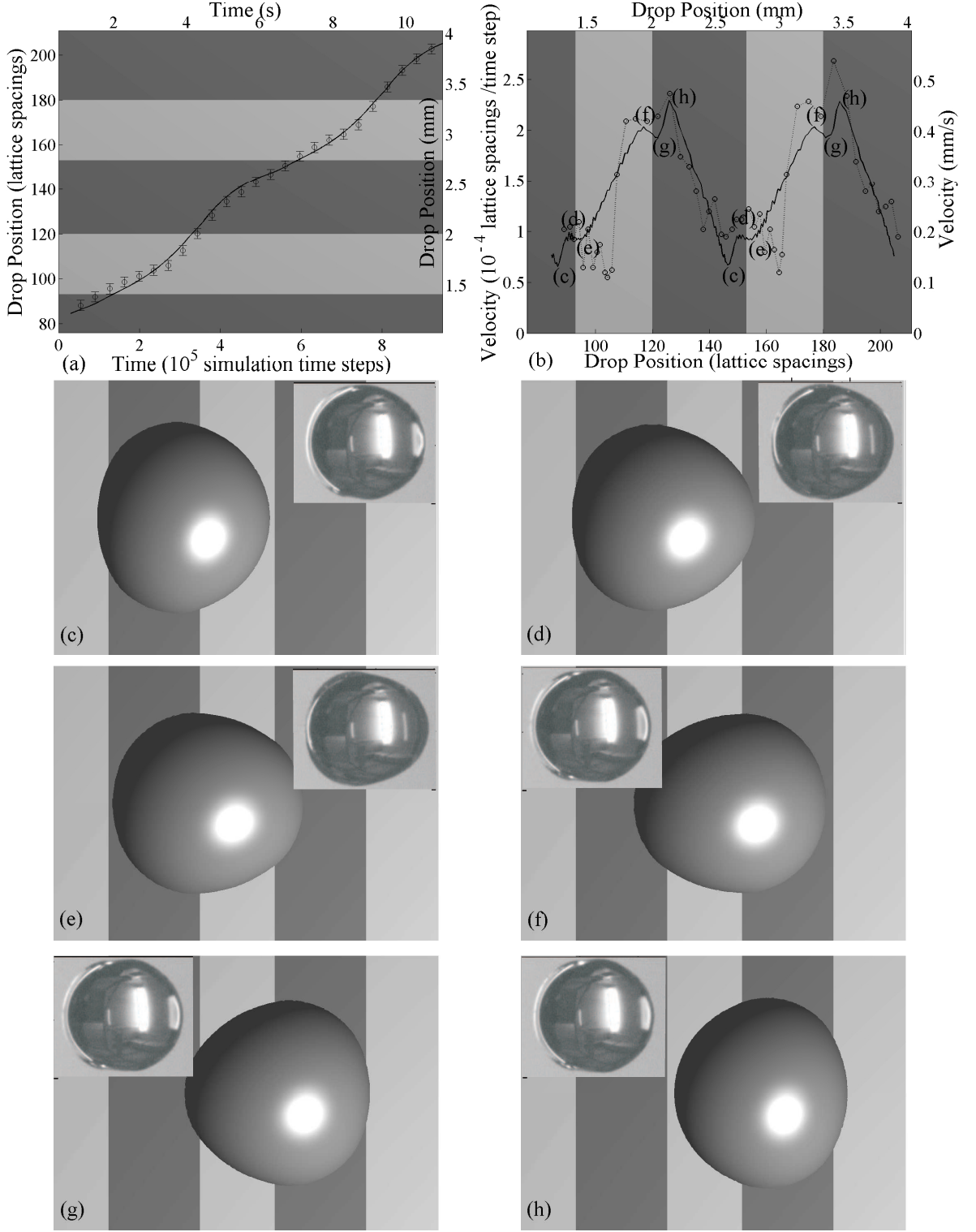


Figure 3.2: Drop dynamics on stripes smaller than the drop diameter and with a small contact angle variation between the stripes: (a) drop position as a function of time. The continuous line shows the simulation results and the circles are the experimental results. (b) drop velocity as a function of position. (c–h) drop morphology at positions indicated in (b). The large figures are simulations and the insets are the experimental results. Simulation parameters: $(L_x, L_y, L_z) = (180, 100, 80)$, $\theta_1 = 80^\circ$ (dark grey), $\theta_2 = 90^\circ$ (light grey), $\delta_1/R = 33/25 = 1.32$, $\delta_2/R = 27/25 = 1.08$, and $a_x = 5 \times 10^{-8}$.

We first describe the numerical results. In Fig. 3.2(a) the drop position is plotted as a function of time and Fig. 3.2(b) shows the drop velocity as a function of its position on the substrate. We also show, in Figs. 3.2(c–h), snapshots of the drop shape at designated points along its path. The first difference, when compared to the wider stripes, is that the drop never reaches a constant velocity. However, as expected, the periodicity of the substrate is reflected in the variation of the drop velocity with time. The broad features of the curves match those in Fig. 3.1(b) with the flat sections removed showing that the dynamics are again controlled by an interplay between the applied and wetting forces. The additional structure at the peaks and troughs of the velocity versus position graph occurs because the drop is traversing two stripe boundaries simultaneously.

We now compare to the experimental results. The simulation parameters were chosen so that the values of the liquid viscosity, the surface tension, the drop radius and the stripe widths in the simulations matched the experimental values. We also chose the (static) contact angles to take values of 80° and 90° .

The drop displacement as a function of time measured in the experiments is shown by the data points in Fig. 3.2(a). Photographs of the drop as it moves across the substrate are shown as insets in Figs. 3.2(c–h). There is a pleasing agreement between simulations and experiments.

However we caution that, as with all mesoscale approaches, it is not possible to match all the physical parameters and retain a stable and numerically feasible calculation. The interface is too wide in the simulations (relative to the drop radius) and the liquid–gas density difference is too small. The contact line velocity $u \propto \xi/(\Delta n)^2$ [27], where ξ is the interface width and Δn is the density difference. The drop therefore moves too quickly in the simulations. This problem is accounted for by rescaling the time axis. Another difference between the simulations and experiments is that experimental drops are not confined in a channel as in the simulations. However, we have chosen L_z/R sufficiently large that the drop feels a parabolic velocity profile akin to the experimental profile.

However, given these caveats, the agreement between simulation and experiment gives us confidence to explore the case of a larger contact angle difference between stripes which is more difficult to achieve experimentally. We take $\delta_1/R = 0.8$, $\delta_2/R = 2.0$, $\theta_1 = 60^\circ$ and $\theta_2 = 110^\circ$. We plot the drop position as a function of time and the drop velocity as a function of position in Figs. 3.3(a) and 3.3(b) respectively. Several authors [6, 59] have shown that

on such a substrate the drop can take either a ‘butterfly’ configuration where the drop spans the space between two hydrophilic stripes or a ‘diamond’ shape where the drop just lies on a single hydrophilic stripe. Strong deviations from spherical can now be favourable because the extra liquid–gas interface free energy is offset by the considerable advantage of lying on a hydrophilic stripe.

When a constant body force is applied, the drop moves across the surface and changes from a diamond to a butterfly shape and back again (Fig. 3.3(c–f)). Let us assume the drop is initially in a diamond configuration (Fig. 3.3(f)). Due to the Poiseuille flow field, the drop is pushed forward onto the hydrophobic region. Its velocity decreases because of the dewetting force at the hydrophobic stripe. If the external body force is small, the drop velocity will fall to zero, the drop will be pinned, and the steady-state drop shape will look similar to Fig. 3.3(c). For the parameters we consider here, however, the drop is just able to channel to the next hydrophilic stripe. The effective capillary force at the hydrophobic-hydrophilic border then starts to take charge and the drop accelerates and wets the next hydrophilic stripe. The drop now has a butterfly shape (Fig. 3.3(d)) and is at the peak of an energy barrier between two diamond shapes on successive hydrophilic stripes. It then becomes more advantageous for the drop to spread along the new hydrophilic stripe in the y -direction than to continue to move along the substrate. Hence the diamond configuration is re-formed and the oscillations repeat.

3.2 Controlling Drop Size and Polydispersity Using Chemically Patterned Surfaces

Recent experiments on biosystems have shown that these systems have evolved to use surface patterning to direct the motion of fluids at surfaces. Examples include plants where micron-scale bumps on the leaves lead to superhydrophobic behaviour [8, 79], desert beetles who use hydrophilic patches on their back to collect dew [80], and butterfly wings which are patterned anisotropically to promote directional run-off [10]. Similar surface patterning have also been exploited in the design of microfluidic devices. For example, Zhao *et al.* [81, 82] have used chemically patterned stripes inside microchannels to control the behaviour of liquid streams and Handique *et al.* [83] have used a hydrophobic surface treatment to construct a device which can deliver a fixed volume of fluid. Our aim in this section is to use numerical simulations to further demonstrate ways in which chemically patterned surfaces can be used to manipulate the

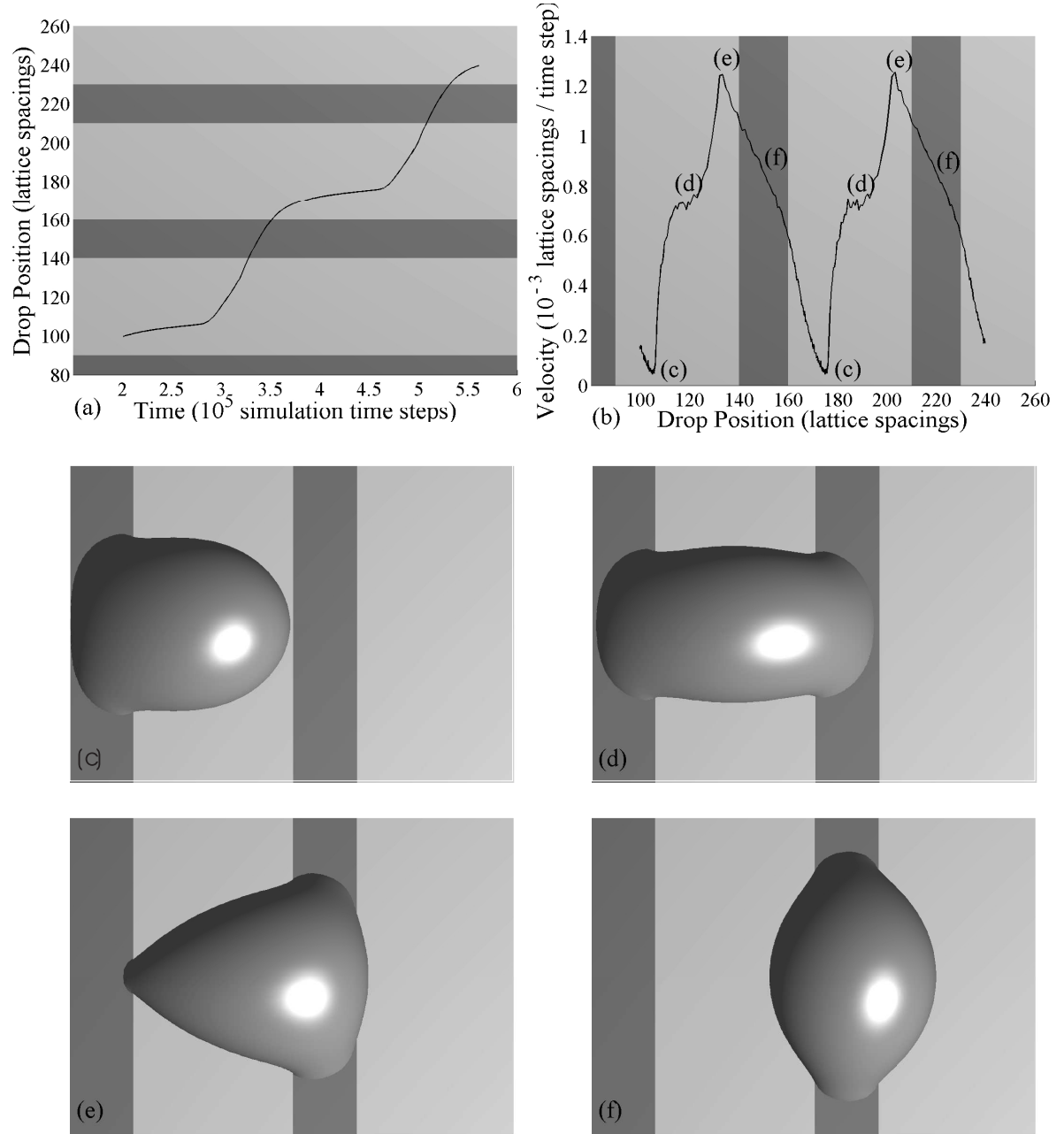


Figure 3.3: Drop dynamics where there is a large contact angle variation between the stripes: (a) drop position as a function of time. (b) drop velocity as a function of position. (c–f) drop morphology at positions indicated in (b). Simulation parameters: $(L_x, L_y, L_z) = (140, 100, 80)$, $\theta_1 = 60^\circ$ (dark gray), $\theta_2 = 110^\circ$ (light gray), $\delta_1/R = 20/25 = 0.8$, $\delta_2/R = 50/25 = 2.0$, and $a_x = 2.5 \times 10^{-7}$.

behaviour of micron-scale drops, demonstrating that they provide a useful tool for exploring device designs.

We propose two ways in which chemically patterned surfaces can be used to control drop size and polydispersity. The drop sorter takes a collection of polydisperse drops as input and separates them into different channels based on their size or wetting properties. The drop generator allows small polydisperse drops to coalesce, pinning the resultant drop until it reaches a critical volume.

Most drop sorting techniques available in the literature involve active actuation to control the motion of the drops. This can be done by (but is not limited to) electro-osmotic [68], mechanical [69], optical [70], or dielectrophoretic [71] manipulation. Our proposed devices are passive devices, which require neither a detection nor switching mechanism. Tan *et al.* [72] make use of the channel geometry to control the flow and hence sort drops by their size. Here we propose a different drop sorting device which uses chemical surface patterning to separate the liquid drops. Since a given surface is wet differently by different liquids, our proposed method can be used to separate drops based on their wetting properties, size, or both.

Active [73, 74] and passive [75–77] drop generating techniques are known in the literature, but to the best of our knowledge, they are mostly concerned with generating liquid drops from continuous streams or larger sample drops. Here, we look at the problem from a different angle and suggest how monodisperse liquid drops can be formed from small polydisperse drops.

3.2.1 Sorting Drops by Size and Wetting Properties

To use chemical patterning to sort drops according to size or wettability we consider the design in Fig. 3.4. A surface is patterned with a rectangular grid of hydrophilic (relative to the background) stripes. A drop is input to the device at A and subject to a body force at an angle $< 45^\circ$ to the x -axis. The system is confined in a channel of height L_z .

The path taken by the drop through the device depends on the drop contact angles with the substrate and the strength of the body force. It also, of particular relevance to us here, depends on the width of the stripes relative to the drop radius. By choosing the stripes along the y direction to be of equal widths, but those along x to increase in width with increasing y , drops of different sizes move along different paths with the larger drops moving further along the y direction.

Fig. 3.5(a)-(c) show simulations of the paths of drops of initial radius $R = 25, 26$ and 29

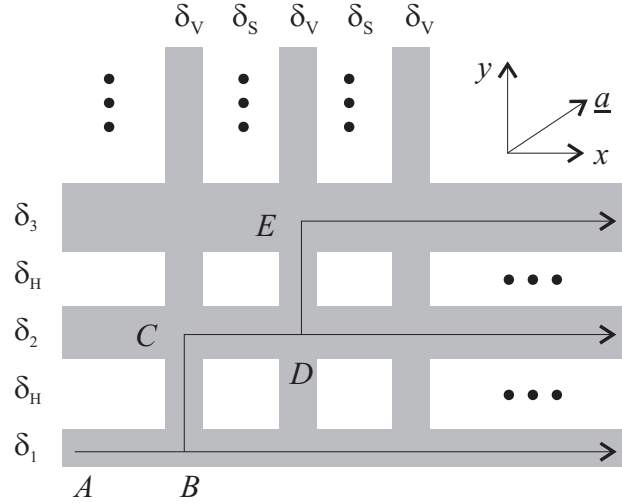


Figure 3.4: Schematic diagram of a drop sorter. The grey stripes on the surface are hydrophilic with respect to the background. δ labels the widths of the stripes and \underline{a} the imposed acceleration. The arrows show possible paths of a drop through the device.

moving through such a device. The simulation parameters are: $\theta_{\text{philic}} = 60^\circ$, $\theta_{\text{phobic}} = 110^\circ$, $L_z = 80$, $a_x = 3.0 \times 10^{-7}$, $a_y = 2.0 \times 10^{-7}$, dynamic viscosity $\eta = 0.4128$, $\sigma_{LG} = 7.7 \times 10^{-4}$, drop density $n_l = 4.128$, $\delta_1 = 20$, $\delta_2 = 30$, $\delta_3 = 40$, $\delta_V = 20$, $\delta_H = 80$, and $\delta_S = 200$. The drop velocity is measured to be $\sim 5 \times 10^{-3}$. Comparing the simulation results with experiments for a simpler surface pattern in section 3.1, we established a mapping between simulation and physical units, except that the drops move too fast by a factor of ~ 500 in the simulations (for the liquid gas model). Taking into account this empirical factor, the parameters used here correspond to dimensionless numbers: $Re = n_l v R / \eta \sim 3 \times 10^{-3}$, $Ca = \eta v / \sigma_{LG} \sim 6 \times 10^{-3}$, and $Bo = n_l a R^2 / \sigma_{LG} \sim 1.2$.

When a submillimetric drop of initial radius R is jetted on a flat homogeneous substrate, it will relax to form a spherical cap with a contact angle given by the Young's law. This is however not generally the case on chemically patterned surfaces. The equilibrium drop shape at A is elongated in the x -direction because the drop prefers to wet the hydrophilic stripe. The introduction of the body force will further deform the drop shape so that it is no longer symmetric in either the x or the y -directions. Indeed, the drop will be confined in a hydrophilic stripe only if the effective capillary force is able to counterbalance the imposed body force.

In cases where the drops are confined in the δ_1 stripe, they will move in the x -direction from A to the cross-junction B , where their paths may diverge. In order for a drop to move in the y -direction, the capillary force in this direction must be large enough to overcome the sum of the capillary force and the excess external body force in the x -direction (recall $a_x > a_y$).

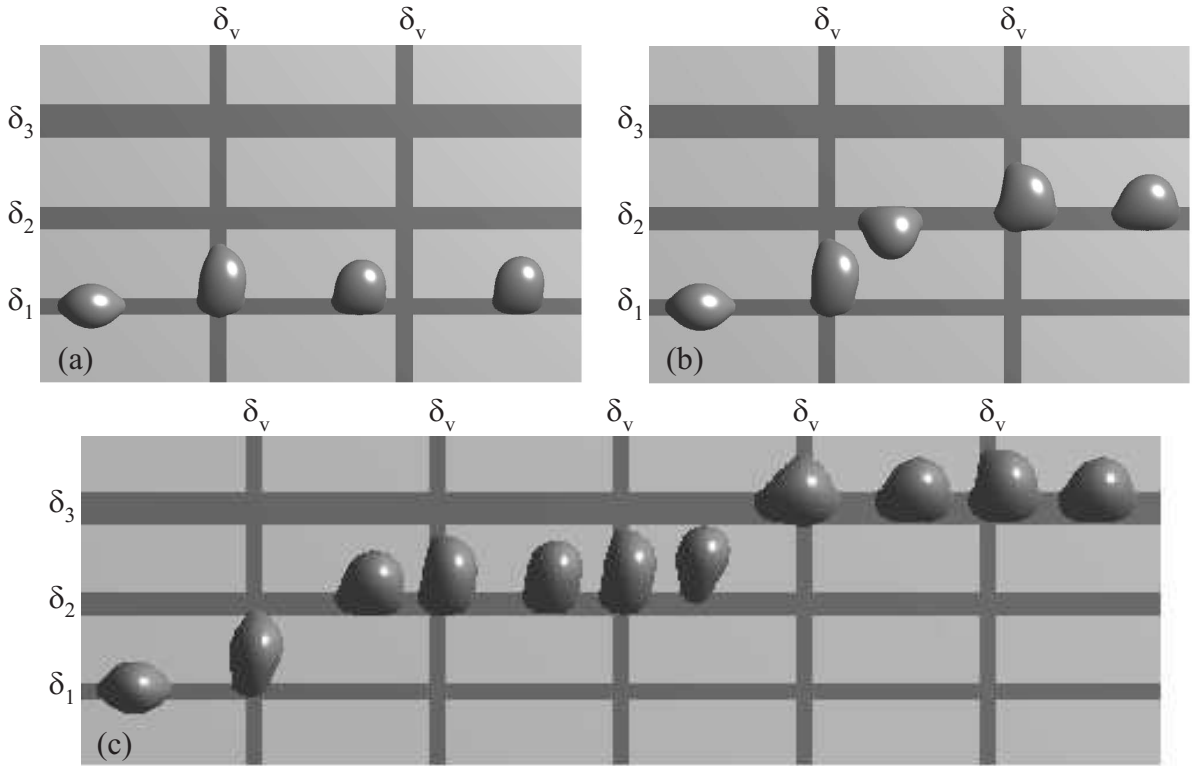


Figure 3.5: Paths taken by drops of radius (a) $R = 25$, (b) $R = 26$, and (c) $R = 29$ through the drop sorter. $\delta_1 = 20$, $\delta_2 = 30$, $\delta_3 = 40$, and $\delta_V = 20$

This is where the asymmetry of the drop shape comes into play. As the volume of the drop is increased, a larger fraction of it overhangs the stripes and hence a larger fraction will interact with the hydrophilic stripe along the y -direction at the junction. This increases the capillary force along y and means that larger drops (e.g. $R = 26$) will move in the y -direction to point C , whereas smaller drops (e.g. $R = 25$) will continue to move along x .

Since $a_x > a_y$ and $\delta_2 > \delta_V$ the asymmetry of the drops' shape guarantees that drops at C move to D . If the widths of the stripes along x were all the same the drops would then move from D to E for the same reason that they moved from B to C . However, increasing the stripe width so that $\delta_2 > \delta_1$ reduces the effective capillary force in the y -direction and therefore some of the drops (e.g. $R = 26$) continue to move along x whereas larger drops are routed around the corner towards the third stripe. Hence the drops are sorted by size.

Fig. 3.5(c) shows the path of a drop of radius $R = 29$ through the device. Although it does move up to the third stripe it has to pass several junctions before it does so. This occurs because the drop takes time to relax to its steady state shape as it moves along the δ_2 stripe – note that the drop morphology is slightly different as it crosses the second and third vertical

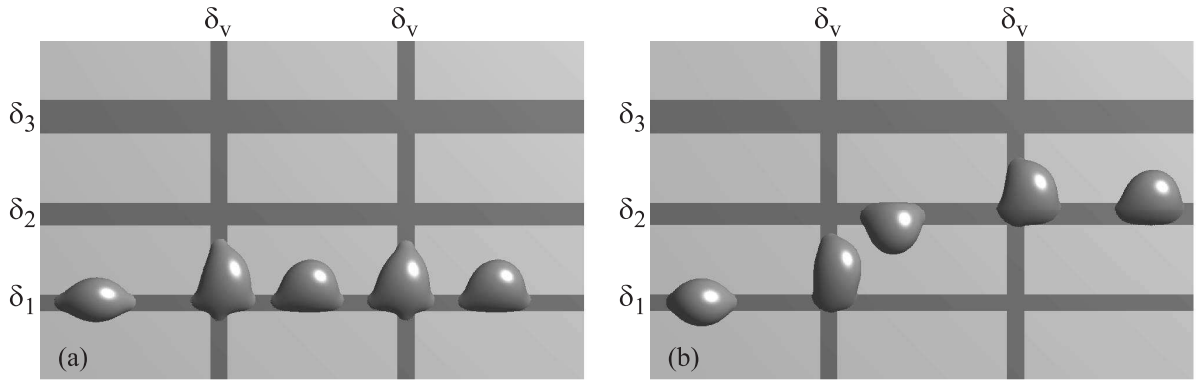


Figure 3.6: The paths taken by drops of radius $R = 26$ through the drop sorter, where the contact angle of the drops on the hydrophilic stripes is (a) $\theta_{\text{philic}} = 40^\circ$ and (b) $\theta_{\text{philic}} = 60^\circ$.

stripes, with a slightly increased overhang at the latter. Ideally the distance between two vertical hydrophilic stripes should have been longer to overcome this effect.

These simulations suggest that by increasing the number of stripes and carefully controlling their widths it may be possible to sort polydisperse drops into collections of monodisperse drops. The precision with which this can be done is determined by the increase in the stripe widths. Here the vertical stripe width is fixed. As a result $(R_{n+1} - R_n) > (R_n - R_{n-1})$. $(R_{n+1} - R_n) \sim (R_n - R_{n-1})$ can be achieved by increasing the vertical stripe width with increasing x . Two other parameters, the wettability contrast and the external body force, could also be adjusted to fine-tune the device.

This design can also be applied to sort drops of similar size that possess different wetting properties. Returning to Fig. 3.4 all the drops will move to the right from point *A* to point *B*. Drops with a lower contact angle on the stripes will overhang the stripes less. Hence at *B*, these drops will interact less with the stripes along y and will continue to move along x . As the contact angle of the drops increases they will feel more effect from the junction and, at some threshold wettability, they will turn the corner to move along y . As shown in Fig. 3.6, we find that for drops of radius $R = 26$ the drop moves along stripe δ_1 for $\theta_{\text{philic}} = 40^\circ$ but is diverted to stripe δ_2 for $\theta_{\text{philic}} = 60^\circ$, with other simulation parameters as before.

The current device speed and throughput are limited by the need to eliminate unwanted drop coalescence. For example, in the drop sorter, drops of different sizes and wetting properties move at a different speed. If two drops are entered too closely together, it may lead to a situation where the two drops coalesce and mix instead of being sorted.

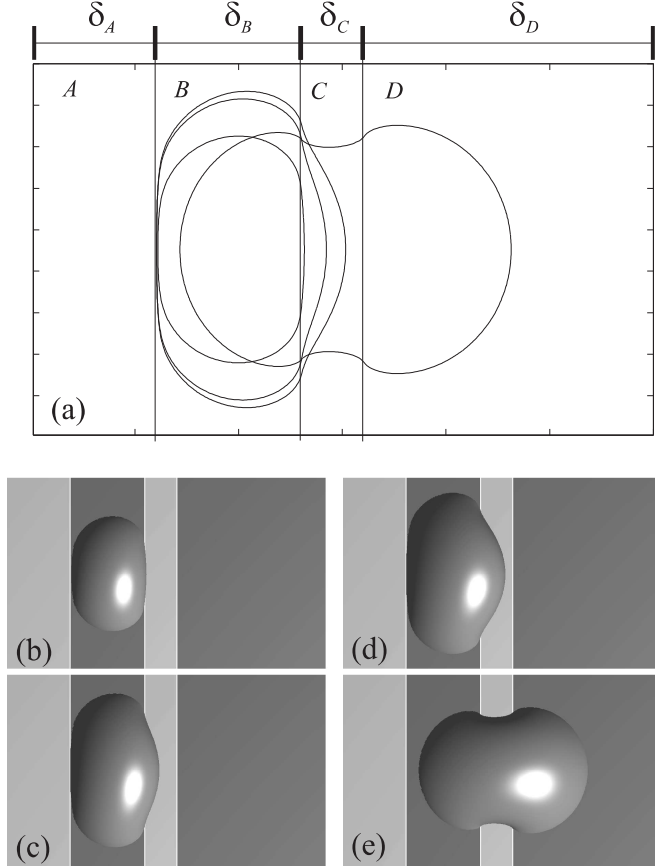


Figure 3.7: Simulations showing the evolution of the drop shape and position with time in the drop generator. (a) Contour plot as volume is added to the system. (b)–(e) Snapshots as volume is added. (b) $V = 1.2 \times 10^5$. (c) $V = 2.6 \times 10^5$. (d) $V = 3.3 \times 10^5$. (e) $V = 4.1 \times 10^5$

3.2.2 Generating Monodisperse Drops

As a second example we demonstrate how suitable chemical patterning can be used to generate monodisperse drops. In Fig. 3.7(a) regions A and C are hydrophobic to the drop relative to regions B and D . For simplicity, we take $\theta_A = \theta_C = 110^\circ$ and $\theta_B = \theta_D = 60^\circ$. Polydisperse drops are input to the system in region A and subject to an external body force in the x -direction. If the applied body force is large, all drops will exit the system at region D without change.

If the body force is small, however, the effective capillary force at the B – C border can balance the external force and the drops are trapped in the hydrophilic stripe. As more and more polydisperse drops coalesce at the B – C border, the resultant drop will no longer be confined to the hydrophilic stripe. A fraction of the drop volume will start to occupy the hydrophobic region. At a certain critical volume, the front end of the drop will reach the D

region and the drop will tunnel from B to D . This is shown in Fig. 3.7 where we have presented the lattice Boltzmann simulation results for the following set of parameters: $\delta_A = 60$, $\delta_B = 70$, $\delta_C = 30$, $\delta_D = 140$, and $a_x = 10^{-7}$. Other parameters remain the same as in the previous subsection.

The accuracy with which it is possible to control the final drop size is dependent on the ratio between the average input drop volume to that of the generated output drop: the smaller the ratio the better the accuracy. There are three key parameters that can be used to tune the generated drop volume: the wettability contrast, the stripe widths, and the external body force. Increasing either the wettability contrast or the stripe widths will increase the effective capillary force, and hence increase the final drop volume. Increasing the body force will have the opposite effect, resulting in a smaller output drop. It is also important to tune the input drop frequency. If the frequency is too high then a number of input drops will coalesce with the resultant drop as it moves from region B to D .

3.3 Discussion

We have presented numerical and experimental results following the dynamics of micromscale drops moving across a chemically patterned surface. In section 3.1, we showed that the drop behaviour is determined by the balance between the driving force and the variation in the surface force as the drop moves between regions of different wettability. As the wettability contrast increases there are large deviations of the drop shape from spherical as it moves across the surface. We also found a close agreement between results of the lattice Boltzmann simulations and experiments. Therefore we hope that the numerical approach will provide a useful tool for designing new ways of controlling the motion of liquid drops on patterned surfaces for applications in areas such as microfluidics and ink-jet printing.

With this in mind, we explore numerically in section 3.2, the feasibility of using chemical patterning to control the size and polydispersity of micron-scale drops. The simulations suggest that it is possible to sort drops by size or wetting properties by using an array of hydrophilic stripes of different widths. We also demonstrate that monodisperse drops can be generated by exploiting the pinning of a drop on a hydrophilic stripe. The latter has recently been demonstrated experimentally by Fidalgo *et al.* [84].

Since capillary phenomena are increasingly important for systems with large surface to

volume ratio, passive microfluidic devices based on surface chemical patterning can play an important role in the future, particularly as the devices are downscaled. Careful designs of capillary networks may even lead to an integrated device, where drop generation, sorting, mixing, and delivery can all be done on a single chip. We further note that it is an intriguing idea to incorporate electrowetting [85,86] into both devices, adding active control, flexibilities, and functionalities. Such devices are not limited to the liquid-gas system considered in this chapter. The designs can be used for both a liquid-liquid and liquid-gas system, and in both open and closed channels. Recently, Balazs and co-workers [87,88] have used similar ideas to sort microcapsules based on their mechanical or chemical properties.

CHAPTER 4

Modelling Contact Angle Hysteresis on Patterned Surfaces

“All models are wrong, but some are useful.”

- George Box

Our aim in this chapter is to investigate contact angle hysteresis on chemically patterned and superhydrophobic surfaces. For a surface that is flat and chemically homogeneous, a liquid drop will form a spherical cap with a contact angle θ given by Young’s law [1]

$$\cos \theta = \frac{\sigma_{GS} - \sigma_{LS}}{\sigma_{LG}}, \quad (4.1)$$

where σ_{GS} , σ_{LS} and σ_{LG} are the gas–solid, liquid–solid and liquid–gas surface tensions respectively.

Real surfaces are, however, neither perfectly flat nor chemically homogeneous. These inhomogeneities result in the existence of multiple local free energy minima, not just the global minimum prescribed by Young’s formula (4.1). This can cause pinning of the contact line and lead to drop shapes which depend not only on the thermodynamic variables describing the state of the drop, but also on the path by which that state was achieved. This phenomenon is known as contact angle hysteresis.

There are several different manifestations of contact angle hysteresis commonly reported in the literature and it is important to distinguish clearly between them. One favoured experimental approach to measure the contact angle of a drop is to slowly increase the volume until the drop starts to spread. The angle at which spreading occurs, which corresponds to the drop being able to cross any free energy barrier which impedes its motion, is termed the advancing

contact angle. Similarly, as the drop volume is quasi-statically decreased, the contact line first moves at the receding contact angle. The difference between the advancing and receding contact angles is the contact angle hysteresis, zero for a perfect substrate, but possibly 10° or more, and notoriously difficult to measure, for a real surface. We shall concentrate on this set-up here and shall term it unforced, static hysteresis.

It is also possible to push a drop across a surface and measure the advancing angle, at the front of the drop, and the receding contact angle, at the rear, when it first moves. We shall refer to this case as forced, static hysteresis and comment on it further in the discussion. However it is important to point out that the measured unforced and forced contact angle hysteresis for a given drop on a given surface need not necessarily be the same as a forced drop will be deformed and the free energy barriers will depend on the shape of the drop.

In the literature there is also mention of dynamic contact angle hysteresis, the difference in angles at the front and rear of a moving drop. This is again a different situation, which cannot be treated by equilibrium statistical mechanics, and we shall not consider it further here.

Understanding contact angle hysteresis quantitatively is not easy because it depends on the details of the surface inhomogeneities which will, in general, be random in position and size. However recent advances have allowed surfaces to be fabricated with well-defined chemical patterning – areas of differing contact angle – which can be varied in size relative to the size of a drop (e.g. [6, 56, 57]). This is allowing more quantitative measurements of how advancing and receding contact angles, and contact angle hysteresis, depend on the details of the surface patterning.

Another exciting development is the fabrication of superhydrophobic surfaces [7, 12, 24, 89]. As we have described in the Introduction, drops can either lie in a suspended, or Cassie-Baxter [11], state on top of the posts or a collapsed, or Wenzel [15], state filling the interstices between them. Moreover, drops can roll very easily on these surfaces [7, 24, 89–91] and contact angle hysteresis is important in understanding why. It is of interest to ask how the position, size and spacing of the posts affects the hysteresis, questions which have caused some controversy in the literature [89–93], for example whether contact angle hysteresis is primarily a surface (e.g. [92]), or a contact line (e.g. [89–91, 93]), effect. Very recent experiments by Dorrer *et al.* [94] show that the advancing contact angle is constant, while the receding contact angle varies as a function of the post size and spacing.

The role of free energy barriers in contact angle hysteresis has been known for some

time [95–109]. Several authors have considered the two dimensional (or axisymmetric three dimensional) problem of a drop moving over chemically striped surfaces [96, 97], sinusoidal surfaces [98–101], or surfaces with posts [102, 103] using analytic or numerical techniques to minimise the free energy. Extensions to three dimensions have also been attempted [97, 104–109]. These efforts include surfaces with random isolated heterogeneities [106], striped patterns [107], and regular lattices of posts [108, 109] or chemical patches [97, 104, 105]. The common themes in all these works are the pinning of the contact line, the existence of multiple local energy minima, and the occurrence of a slip-jump-stick behaviour.

In this chapter we investigate contact angle hysteresis on chemically patterned and superhydrophobic surfaces, as the drop volume is quasi-statically increased and decreased. We consider both two (cylindrical drops), and three (spherical drops), dimensions using analytical and numerical approaches to minimise the free energy of the drop. The numerical results are obtained using the liquid gas model described in section 2.1. To implement unforced static hysteresis in our lattice Boltzmann simulations, we need to slowly increase or decrease the drop volume. To do this we vary the drop liquid density by $\pm 0.1\%$. This in turn affects the drop volume as the system relaxes back to its coexisting equilibrium densities.

In two dimensions, on a surface striped with regions of different equilibrium contact angle, θ_e , we find, in agreement with other authors [96, 97], a slip, jump, stick motion of the contact line. The advancing and receding contact angles are equal to the maximum and minimum values of the θ_e respectively. In three dimensions these values provide bounds, but the contact angle hysteresis is reduced by the free energy associated with surface distortion [104–106]. A stick, slip, jump behaviour persists, but we caution that the definition of a single macroscopic contact angle is problematic for patterns of order the drop size. The position and magnitude of the contact line jumps are sensitive to the details of the surface patterning and can be different in different directions relative to that patterning.

For drops suspended on superhydrophobic surfaces we find that, in two dimensions, the advancing contact angle is (ideally) 180° , in agreement with [102] and the receding angle is θ_e , the intrinsic contact angle of the surface. For collapsed drops in two dimensions the advancing contact angle is also 180° but the receding angle is $\theta_e - 90^\circ$ because the contact line has to dewet the sides of the posts. In three dimensions, for both suspended and collapsed drops, the advancing angle remains close to 180° [89–91, 94, 108], but the receding contact angle is increased. However, the receding angle still remains considerably smaller for the collapsed

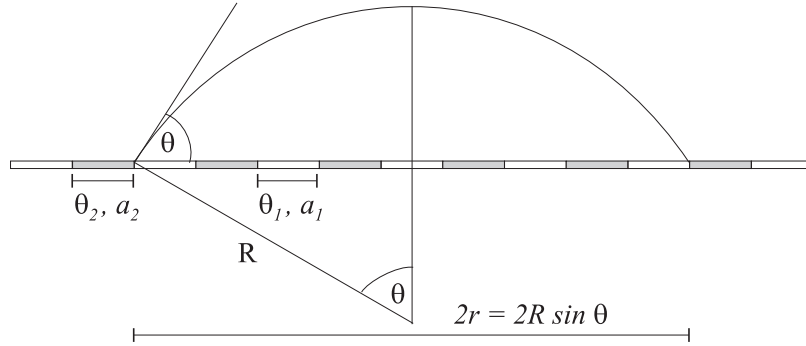


Figure 4.1: Schematic diagram of a cylindrical drop

state and the contact line pinning is much stronger for the collapsed state. As a result, the hysteresis of suspended drops is, in general, much smaller than that of collapsed drops on the same surface. Again we argue that a simple average over the disorder is not sufficient to predict the details of the contact angle hysteresis.

4.1 Two Dimensional Drop on a Chemically Patterned Surface

In this section we shall investigate a two-dimensional situation, the hysteresis of a cylindrical drop spreading over a chemically striped surface, where an analytic solution is possible. We shall demonstrate that the contact line shows a stick, jump, slip behaviour and that the advancing and receding contact angles are equal to the maximum and minimum equilibrium contact angles of the surface respectively. We also show that lattice Boltzmann simulations reproduce the analytic results well.

Consider a cylindrical drop with a *macroscopic* contact angle θ that forms a spherical cap of radius R as shown in Fig. 4.1. (Note that we reserve θ_e , θ_A , and θ_R to describe the *equilibrium*, *advancing*, and *receding* contact angles on a given surface.) The base length of the drop is $2r = 2R \sin \theta$. The drop volume per unit length is

$$S = r^2 \frac{\theta - \sin \theta \cos \theta}{\sin^2 \theta} \quad (4.2)$$

and therefore, for a drop at constant volume,

$$r \frac{\sin \theta - \theta \cos \theta}{\sin^2 \theta} d\theta = \frac{\sin \theta \cos \theta - \theta}{\sin \theta} dr. \quad (4.3)$$

The liquid–gas surface area per unit length is

$$L_{LG} = \frac{2r\theta}{\sin\theta}. \quad (4.4)$$

The important contributions to the free energy per unit length of the cylindrical drop come from the interfacial terms:

$$F = \sigma_{LG} L_{LG} + \int (\sigma_{LS} - \sigma_{GS}) dx, \quad (4.5)$$

where the integral is taken over the substrate. Using Young's equation (4.1) the reduced free energy follows as

$$f = F/\sigma_{LG} = \frac{2r\theta}{\sin\theta} - \int \cos\theta_e(x) dx. \quad (4.6)$$

We consider, as in [96, 97], the simple case where a drop is lying on a surface regularly patterned with (relatively) hydrophilic stripes with equilibrium contact angle $\theta_e = \theta_1$ and width a_1 and (relatively) hydrophobic stripes with parameters $\theta_e = \theta_2$ and width a_2 . Let us further assume that the contact line is initially lying on a hydrophilic stripe. Our aim is to discuss the motion of the contact line as the drop volume slowly increases. The drop initially lies at an angle $\theta = \theta_1$ with respect to the solid surface. As the volume is increased the contact line moves in order to keep the contact angle at a value $\theta = \theta_1$. This remains true until the contact line reaches the chemical border between stripes. It will then be pinned as it costs free energy for the drop to spread onto the more hydrophobic stripe. The contact line will continue to be pinned until the free energy cost of distorting the liquid–gas interface exceeds the surface energy gain. We demonstrate that, as expected, this occurs when $\theta = \theta_2$ [96, 97].

From Eq. (4.6) we may write the reduced free energy of the drop as

$$f = F/\sigma_{LG} = \frac{2r\theta}{\sin\theta} - (2k+1)a_1 \cos\theta_1 + 2ka_2 \cos\theta_2 + 2x a_2 \cos\theta_2 \quad (4.7)$$

where k is an integer and $0 < x < 1$. Moving the drop a small distance $dr = a_2 dx$ onto the hydrophobic stripe the free energy changes by

$$df = 2r \frac{\sin\theta - \theta \cos\theta}{\sin^2\theta} d\theta + \frac{2\theta}{\sin\theta} dr - 2 \cos\theta_2 dr \quad (4.8)$$

which, using the constant volume constraint (Eq. (4.3)) can be rewritten

$$df = 2(\cos \theta - \cos \theta_2) dr. \quad (4.9)$$

Hence $df/dr < 0$ and the drop depins when $\theta > \theta_2$.

Increasing the volume further the drop contact line moves with a constant contact angle $\theta = \theta_2$. Once the drop reaches the hydrophobic–hydrophilic chemical border it can lower its free energy by immediately spreading onto the hydrophilic stripe. It will either move to a position where the contact angle has returned to θ_1 or to the next hydrophilic–hydrophobic boundary, whichever is reached first. In the particular example we show below, the latter is the case and the contact line becomes pinned at the next hydrophilic–hydrophobic border, with a contact angle $\theta_2 < \theta < \theta_1$.

The free energy (4.6) of the advancing drop is illustrated in Fig. 4.2(a) for $a_1/a_2 = 1$, $\theta_1 = 30^\circ$ and $\theta_2 = 60^\circ$. The dashed lines show the free energy of the drop pinned at successive hydrophilic–hydrophobic boundaries as the drop volume is increased. The solid line shows the path in free energy space taken by the drop as it spreads with a contact angle $\theta = \theta_2$. At A the drop reaches, and immediately wets the hydrophilic stripe corresponding to a sudden fall in free energy. It reaches the hydrophobic boundary and remains pinned along AB. At B the contact angle attains the value θ_2 and the drop spreads across the hydrophobic stripe, reaching the next hydrophilic stripe at A'. The solid lines in the inset in Fig. 4.2(a) show the drop profiles at A, B and A'. The dashed lines in the inset correspond to the drop profiles at A and A' immediately before contact line jumps occur. The drop base length and contact angle as a function of volume are plotted for the advancing contact line in Fig. 4.2(b) and (c). The stick, slip, jump behaviour will be a recurrent theme for all the substrates we consider.

Similar reasoning can be applied to understand the dynamics of the receding contact line. Free energy curves for this case are shown in Fig. 4.3(a). (As this is the receding contact angle, the correct way to read the plot is from right to left.) Assume that the contact line is initially placed on the hydrophobic stripe with $\theta = \theta_2$. As the volume of the drop is reduced, the contact line will recede smoothly to the hydrophobic–hydrophilic border where it remains pinned until $\theta = \theta_1$ [96, 97] (along AB in Fig. 4.3(a)). The contact line then continues to move along the hydrophilic stripe with contact angle θ_1 (BA'). A sudden jump occurs when it reaches the hydrophilic–hydrophobic border as the drop can lower its free energy by dewetting

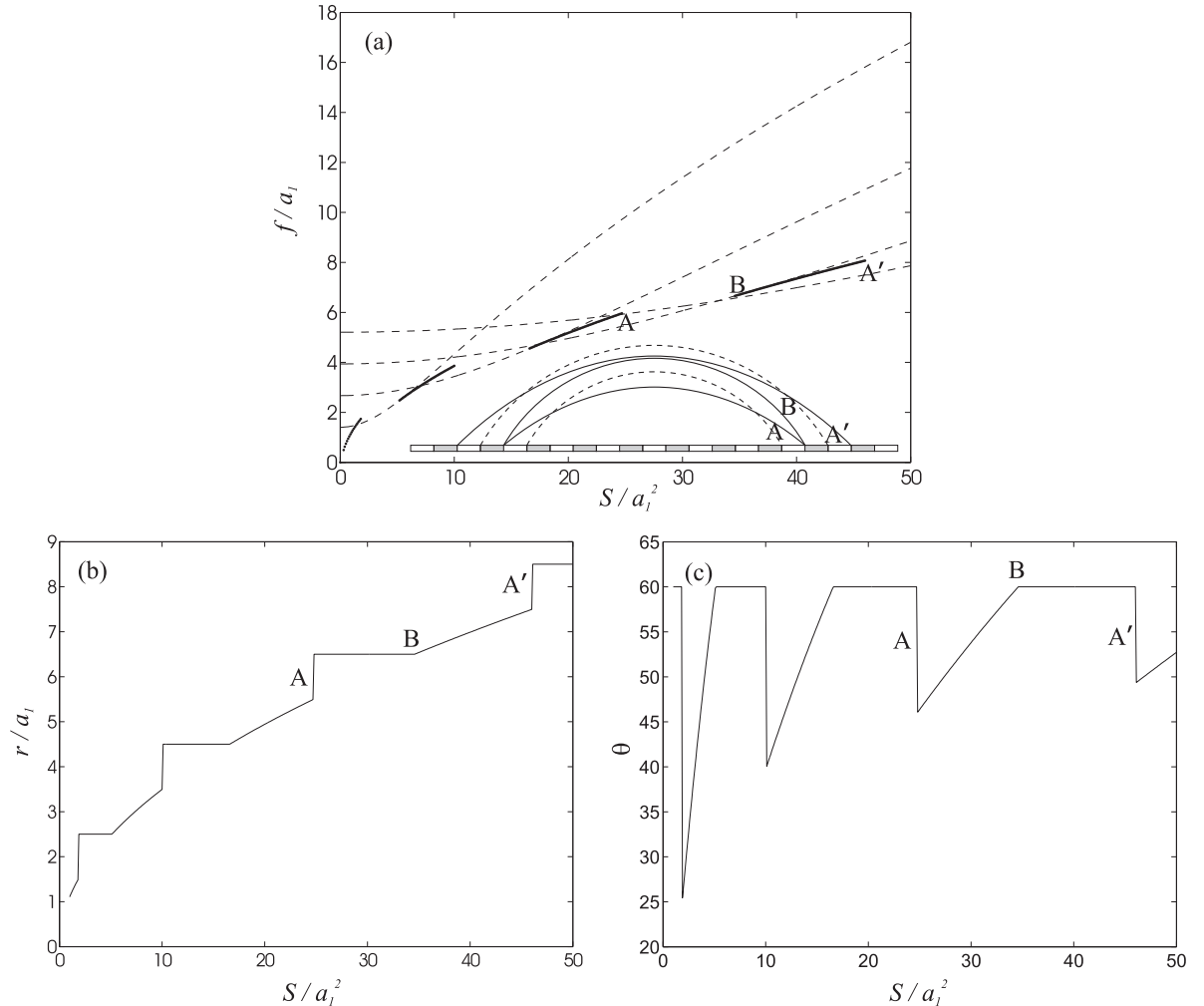


Figure 4.2: The dynamics of the advancing contact line for $a_1/a_2 = 1$, $\theta_1 = 30^\circ$ and $\theta_2 = 60^\circ$. (a) Free energy, (b) drop radius, and (c) macroscopic contact angle as a function of drop size. A and A': the contact line immediately wets the hydrophilic stripe. AB: the contact line is pinned until $\theta = \theta_2$. BA': the contact line advances with $\theta = \theta_2$. The inset in (a) summarises the evolution of the drop shape. The solid lines in the inset show the drop profiles at A, B and A', while the dashed lines correspond to the drop profiles at A and A' immediately before contact line jumps occur.

the hydrophobic stripe (at A' in Fig. 4.3(a)). The inset in Fig. 4.3(a) show the profile of the drop as its volume is reduced. The drop base length and contact angle as a function of volume are shown in Fig. 4.3 (b) and (c).

Fig. 4.4 shows a typical hysteresis curve: the variation of the macroscopic contact angle as the volume is increased, then decreased. Diagonal, horizontal, and vertical lines correspond to the drop sticking, slipping, and jumping respectively. The data points are results from the lattice Boltzmann simulations, while the solid line corresponds to the analytical calculations. The contact line dynamics is well captured by lattice Boltzmann simulations, though contact line jumps occur earlier in lattice Boltzmann simulations than one would expect from the analytical expressions. This is because the numerical interface has a finite width, typically ~ 3 lattice spacings.

We can conclude that for unforced hysteresis on a two dimensional chemically striped surface, the advancing contact angle $\theta_A = \theta_e|_{\max}$ and the receding contact angle $\theta_R = \theta_e|_{\min}$. If we return to the free energy curves in Fig 4.2(a) and 4.3(a), paths AB and BA' are reversible. Even though contact line pinning is observed there, the contact angle is unique for a given drop volume. It is the free energy jumps at A and A' that make contact angle hysteresis an irreversible phenomenon.

4.2 Three Dimensional Drop on a Chemically Patterned Surface

In section 4.1, we showed that $\theta_A = \theta_e|_{\max}$ and $\theta_R = \theta_e|_{\min}$ for a two dimensional drop on a chemically striped surface. We now turn to three dimensions. Here we find that the values of the advancing and receding contact angles are strongly dependent on the details of the surface patterning. Therefore we shall focus on the general aspects of the hysteresis, particularly those not captured by the two dimensional model described in section 4.1, rather than quantitative details. The drops no longer form spherical caps so analytic results are not possible without serious approximation. Our arguments will be illustrated by numerical results obtained using lattice Boltzmann simulations.

The chemically patterned surface we consider is shown diagrammatically in Fig. 4.5. Squares of side $a = 12$ are separated by a distance $b = 5$. In the first case that we consider (surface A), the equilibrium contact angle of the squares is taken as $\theta_1 = 110^\circ$, while that

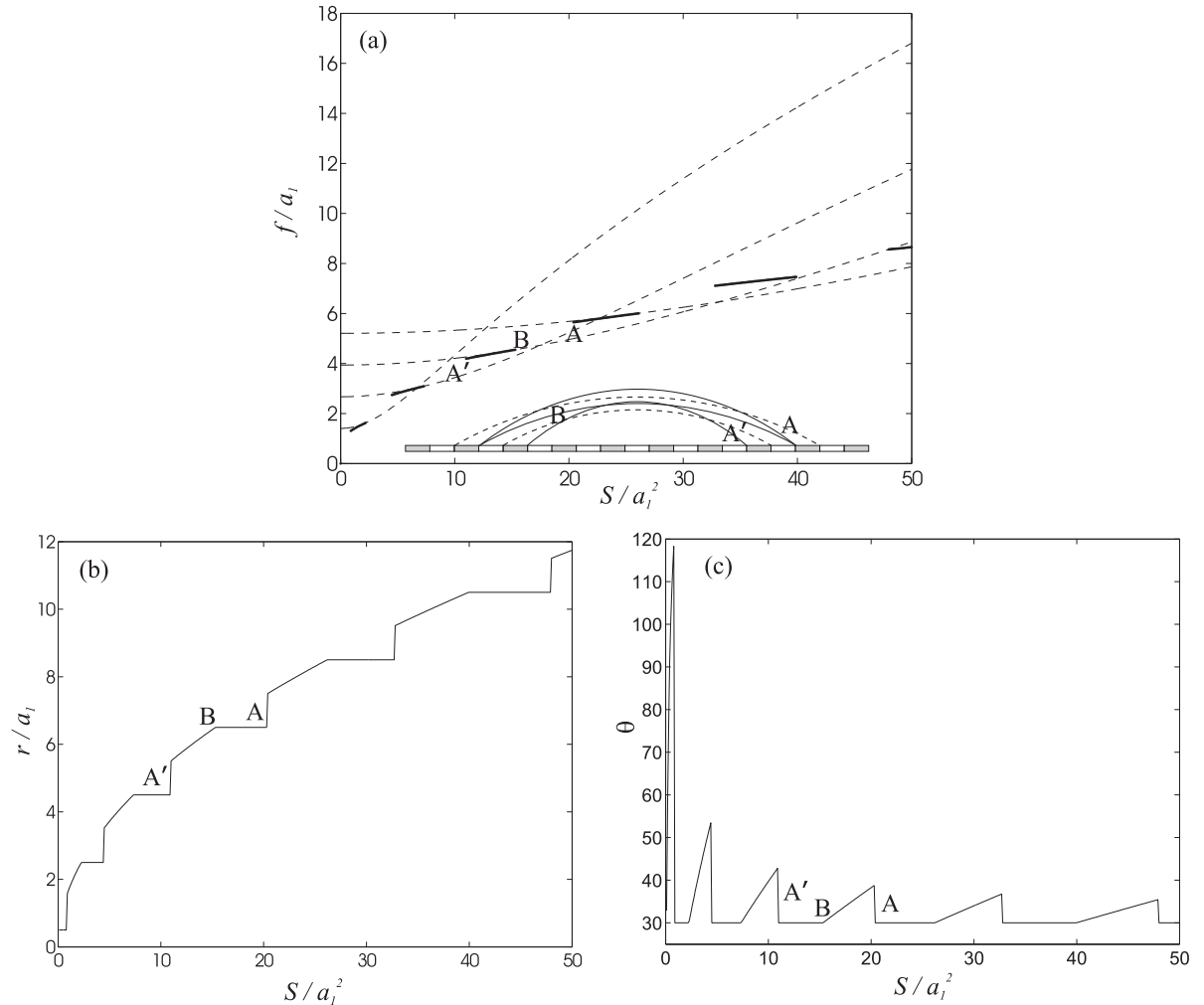


Figure 4.3: The dynamics of the receding contact line for $a_1/a_2 = 1$, $\theta_1 = 30^\circ$ and $\theta_2 = 60^\circ$. (a) Free energy, (b) drop radius, and (c) macroscopic contact angle as a function of drop size. A and A': the contact line immediately dewets the hydrophobic stripe. AB: the contact line is pinned until $\theta = \theta_1$. BA': the contact line recedes with $\theta = \theta_1$. The inset in (a) summarises the evolution of the drop shape. The solid lines in the inset show the drop profiles at A, B and A', while the dashed lines correspond to the drop profiles at A and A' immediately before contact line jumps occur.

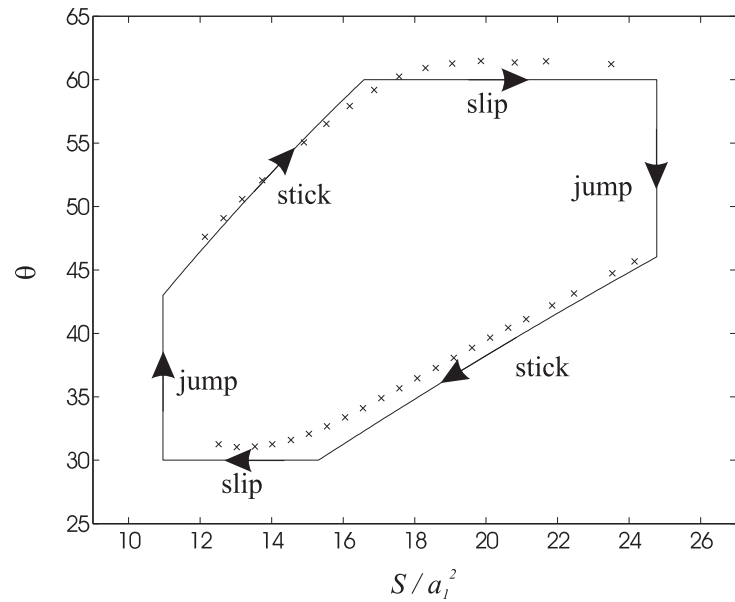


Figure 4.4: Hysteresis curve for a two dimensional, cylindrical drop on a chemically striped surface. $a_1 = a_2 = 30$, $\theta_1 = 30^\circ$ and $\theta_2 = 60^\circ$. The data points are results from the lattice Boltzmann simulations and the solid line corresponds to the analytical calculations.

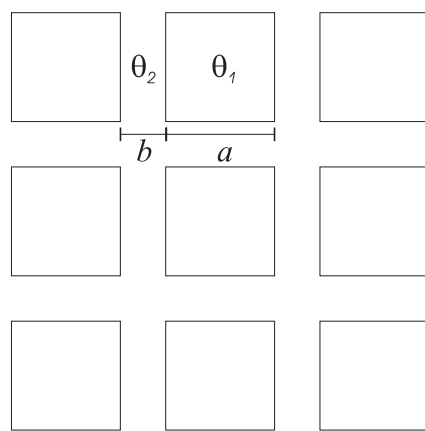


Figure 4.5: Schematic diagram of the chemically patterned surface.

of the channels between them is $\theta_2 = 60^\circ$. In the second case (surface B), we swapped the values of the equilibrium contact angles so that $\theta_1 = 60^\circ$ for the squares and $\theta_2 = 110^\circ$ for the channels. Due to the particular choice of a and b , the two surfaces have almost the same macroscopic contact angle, $\theta_{CB} \simeq 85.5^\circ$ calculated using the Cassie-Baxter formula

$$\cos \theta_{CB} = \Phi_1 \cos \theta_1 + \Phi_2 \cos \theta_2 \quad (4.10)$$

which averages over the surface contact angles. Φ_1 and Φ_2 are the fractions of the surface with intrinsic equilibrium contact angle θ_1 and θ_2 respectively. Therefore we might naively expect the two surfaces to have very similar behaviour. However, this is not the case unless the strength of the heterogeneities is below a certain threshold [95, 106], a condition which implies negligible contact angle hysteresis.

Consider first the advancing contact angle. From the discussions in section 4.1, we know that contact line pinning occurs because there is an energy barrier for the drop to move onto a hydrophobic area, whilst the contact line jumps when it reaches a new hydrophilic region. Therefore we expect to observe stick behaviour when the contact line reaches unwetted hydrophobic parts of the surface, slip when it moves across partially covered hydrophobic portions, and jumps as the contact line reaches the hydrophilic areas. This is indeed observed in the lattice Boltzmann simulations, as shown by the plots of the base radius of the drop at different volumes in Figs. 4.6(c) and 4.7(c) for surfaces A and B respectively.

Since the contact line is no longer circular the local contact angle varies along the contact line and the notion of a macroscopic contact angle pertaining to the whole drop is not well defined. However, a popular approach (e.g. [108]) is to match the drop profile far away from the substrate to a spherical cap to obtain the drop radius of curvature, and hence define a macroscopic contact angle

$$\cos \theta_{\text{macro}} = (1 - h/R), \quad (4.11)$$

where h is the drop height and R is the radius of curvature at the top of the spherical cap. If the length scales of the heterogeneities are of order the interface width then one expects Eq. (4.11) to give a value of θ_{macro} equal to the Cassie-Baxter contact angle. However, as we see in Figs. 4.6 – 4.7, this is not necessarily the case for the length scales considered here. Indeed, in some of the metastable states the drop shape is far from a spherical cap and therefore it makes little sense to define a macroscopic contact angle. As a guide to the accuracy of the definition

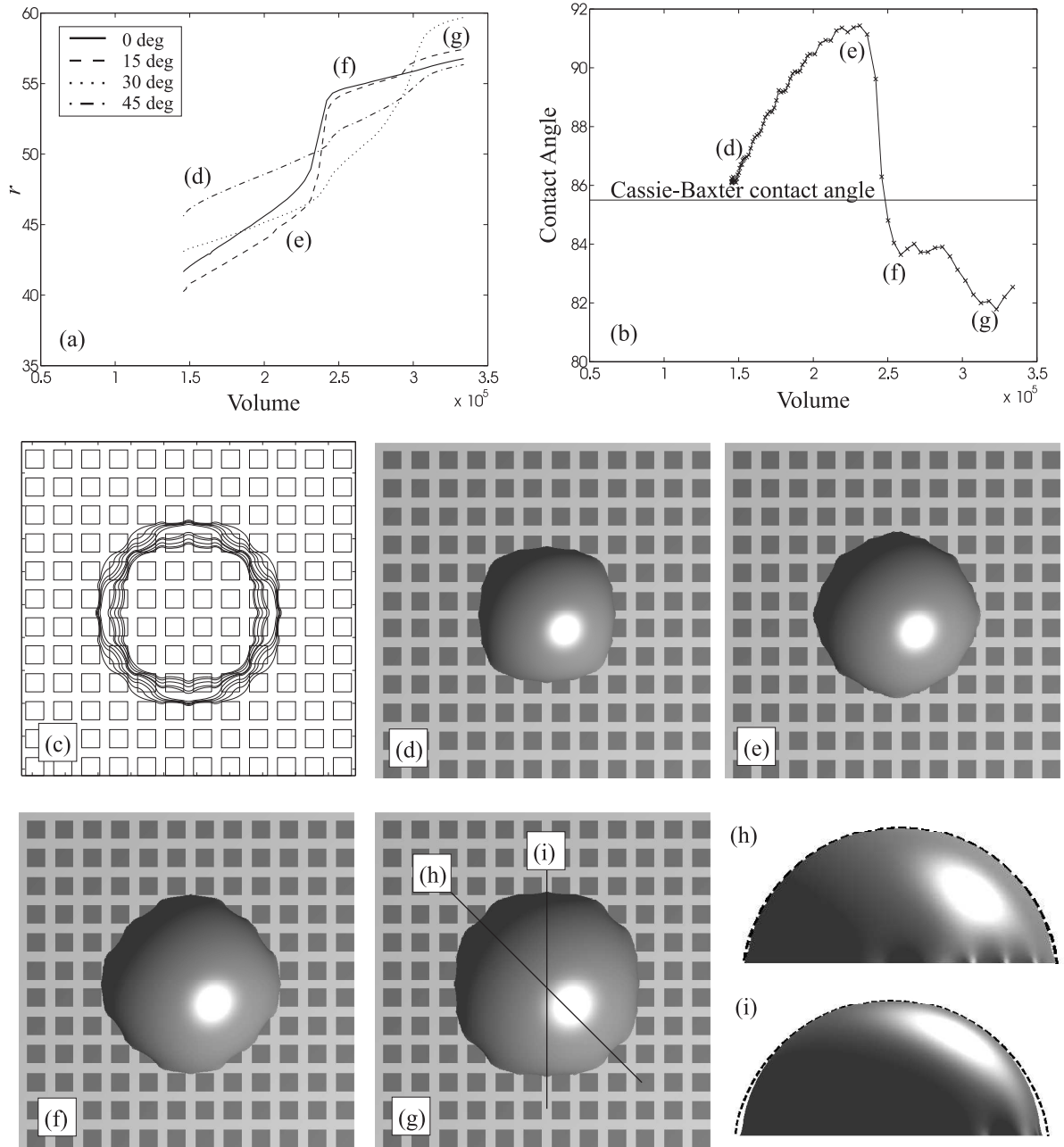


Figure 4.6: Advancing contact line dynamics for surface A, where squares with $\theta_e = 110^\circ$ and length $a = 12$ are separated by a distance $b = 5$, on a background with $\theta_e = 60^\circ$. (a) Volume dependence of the interface position at an angle 0° , 15° , 30° , and 45° with respect to the lattice axes. (b) Macroscopic contact angle as a function of drop volume. (c) Contour plots of the base radius at various drop volumes. (d-g) Top view of the drops at the points indicated in frame (b). (h-i) Side views of the drop as indicated in frame (g).

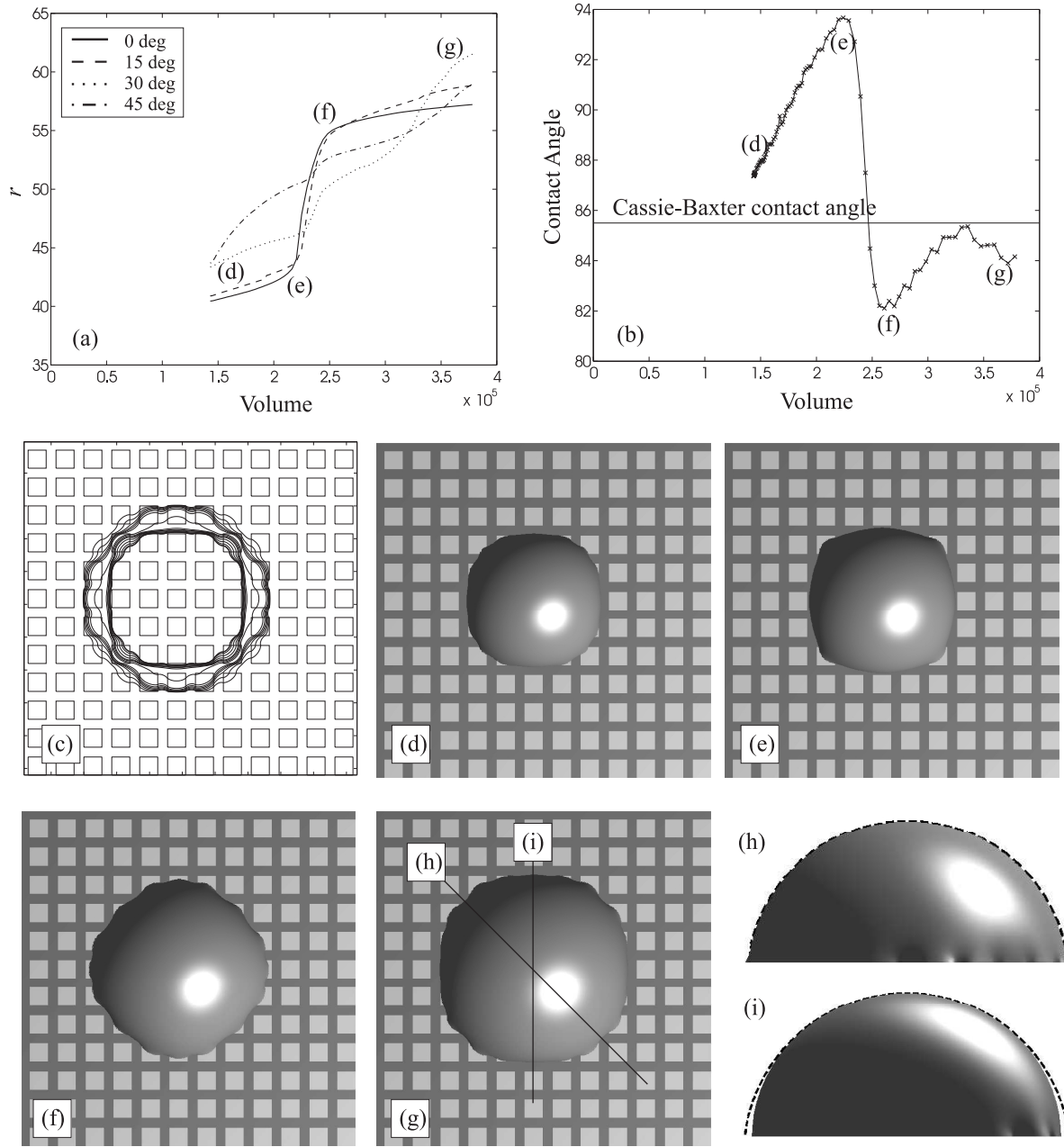


Figure 4.7: Advancing contact line dynamics for surface B, where squares with $\theta_e = 60^\circ$ and length $a = 12$ are separated by a distance $b = 5$, on a background with $\theta_e = 110^\circ$. (a) Volume dependence of the interface position at an angle 0° , 15° , 30° , and 45° with respect to the lattice axes. (b) Macroscopic contact angle as a function of drop volume. (c) Contour plots of the base radius at various drop volumes. (d-g) Top view of the drops at the points indicated in frame (b). (h-i) Side views of the drop as indicated in frame (g).

(4.11), Figs. 4.6 – 4.7 (h–i) show the side views of the largest (for advancing contact angle) or smallest (for receding contact angle) simulated drops at two different viewing angles, with the dashed lines showing the corresponding spherical fit. In general, the fit is better for the diagonal cross sections as compared to the vertical or horizontal cross sections. This is because along the diagonal direction it is very disadvantageous for the contact line to lie entirely in the hydrophilic region. As a result, contact line pinning is weaker, and the drop interface is more able to take a circular shape. The top view of the drops are shown in Figs. 4.6 – 4.7 (g).

With these cautions the macroscopic contact angle, defined by Eq. (4.11) is plotted as a function of drop volume in Figs. 4.6 – 4.7 (b). Fig. 4.6 gives the results for surface A and Fig. 4.7 for surface B. The overall behaviour of the curves is reminiscent of that for the two dimensional case in Fig. 4.2. However changes in slope are rounded and there is secondary structure that depends on the details of the surface patterning, and on the shape and position of the contact line. This is an important new feature of the three dimensional geometry; that the slip-stick-jump behaviour can occur at different volumes in different directions, leading to secondary structure in the base radius and contact angle plots. This underlines the importance of using multiple viewing angles when measuring the advancing and receding contact angles on patterned surfaces.

The behaviour of the different directions is, however, correlated. This can be seen in Figs. 4.6(a) and 4.7(a), where the variation of the interface position is plotted against volume at several angles with respect to the lattice axes. For example, any variation in the drop radius at 0° is typically accompanied by a similar variation at 15° , although the drop radius at 45° does not necessarily follow the same trend. Essentially this more complex motion of the drop in three dimensions occurs because the contact line lies on both hydrophobic and hydrophilic portions of the surface to avoid large surface distortions which would lead to a large liquid–gas surface free energy penalty. The shape of the contact line is thus very complicated and can be approximated analytically only in a few special cases [104, 105]. Nevertheless, as one would qualitatively expect, the simulation results show that the sections of contact line which lie on hydrophobic areas are concave whilst those on hydrophilic regions are convex.

We now compare the behaviour on surfaces A and B. Results for surface A are shown in Fig. 4.6. As its volume increases the drop wishes to move onto the hydrophilic channels between the hydrophobic patches, but prefers to also cover part of the hydrophobic regions to avoid significant interface distortion. As a result, the drop tends to be faceted. The

first, larger, jump in contact angle in Fig. 4.6(b) occurs when the contact line reaches the hydrophilic channels in the vertical and horizontal directions. The contact line moves more easily in the diagonal directions and the second, smaller, jump is due to the sudden movement of the contact line along the diagonal.

For the advancing motion, contact line pinning is more pronounced on surface B (see Fig. 4.7). There is a relatively high free energy barrier to move onto the hydrophobic channels and hence contact line jumps occur at higher contact angles. As a corollary of this the free energy release and the jump in contact angle upon depinning is also higher for surface B. From Figs. 4.6 and 4.7, the jumps can be read off as 8° and 11.5° for surfaces A and B respectively.

Similar results for the receding contact angles are presented in Figs. 4.8 and 4.9 for surfaces A and B respectively. Comparing the contour plots for the advancing and receding contact line, we find that contact line pinning occurs at very similar positions: for surface A, when the drop tries to dewet the hydrophilic channel, and for surface B, as it dewets the square hydrophilic patches. Since the free energy barrier is highest in the vertical or horizontal directions, the primary features of the curves are caused by contact line pinning in these directions. The secondary features are due to the contact line dynamics in the diagonal directions. Again, this is similar to the behaviour as the drop advances. It is important to realise, however, that this is only a qualitative similarity. The receding jumps occur at different volumes and have magnitudes 8.5° and 10.5° for surfaces A and B respectively. Figs. 4.6(b) and 4.8(b) also provide a clear example that the secondary structures can be different for the advancing and receding contact angles.

In two dimensions the advancing and receding contact angles were $\theta_e|_{\max}$ and $\theta_e|_{\min}$ (here 110° and 60°). In three dimensions, these values are reduced by the additional surface free energy penalty caused by distortions of the drop. On surfaces A and B, θ_A are 91.4° and 93.7° respectively, bounded by $\theta_e|_{\max}$ and the Cassie-Baxter contact angle θ_{CB} . The receding contact angles are 80.1° and 80.2° for surfaces A and B and are bounded by $\theta_e|_{\min}$ and θ_{CB} . We therefore find that contact angle hysteresis is slightly larger for surface B (13.5°) than for surface A (11.3°). We expect this discrepancy to become larger if the wettability contrast between the hydrophilic and hydrophobic patches is increased and future work will explore both this and the dependence of contact angle on patch size. The initial positioning of the drop with respect to the hydrophobic grid will change the quantitative details of the behaviour, but we expect the qualitative descriptions we have here to remain true.

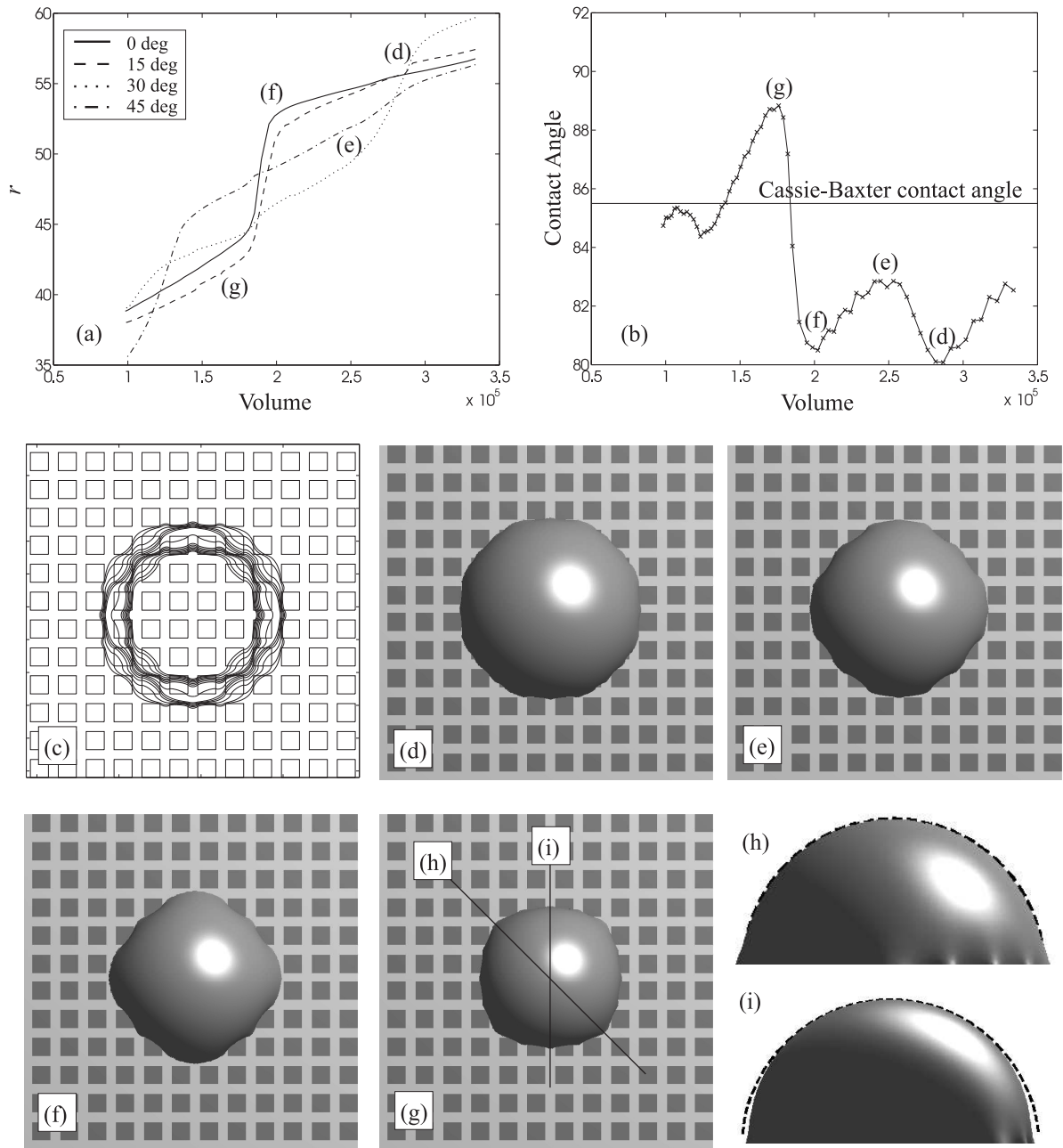


Figure 4.8: Receding contact line dynamics for surface A, where squares with $\theta_e = 110^\circ$ and length $a = 12$ are separated by a distance $b = 5$, on a background with $\theta_e = 60^\circ$. (a) Volume dependence of the interface position at an angle 0° , 15° , 30° , and 45° with respect to the lattice axes. (b) Macroscopic contact angle as a function of drop volume. (c) Contour plots of the base radius at various drop volumes. (d-g) Top view of the drops at the points indicated in frame (b). (h-i) Side views of the drop as indicated in frame (g).

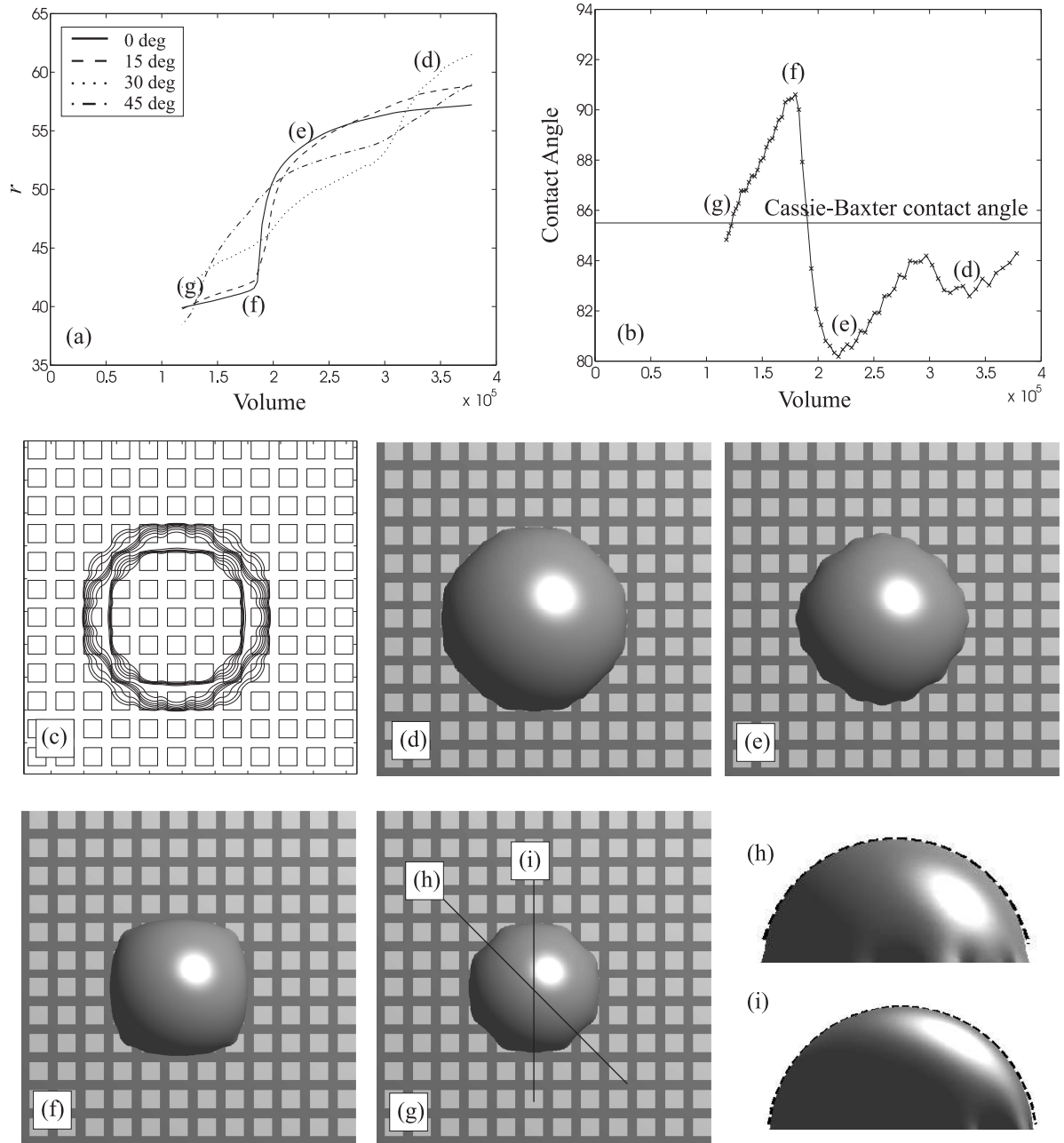


Figure 4.9: Receding contact line dynamics for surface B, where squares with $\theta_e = 60^\circ$ and length $a = 12$ are separated by a distance $b = 5$, on a background with $\theta_e = 110^\circ$. (a) Volume dependence of the interface position at an angle 0° , 15° , 30° , and 45° with respect to the lattice axes. (b) Macroscopic contact angle as a function of drop volume. (c) Contour plots of the base radius at various drop volumes. (d-g) Top view of the drops at the points indicated in frame (b). (h-i) Side views of the drop as indicated in frame (g).

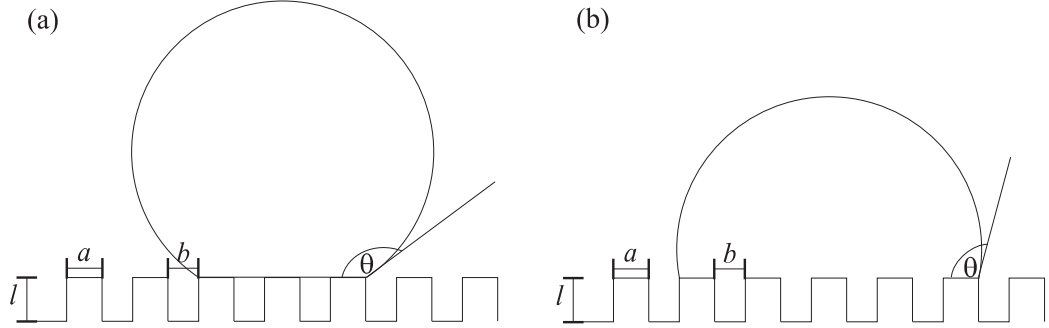


Figure 4.10: Schematic diagram of a cylindrical drop on a topologically patterned surface: (a) suspended state and (b) collapsed state.

4.3 Two Dimensional Suspended Drop on a Topologically Patterned Surface

We now consider unforced hysteresis on a topologically patterned surface that consists of an array of posts as shown in Fig. 4.10; this is a typical fabricated superhydrophobic surface. In this section, we concentrate on a two dimensional suspended drop, showing that the advancing and receding contact angles are 180° and θ_e respectively [102]. We then, in section 4.4, treat the two-dimensional collapsed drop. Here the hysteresis is larger with θ_A and θ_R equal to 180° and $\theta_e - 90^\circ$. The extension to three dimensions will be discussed in section 4.5 and 4.6 for the suspended and collapsed drops respectively.

As the drop retains the shape of a circular cap above the posts, the free energy calculations described in section 4.1 can be adapted to explore the way in which the contact line moves as the volume of the drop is slowly increased or decreased. The argument is analogous to that for the chemically striped surface if we take θ_1 to be the equilibrium contact angle of the posts and θ_2 to be the liquid–gas interface contact angle, which is equal to 180° . Hence we expect the advancing and receding contact angles to be $\theta_A = \theta_e|_{\max} = 180^\circ$ and $\theta_R = \theta_e|_{\min} = \theta_e|_{\text{post}}$ respectively. For a finite value of base radius r , the contact angle will reach 180° only as $R \rightarrow \infty$. As a result, the contact line will remain pinned indefinitely at the outer edge of a given post as the drop volume is increased.

These predictions are consistent with lattice Boltzmann simulations as shown in Fig. 4.11(a). In this set of simulations, we used a post width $a = 7$, post separation $b = 13$, and an equilibrium contact angle $\theta_e = 120^\circ$. The drop volume was increased by about a factor 4, and the contact angle to 162° , and no transition was observed. At this point it was no longer

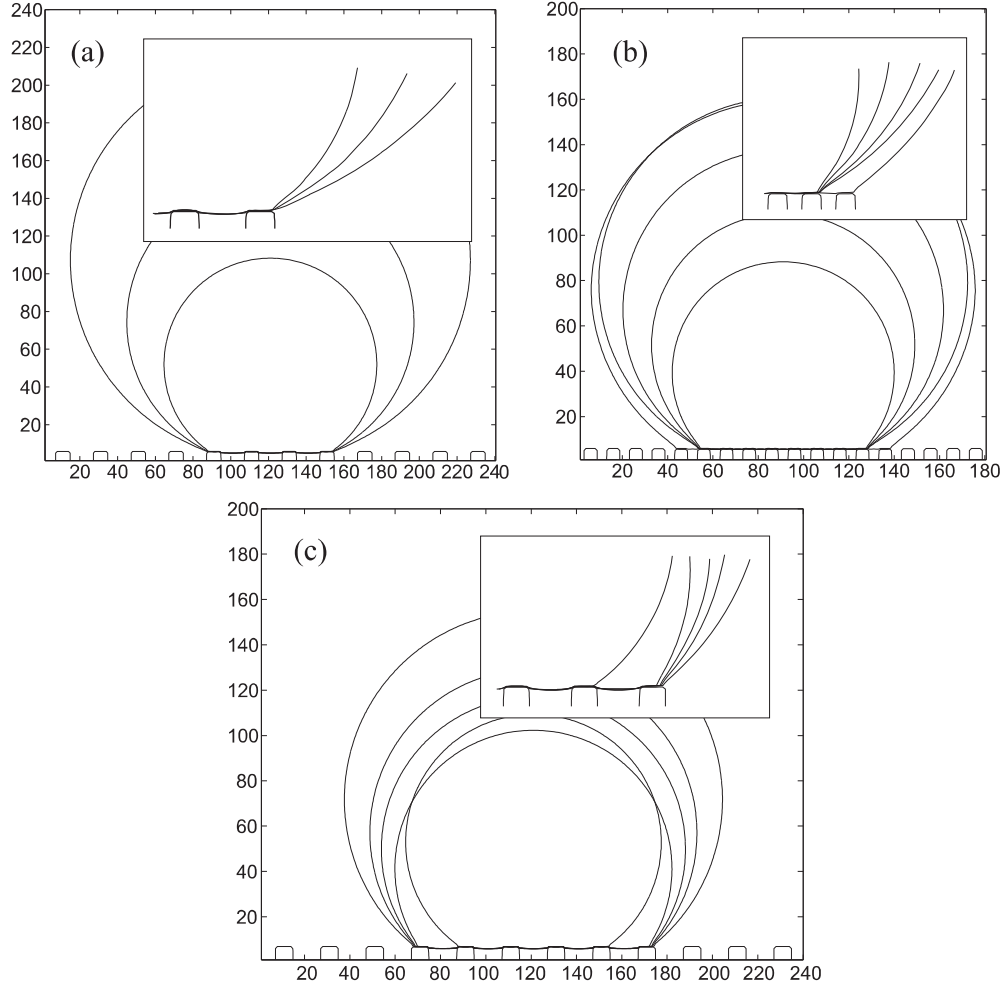


Figure 4.11: Drop shape as a function of time from lattice Boltzmann simulations of a cylindrical drop suspended on a topologically patterned surface. (a) The advancing contact line remains pinned during the simulation ($a = 7$ and $b = 13$). (b) A contact line jump occurs when $\theta = 155^\circ$ ($a = 5$ and $b = 5$). (c) The measured receding contact angle $\sim 120^\circ$ ($a = 7$ and $b = 13$). The position of the contact lines can be seen more clearly in the insets.

possible to run the simulation as the drop filled the simulation box. As the drop volume was decreased (Fig. 4.11(c)) the drop jumped between posts at $\theta \sim 120^\circ$. We do not find that the receding drop establishes its equilibrium contact angle on the side of the asperities as proposed by Extrand [93].

If the separation between the posts was decreased to $b = 5$ (with $a = 5$), however, we did observe a contact line jump from one post to another as shown in Fig. 4.11(b). The contact angle of the drop just before the jump was 155° . This is due to the diffuse liquid–gas interface in the lattice Boltzmann simulations which allows the interface to probe the existence of the neighbouring post and hence lower its free energy by jumping across to it. To check this interpretation we ran a simulation increasing κ from 0.004 to 0.006 corresponding to a wider

interface. This led to a decrease in the advancing contact angle θ_A from 155° to 152° .

In the model, the interface width is comparable to the dimensions of the posts, a problem inherent in mesoscale simulations of multiphase fluids. This is not true for typical superhydrophobic surfaces where the posts are $\sim \mu\text{m}$ in size. Nevertheless, in real systems, there are likely to be mechanical vibrations [110], surface imperfections, and thermal fluctuations [109], which will cause the contact line to feel the neighbouring posts. Gravity will also lower the liquid–gas interface and hence makes it easier to touch the neighbouring posts.

4.4 Two Dimensional Collapsed Drop on a Topologically Patterned Surface

We now discuss unforced hysteresis for a cylindrical collapsed drop where the gaps between the posts are filled with liquid. When the drop volume is increased the advancing contact angle is 180° and the drop behaves in the same way as for the suspended state. This is because locally, in the vicinity of the contact line, the drop has no information as to whether it is in the collapsed or suspended state. Indeed, in the two dimensional simulations we have run, if the contact line does advance, the grooves are not filled by the liquid drop as the contact line advances from one post to the next, in contradiction to the work of Li *et al.* [103], which assumes that the gap is filled as the contact line advances. The results are shown in Fig. 4.12(a) for $a = 5$, $b = 5$, $l = 5$, and $\theta_e = 120^\circ$, the same parameters as in Fig. 4.11(b). In a perfect system there should be no advancing jump between posts. We see a transition at $\theta = 154^\circ$ for the collapsed drop because of the diffuseness of the interface. This is consistent with the results in Fig. 4.11(b) where a contact line jump was seen at $\theta = 155^\circ$ for the suspended drop.

Next we consider the way in which the contact line recedes as the drop volume decreases. The typical behaviour is shown in Fig. 4.12(b). As for the suspended drop, the contact line is pinned at the outer edge of a post until $\theta = \theta_e$. It then retreats smoothly across the post. However, unlike the suspended case, the contact line is pinned again at the inner edge of the posts. This happens because the free energy gain from the reduced liquid–gas interface of the circular cap is not large enough to dewet the side walls of the posts.

To demonstrate this we recall that drop free energy has two important contributions. The first comes from the liquid–gas interface of the circular cap, while the second is from the

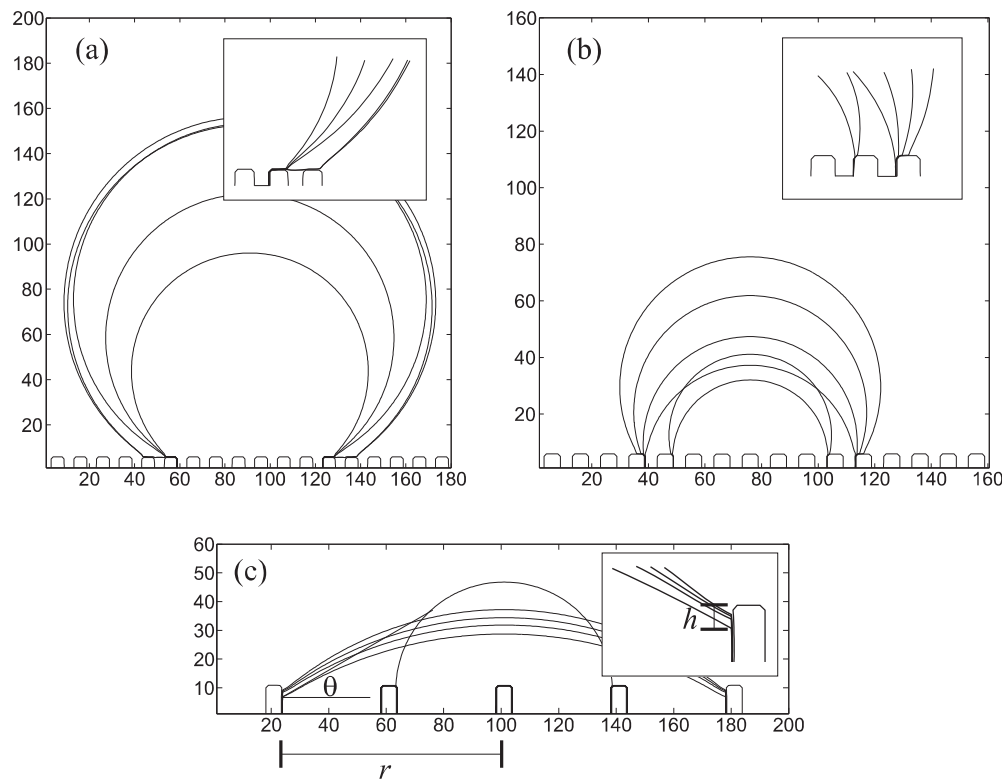


Figure 4.12: Drop shape as a function of time from lattice Boltzmann simulations of a cylindrical drop collapsed on a topologically patterned surface showing the contact line motion as the drop volume is (a) increased or (b-c) decreased. (a) and (b): $a = 5$, $b = 5$ and $l = 5$. (c): $a = 5$, $b = 35$, and $l = 10$. The equilibrium contact angle $\theta_e = 120^\circ$. The position of the contact lines can be seen more clearly in the insets.

liquid–solid boundary.

$$f \equiv F/\sigma_{LG} = \frac{2r\theta}{\sin\theta} + 2h \cos\theta_e, \quad (4.12)$$

where r , θ , and h are respectively the base radius, the macroscopic contact angle, and the distance from the inner edge of the posts to the contact line. These are illustrated in Fig. 4.12(c). Taking the first derivative of f gives

$$df = \left[\frac{2r}{\sin\theta} - \frac{2r\theta \cos\theta}{\sin^2\theta} \right] d\theta + 2 \cos\theta_e dh. \quad (4.13)$$

For a drop of a constant volume

$$S = r^2 \frac{\theta - \sin\theta \cos\theta}{\sin^2\theta} - 2rh,$$

and hence dh to $d\theta$ are related by

$$dh = -r \frac{\theta \cos\theta - \sin\theta}{\sin^3\theta} d\theta. \quad (4.14)$$

Subsituting Eq. (4.14) into Eq. (4.13) gives

$$df = 2(\sin\theta + \cos\theta_e)dh. \quad (4.15)$$

The condition $df/dh > 0$ implies that pinning will hold at the top of the posts as long as $\theta > \theta_e - 90^\circ$. This is best seen in Fig. 4.12(c) where the posts' separation has been increased to $b = 35$ to facilitate the measurement of the receding contact angle. The drop is found to recede at 32° , consistent with the expected analytical result $\theta_e - 90^\circ = 30^\circ$. We note that this is equivalent to the criteria first proposed by Gibbs [111] and confirmed experimentally by Oliver *et al.* [102].

Once this condition is satisfied, further reduction in the drop volume will cause the drop to steadily dewet the side of the post. If the posts are short, the contact line will touch the base of the interstices and it will quickly retract to the neighbouring posts. If the posts are tall, however, the liquid–gas interface can intersect the corners of the neighbouring post, in which case satellite drops will be formed in between the posts. In either case, the contact line will typically reach the next post and move to its inner edge without regaining a contact angle θ_e . Therefore the behaviour will typically be stick-jump rather than stick-jump-slip. Furthermore,

comparing this motion to that described for the suspended drop in section 4.3 shows that, in this simple two dimensional model, the contact angle hysteresis is 90° larger for the collapsed state than for the suspended state.

4.5 Three Dimensional Suspended Drop on a Topologically Patterned Surface

The two dimensional model discussed in section 4.3 and 4.4 captured the phenomenon of contact line pinning on topologically patterned surfaces but the three phase contact line was only represented by two points at the ends of the liquid–gas interface. Hence we were unable to address the effect of distortions of the contact line caused by the surface roughness. Therefore we now present results from three dimensional lattice Boltzmann simulations aimed at investigating contact angle hysteresis on three dimensional topologically patterned surfaces.

For the suspended state we used $a = 3$, $b = 7$, $l = 5$, and $\theta_e = 110^\circ$ which, using the Cassie-Baxter formula (1.4), gives an estimate of $\theta = 160^\circ$ for the macroscopic contact angle. The very high value of the drop contact angle is challenging for the simulations because a small change in the contact angle requires a large change in the drop volume. Moreover, since one needs the drop to be suspended on a reasonable number of posts, a huge simulation box is needed. We used $168 \times 168 \times 168$ lattice points and the largest drop simulated had a volume of 16.8×10^5 .

Small deviations in the drop shape near the surface (from a spherical cap) can cause large uncertainties in the contact angle measurements. The definition in Eq. (4.11) gives $\theta = 180^\circ$ for the drops modelled in this section. We therefore use

$$\theta_{\text{macro}} = 2 \tan^{-1} \left(\frac{H}{r_{\text{max}}} \right), \quad (4.16)$$

where H is the height of the drop and r_{max} is the maximum base radius, as an alternative definition of macroscopic contact angle.

Fig. 4.13 (a) shows the drop contact angle as a function of volume. In the simulation, we have quasi-statically increased the volume from 6.8×10^5 to 16.8×10^5 . This gives a macroscopic contact angle θ (Eq. (4.16)) which ranges from 161.8° to 166.6° . At least for the range of volumes simulated the contact line remains pinned as suggested by other groups [89–91, 94, 108]

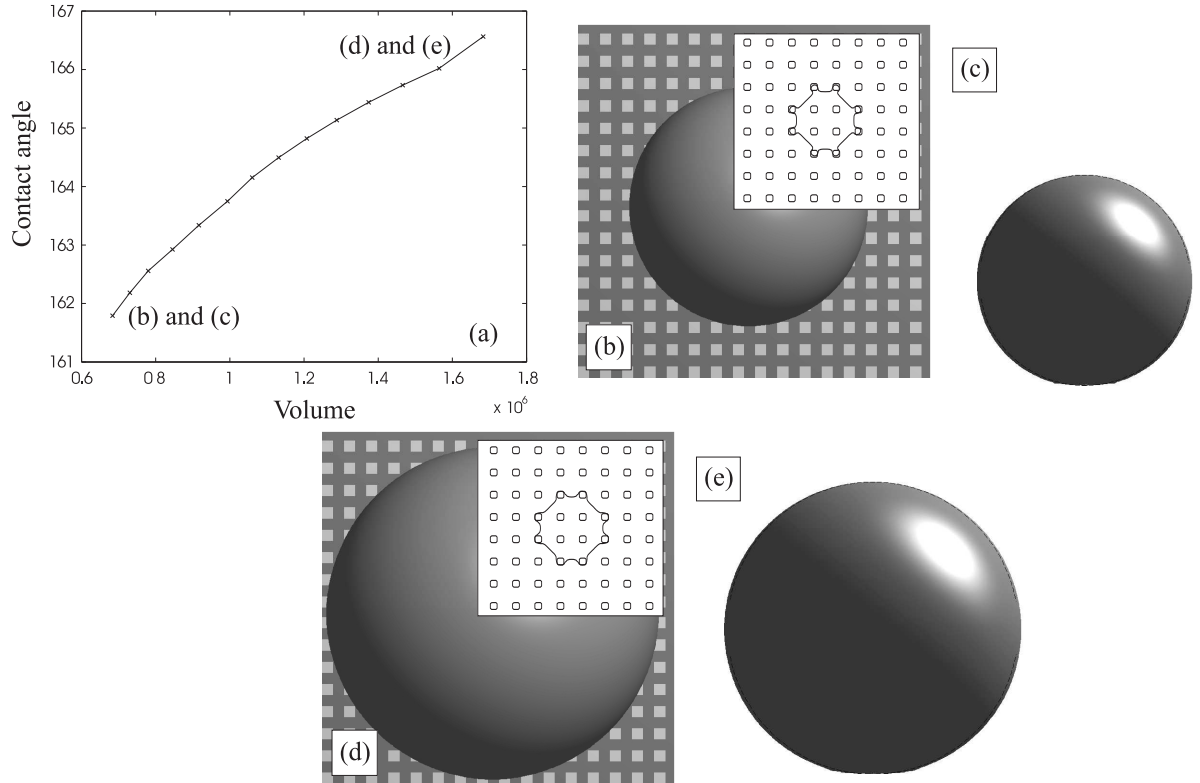


Figure 4.13: Advancing contact line dynamics for a suspended drop on a superhydrophobic surface with $a = 3$, $b = 7$, $l = 5$, and $\theta_e = 110^\circ$. (a) Contact angle as a function of volume. (b) and (c) Top and side view of the drop at $V = 6.8 \times 10^5$. (d) and (e) Top and side view of the drop at $V = 16.8 \times 10^5$. The insets in frame (b) and (d) are the corresponding contour plots of the base of the drop.

and consistent with our two dimensional arguments that the contact line jump occurs when $\theta \rightarrow 180^\circ$ or when the interface is able to touch the neighbouring posts. In Fig. 4.13(b–e) the contour plot, top view, and side view of the drop at the beginning and at the end of the simulation are shown.

While the contact line is very difficult to advance, it is a lot easier to recede. We reduce the drop volume by reducing the liquid density by around 0.1% and then let the system to relax to a (local) minimum energy state. For the parameters used here, the receding contact line jump occurs at 166.5° ($V = 15.4 \times 10^5$), as shown in Fig. 4.14(a). This high value of the receding angle implies that the receding contact line is very unstable against small perturbations, highlighting the weak adhesion of suspended drops on superhydrophobic surfaces. Indeed even the small volume changes we used in the simulations tended to make the drop detach slightly from the surface. The receding contact line can be made even less stable by reducing the solid fraction or by increasing the hydrophobicity of the posts [89, 90].

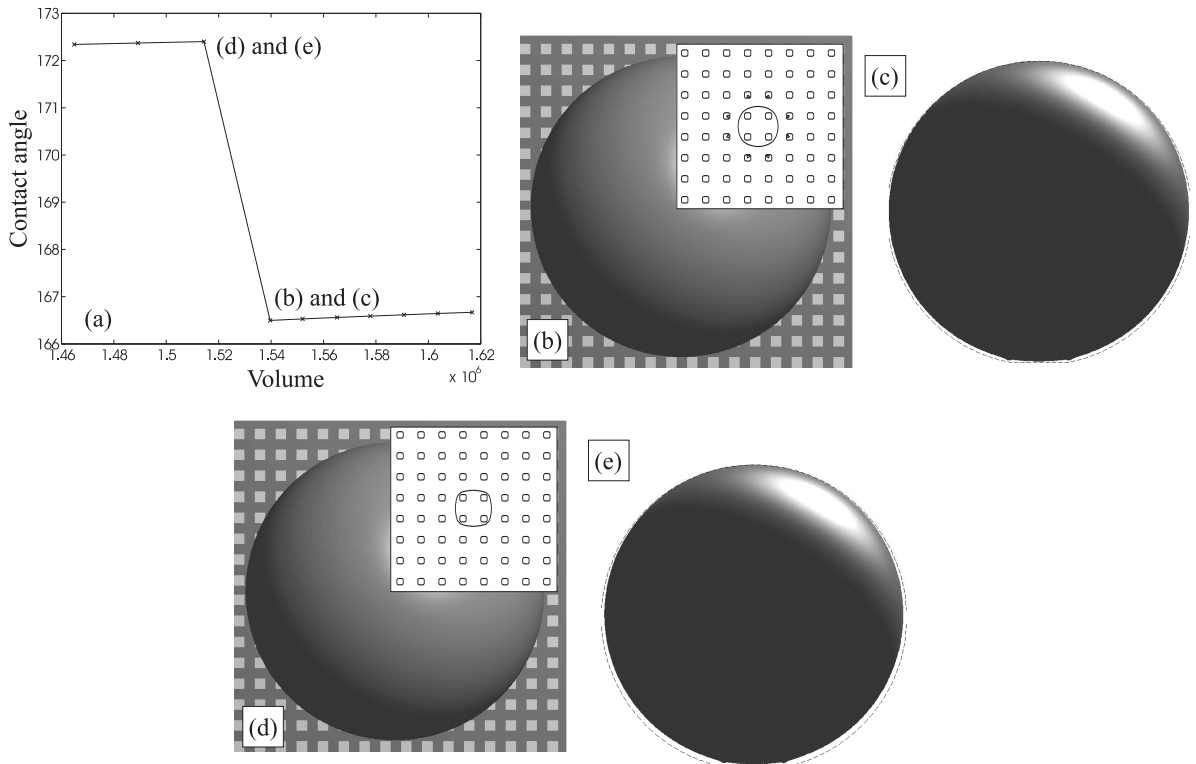


Figure 4.14: Receding contact line dynamics for a suspended drop on a superhydrophobic surface with $a = 3$, $b = 7$, $l = 5$, and $\theta_e = 110^\circ$. (a) Contact angle as a function of volume. (b) and (c) Top and side view of the drop at $V = 15.4 \times 10^5$. (d) and (e) Top and side view of the drop at $V = 15.1 \times 10^5$. The insets in frame (b) and (d) are the corresponding contour plots of the base of the drop.

The contour plot, top view, and side view of the drop before and after the contact line jump are shown in Fig. 4.14(b–e).

4.6 Three Dimensional Collapsed Drop on a Topologically Patterned Surface

We now turn our attention to the collapsed state where the space between the posts is filled with liquid. We use $a = 4$, $b = 6$, $l = 5$, and $\theta_e = 120^\circ$, which according to the Wenzel formula (1.5) gives a contact angle $\theta_W = 154^\circ$.

Fig. 4.15(a) shows the macroscopic contact angle of the drop, calculated using the definition (4.11), as a function of increasing volume. Initially the contact angle increases because, even though the contact line moves outwards in the diagonal direction (with respect to the posts), it remains pinned in the horizontal and vertical directions. This can be seen in the contour plots shown in Fig. 4.15(b–c). Once the drop has touched the four neighbouring posts along

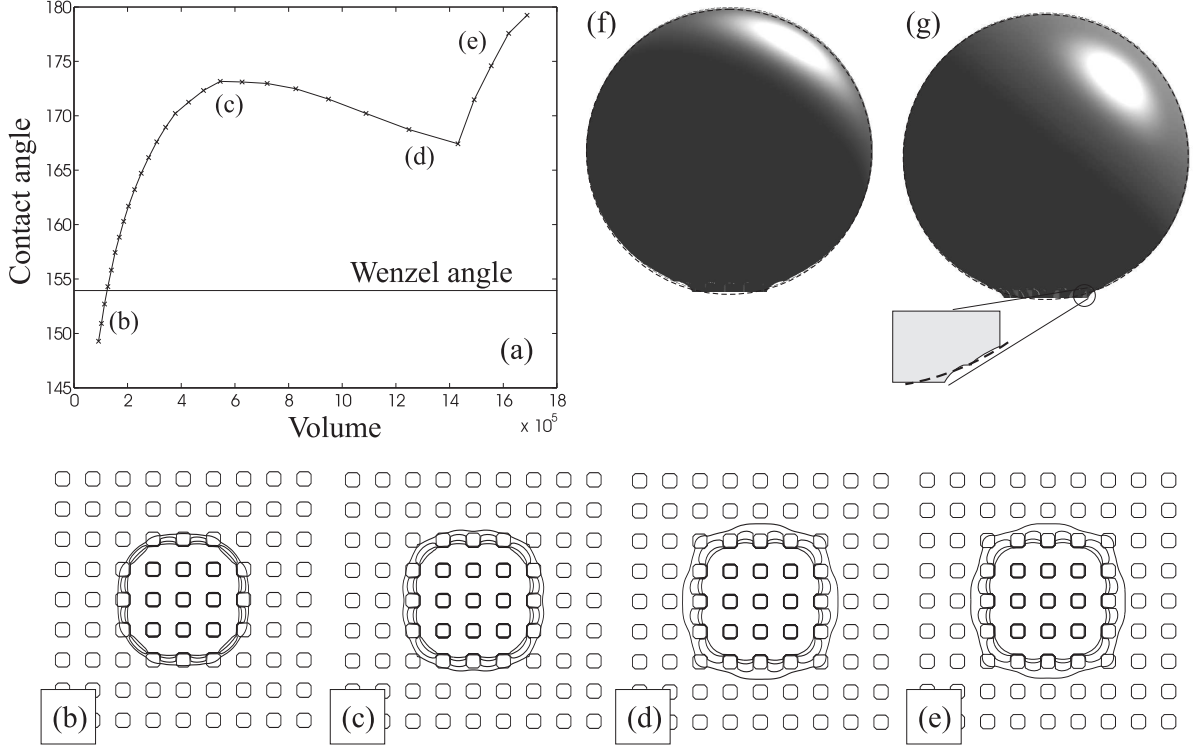


Figure 4.15: Advancing contact line dynamics for a collapsed drop on a superhydrophobic surface with $a = 4$, $b = 6$, $l = 5$, and $\theta_e = 120^\circ$. (a) Contact angle as a function of volume. (b–e) Contour plots of the drop at positions indicated in (a): the different lines correspond to heights 1, 3, 5, and 6 lattice spacings away from the bottom surface. (f) The drop cross section in the horizontal direction. (g) The drop cross section in the diagonal direction. The spherical fit is shown by the dashed lines and the inset magnifies the spherical fit close to the posts.

the diagonals, it wets the top of these posts (Fig. 4.15(d–e)) and this allows the contact angle to decrease slightly, by about 5° . At this stage the contact line will again be pinned until it is energetically favourable to jump and wet the neighbouring posts in the vertical and horizontal directions. This will become possible when the drop can feel the neighbouring posts. We note that this contact line jump has not occurred in the simulations we have presented here. Increasing the size of the simulation box was prohibitively expensive in computer time

Typical side views of the drops are shown in Fig. 4.15(f–g), with the dashed line showing the corresponding spherical fits. The fitted curves match well with drop profiles above the posts, but not with the profiles in between the posts. This again emphasises that any definition of macroscopic contact angle is arbitrary and should be treated with caution. In this section, the contact angle is calculated at the intersection between the fitted curve and the base surface. If instead we take the intersection between the fitted curve and the top of the posts, the values of the contact angles would be lower. This will however, not change the trends we describe in

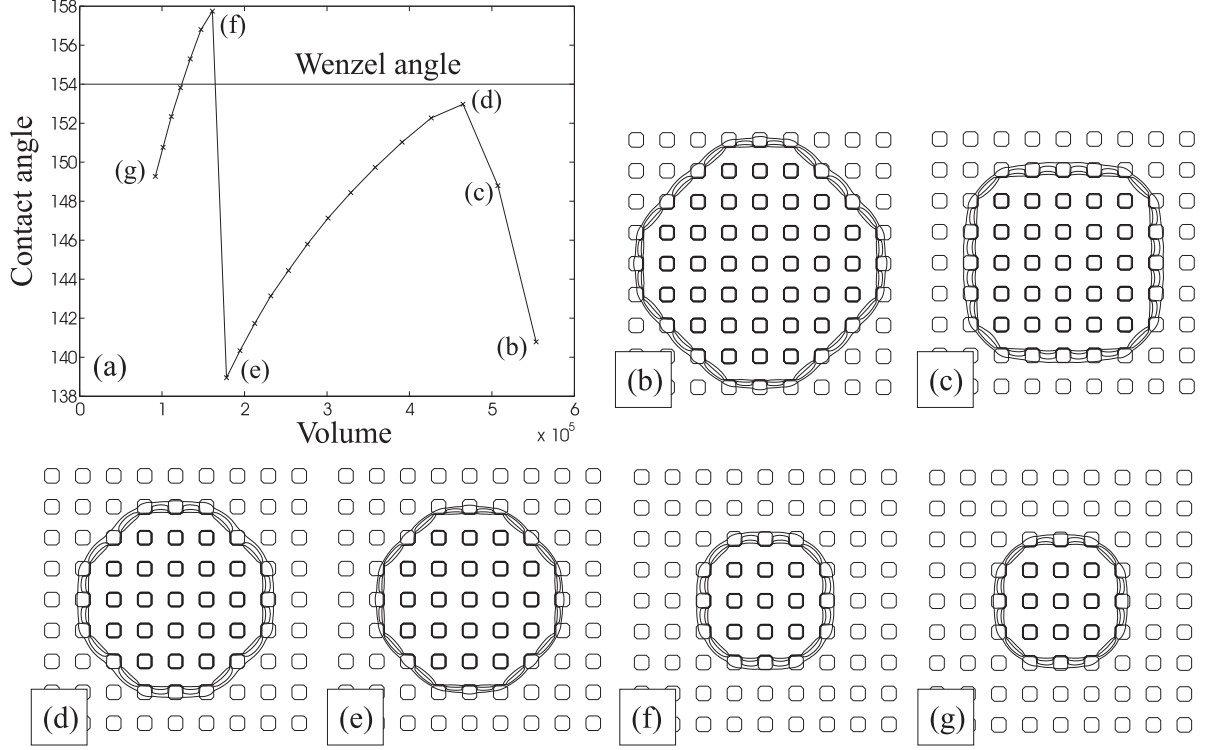


Figure 4.16: Receding contact line dynamics for a collapsed drop on a superhydrophobic surface with $a = 4$, $b = 6$, $l = 5$, and $\theta_e = 120^\circ$. (a) Contact angle as a function of volume. (b–e) Contour plots of the drop at positions indicated in (a): the different lines correspond to heights 1, 3, 5, and 6 lattice spacings away from the bottom surface.

this section.

In section 4.4, we found that, in two dimensions, the receding contact angle for the collapsed state is $\theta_e - 90^\circ$ because of the adhesion provided by the sides of the posts. In three dimensions, we expect the adhesion effect to remain relevant. However, the corresponding energy barrier will now be lowered by the free energy costs due to the liquid–gas interfaces between the posts.

The drop’s macroscopic contact angle as a function of decreasing volume is shown in Fig. 4.16(a). The general features of the curve are very similar to the other examples of receding contact line dynamics that we have discussed. The contact angle decreases slowly as volume is reduced (Fig. 4.16(d–e) and Figs. 4.16(f–g)) until any further reduction in drop volume makes it more favourable for the drop to depin its contact line (Figs. 4.16(b–d) and 4.16(e–f)). Naturally, as a result of the contact line jump, the contact angle increases very sharply. Taking the lowest (highest) value of the contact angle in Fig. 4.16(a) (Fig. 4.15(a)) as the receding (advancing) contact angle, we obtain $\theta_R = 139^\circ$, $\theta_A = 179^\circ$ and $\Delta\theta \sim 40^\circ$.

4.7 Discussion

In this chapter we described contact angle hysteresis on both chemically patterned and superhydrophobic surfaces as the drop volume was quasi-statically increased or decreased. We first considered the two dimensional case of a cylindrical drop. This is a useful baseline calculation as the models are tractable analytically and contain many features that carry over to three dimensions. It was also useful to check the results of lattice Boltzmann simulations against the two dimensional results. The simulation approach was then used to explore the full, three dimensional problem.

For chemically patterned surfaces in two dimensions the advancing (receding) contact angle is equal to the maximum (minimum) value of the equilibrium contact angle. In three dimensions these parameters act as bounds on the hysteresis. Extra free energy contributions, which result from the distortion of the surface, decrease the advancing, and increase the receding, contact angles, thus decreasing the contact angle hysteresis.

For superhydrophobic surfaces in two dimensions the advancing contact angle is close to 180° for both suspended and collapsed drops. The drop will only advance when it is able to feel the neighbouring posts because of, for example, finite interface width or mechanical vibration. This remains true in three dimensions, except for those cases in the collapsed state where the surface roughness factor is close to 1 and the equilibrium contact angle of the posts is close to 90° . In such cases, the drop is able to penetrate the corridors between the posts and the contact line can advance before the contact angle reaches 180° .

The receding contact angle is, however, very different for the suspended and collapsed states. In two dimensions, for suspended drops, it is equal to the contact angle of the posts θ_e . For the collapsed state it is equal to $\theta_e - 90^\circ$ because the interface needs to move down the sides of the posts to recede. In three dimensions these angles again provide limiting values.

For a suspended drop, to obtain a low contact angle hysteresis, the receding angle needs to be driven as close to 180° as possible [89, 90]. This can be done by making θ_e as large as is feasible and then choosing the surface patterning to distort the drop so that the free energy barriers are lowered. For the collapsed state, contact line pinning is stronger and hence we expect the receding contact angle to be lower and the contact angle hysteresis to be larger. This is observed experimentally (e.g. [7, 24, 89]) and is related to the very different adhesive properties of the suspended and collapsed states. To increase the receding contact angle, one

can increase θ_e , increase the posts' separation, or decrease the posts' size.

It is important to note that, because of the distorted drop shape, the advancing and receding contact angles depend on the direction in which the measurement is taken; indeed the concept of macroscopic contact angle is a matter of definition. They also depend sensitively on the details of the surface patterning and any average over the area of the patterning or over the angle along the contact line is not sufficient to predict the hysteretic properties of a surface. We also note that when the contact line jump involves more than one post (or chemical patch), it does not wet/dewet the posts simultaneously. For the advancing drop, movement starts at the centre post, while for the receding drop, the contact line first dewets the outer posts. This is in agreement with [94, 95, 104, 105]. Finally, we note that our three dimensional simulations may suffer from finite size effects. The simulated drops occupy a small number of posts/patches in comparison to the experiments. Nonetheless, we expect the qualitative results we obtain in this chapter to hold for larger drops.

It will be of interest to compare the results we have presented here for unforced hysteresis, where the drop volume is changed quasi-statically, to what we will term forced hysteresis, where the drop is pushed by, for example, a body force. The aim is to slowly increase the force and discuss the value of the advancing and receding contact angles at which the drop first starts to move. Because we are working in the limit of zero velocity free energy arguments can still be used.

On a flat, perfectly smooth surface the limiting force is zero and the drop will start to move as soon as it is pushed. On a patterned surface there will be pinning. The problem is, however, now much more complicated than for unforced hysteresis as the free energy barriers, of which there might be many, depend not only on the local surface patterning, but also on the overall shape of the drop. This in turn will depend on the size of the drop and the magnitude and details of the applied force. Therefore we expect that, in general, the stick-slip-jump behaviour is still observed, both in two and three dimensions, but the advancing and receding contact angles will differ from those of unforced hysteresis and that they will depend sensitively on the details of the problem. In general the depinning of the front and back contact line occur at different times, as opposed to the simultaneous depinning seen in the unforced case.

A further detail that we would like to note here is that, for the forced, three dimensional, suspended drop on a superhydrophobic surface, we observed another depinning mechanism for the advancing contact line. In section 4.3 and 4.5, we found that an equilibrium drop will

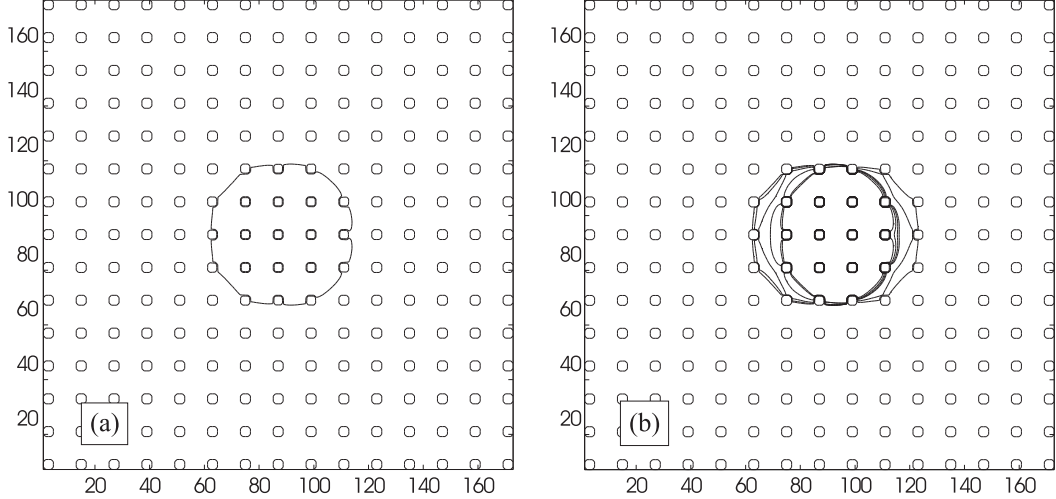


Figure 4.17: Forced hysteresis simulations of a spherical drop suspended on a topologically patterned surface. Contour plots of the drop just below the top of the posts when the drop is (a) pinned and (b) moving. The body force is $a = 10^{-9}$ for panel (a) and $a = 3 \times 10^{-9}$ for panel (b). The various lines in panel (b) correspond to the drop profiles at various times in the simulations. We have used the following parameters: $\theta_e = 95^\circ$, post width = 4, post separation = 8 and post height = 15.

only advance when it is able to feel the neighbouring posts because of, for example, finite interface width or mechanical vibration. When the drop is pushed by a body force, however, the drop can depin in the lateral direction. This is shown in Fig. 4.17. For a very small body force (Fig. 4.17(a)), the drop is pinned and the advancing contact line bulges in between two neighbouring posts. As the body force is further increased (Fig. 4.17(b)), this deformation becomes more significant, and at a critical force, the contact line depins. When this occurs the contact line is free to move to the next posts and hence the drop can move across the surface. This further implies that, for forced hysteresis, the advancing contact angle is less than 180° and the advancing contact line is more mobile than that predicted from the unforced hysteresis analysis. In the example shown in Fig. 4.17, the measured advancing angle is 160° .

CHAPTER 5

The Collapse Transition on Superhydrophobic Surfaces

“Has the drop collapsed yet?” - Julia Yeomans

“No, not yet!” - Halim Kusumaatmaja

As we have described in the Introduction, the hydrophobicity of a surface is amplified by its roughness [7, 12, 24]. This can happen in two different ways. When the liquid drop occupies the spaces between the surface projections, and is everywhere in contact with the surface, the drop is in the collapsed or Wenzel state [15] with contact angle

$$\cos \theta_W = r \cos \theta_e . \quad (5.1)$$

r is the ratio between the real surface area and its projection onto the horizontal plane and θ_e is the equilibrium contact angle of the flat surface. On the other hand, if penetration does not occur and the drop remains balanced on the surface projections with air beneath it, it is in the suspended or Cassie-Baxter state [11] with contact angle

$$\cos \theta_{CB} = \Phi \cos \theta_e - (1 - \Phi) , \quad (5.2)$$

where Φ the solid fraction of the surface on top of the corrugations.

For a given drop volume, the drop free energy increases with contact angle. This statement implies that the Cassie-Baxter state has the lowest energy when $\theta_{CB} < \theta_W$, and similarly the Wenzel state is the ground state when $\theta_W < \theta_{CB}$. However, in most cases, both states are (local) minima of the free energy and there is a finite energy barrier opposing the transition

between them. The magnitude of the energy barrier has been shown to depend on both the size of the drop and the roughness of the surface [22, 23].

The aim of this chapter is to explore mechanisms by which transitions between Cassie-Baxter and Wenzel states may occur. This is an important question because, even though both states show high values of the contact angle, many of their other physical properties, for example, contact angle hysteresis are very different. In particular, we consider the mechanisms by which a drop can spontaneously collapses from the Cassie-Baxter to Wenzel state as it evaporates [112, 113]. Here we focus on the limit where the evaporation timescale is much longer than the timescale for drop equilibration so that the drop is always in thermodynamic equilibrium. This is normally the physically relevant situation for experiments on micron-scale drops.

We first consider a drop on a two dimensional, superhydrophobic surface and present analytic results in section 5.1 for how it collapses as its volume is decreased. We argue that there are two mechanisms for collapse. For short posts, as the curvature of the drop increases, it touches the surface below the posts, thus breaching the free energy barrier. For longer posts, the free energy barrier is removed when the surface free energy gained by the drop as it collapses wins over the surface free energy lost by increased contact with the hydrophobic posts. However, importantly, the collapse transition is usually preempted by the contact line of the drop retreating across the surface. Therefore collapse for drops on long posts will normally occur only when the drop covers a very small number of the posts. The analytical results are then compared to lattice Boltzmann simulations in section 5.2, where we find an excellent agreement between theory and simulations.

In three dimensions analytical calculations are generally not feasible, except for few special cases. In section 5.3, we consider one example where this can be done, when the surface is patterned with concentric circular ridges. A new feature in three dimensions is that the drop profile is not the same in all grooves. Therefore a collapsing drop will first touch the base surface at the centre of the drop. This feature is even more pronounced when we consider a square lattice of hydrophobic posts, which is a common experimental set-up. Here analytical solutions are not possible and we consider the problem numerically. In this case, we find that the base of the drop tends to form a bowl-shape, where the lines of contact depin and move down all but the outermost posts. We further argue that the tendency for the contact line to prefer to retreat across the surface than to collapse is even more pronounced in three

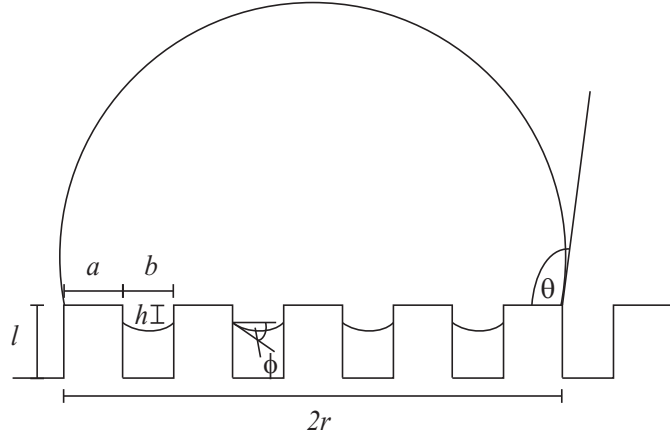


Figure 5.1: Schematic diagram of a suspended drop.

dimensions than in two.

5.1 Drop Collapse in Two dimensions: Analytical Results

Consider a two dimensional drop suspended on a regular array of hydrophobic posts as shown in Fig. 5.1. The posts have width a , spacing b and height l , and the substrate material has an intrinsic contact angle $\theta_e > 90^\circ$. The drop forms a circular cap with a contact angle θ , cross-sectional area S , radius of curvature R and base length $2r$.

We consider a drop with contact line that is pinned at the outer edges of two posts and we first assume that the contact line pinning persists as the drop spontaneously collapses. Considering the motion of a retreating contact line across a superhydrophobic surface (as, say, the volume of the drop is slowly decreased) shows that the line is pinned for $180^\circ > \theta > \theta_e$, as shown in chapter 4. After we have explained the possible collapse mechanisms, we shall return to a discussion of when they are preempted by depinning.

Given pinning, the base radius r is fixed and takes discrete values

$$r = (m + 1/2) a + m b, \quad (5.3)$$

where $2m + 1 = 1, 2, 3, \dots$ is the number of posts beneath the drop. The cross-sectional area of the drop, which is constant, can be written

$$S = r^2 \frac{\theta - \sin \theta \cos \theta}{\sin^2 \theta} + 2m b h + \frac{2m b^2}{4} \frac{\phi - \sin \phi \cos \phi}{\sin^2 \phi}. \quad (5.4)$$

The last term in Eq. (5.4) is due to the curved interface underneath the drop and $\phi = \theta_p - 90^\circ$, where θ_p is the angle this interface makes with the sides of the posts.

Our aim is to investigate when and how the collapse transition occurs. We do this by considering the behaviour of the drop free energy as a function of h , the distance it penetrates into the substrate (see Fig. 5.1). The non-constant contributions to the drop free energy F come from three terms. The first two correspond to the liquid–gas interfacial free energy above and beneath the surface and the third term is the free energy required by the liquid drop to wet the posts to a depth h .

$$f \equiv F/\sigma_{LG} = \frac{2r\theta}{\sin\theta} + \frac{2mb\phi}{\sin\phi} - 4mh\cos\theta_e, \quad (5.5)$$

where σ_{LG} is the liquid–gas interfacial tension.

We now consider the variation of the free energy with h . The drop will start to penetrate the posts if $\frac{df}{dh} < 0$ at $h = 0$, or equivalently $\frac{df}{d\theta} > 0$, since $\frac{dh}{d\theta} < 0$. Using the constraint of constant area to eliminate dh gives

$$\begin{aligned} df = & \frac{2r(\sin\theta - \theta\cos\theta)}{\sin^3\theta} (\sin\theta + \frac{2r}{b}\cos\theta_e) d\theta + \\ & \frac{2mb(\sin\phi - \phi\cos\phi)}{\sin^3\phi} (\sin\phi + \cos\theta_e) d\phi. \end{aligned} \quad (5.6)$$

Consider first $d\phi = 0$. Since $2r(\sin\theta - \theta\cos\theta)/\sin^3\theta > 0$, the condition for the drop to start collapsing is

$$\sin\theta + \frac{2r}{b}\cos\theta_e > 0|_{h=0}. \quad (5.7)$$

The corresponding critical drop radius of curvature and contact angle are

$$R_c = -\frac{b}{2\cos\theta_e}, \quad (5.8)$$

$$\sin\theta_c = -\frac{2r}{b}\cos\theta_e. \quad (5.9)$$

θ gets smaller and $\sin\theta$ gets larger as the drop penetrates the posts. As a result, once Eq. (5.7) is satisfied it will always be satisfied and once the drop has started to move it collapses fully, into the Wenzel state.

The drop will be in equilibrium at $h = 0$ on the threshold of the collapse transition. Therefore we may combine Eq. (5.9) and the Laplace pressure condition to show that $\theta_p =$

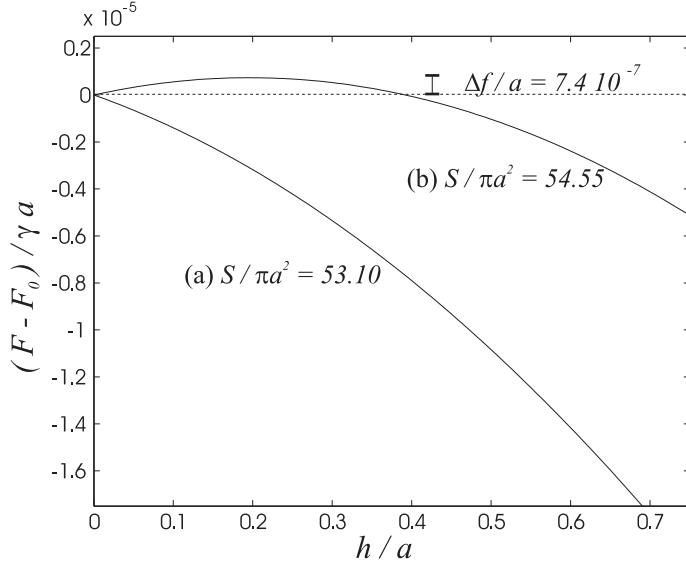


Figure 5.2: Normalised drop free energy against penetration depth when (a) the collapse transition occurs and (b) there is a free energy barrier between Cassie-Baxter and Wenzel states. F_0 is the drop free energy in the Cassie-Baxter state, σ_{LG} is the liquid–gas surface tension and S is the drop area. $m = 3$, $b/a = 1.5$, $\theta_e = 95^\circ$ and $\theta|_{h=0} = 111^\circ$ and 112° for (a) and (b) respectively.

θ_e , or $\phi = \theta_e - 90^\circ$ as expected from the Gibbs' criterion [111]. Hence, from Eq. (5.6) the free energy is at an extremum with respect to changes in ϕ . Calculating the second derivative confirms that this is a minimum and hence that the assumption $d\phi = 0$ is appropriate.

Typical plots of the free energy of a drop against h , the distance it penetrates into the substrate are shown in Fig. 5.2, where for simplicity we have neglected the corrections due to the curvature of the interfaces in the grooves. In Fig. 5.2(a), where we have used $m = 3$, $b/a = 1.5$, $\theta_e = 95^\circ$, and $\theta|_{h=0} = 111^\circ < \theta_c = 111.6^\circ$, the free energy is a smoothly decreasing function of h and the drop will collapse. In Fig. 5.2(b) on the other hand, for $\theta|_{h=0} = 112^\circ > \theta_c = 111.6^\circ$, there is a free energy barrier and therefore no collapse. The peak of the free energy barrier occurs at $\theta = \theta_c$ and the magnitude of the barrier is

$$\begin{aligned} \Delta f = & \frac{2r\theta_c}{\sin\theta_c} + \frac{2r^2\cos\theta_e}{b} \frac{\theta_c - \sin\theta_c\cos\theta_c}{\sin^2\theta_c} \\ & - \left[\frac{2r\theta}{\sin\theta} + \frac{2r^2\cos\theta_e}{b} \frac{\theta - \sin\theta\cos\theta}{\sin^2\theta} \right]_{\theta \equiv \theta|_{h=0}}. \end{aligned} \quad (5.10)$$

We have argued that, for $R < R_c$, there is no free energy barrier to drops penetrating hydrophobic posts. The critical radius depends on the post width a , the post separation b , the base radius r , and the equilibrium contact angle θ_e . It does not, however, depend on the

post height l . There is, however, another route to drop collapse [113], which will pre-empt this mechanism for shallow posts.

Prior to collapse the liquid drop has not penetrated the posts, the system is in mechanical equilibrium, and the Laplace pressure is the same everywhere. Thus the liquid–gas interface between the posts bows out with a radius of curvature equal to that of the circular cap R . The centre of the curved interface reaches a distance d into the posts:

$$d = R(1 - \cos \phi) \simeq \frac{b^2}{8R} \quad (5.11)$$

for small ϕ . As R gets smaller, d increases. When $d = l$ the liquid–gas interface touches the base surface initiating the transition between the Cassie-Baxter and Wenzel states. At this point there is a considerable free energy release because the drop is replacing two interfaces (liquid–gas and gas–solid) with a single liquid–solid interface. Consequently this transition is irreversible and for the opposite transition to occur (Wenzel to Cassie-Baxter) an external force is needed to overcome the free energy barrier. For this mechanism to be possible it is apparent from simple geometry that $d < b/2$.

Regions of parameter space where there is (i) collapse due to the contact line sliding down the posts, (ii) collapse due to the centre of the interface touching the base surface, (iii) no collapse are distinguished in Fig. 5.3. The crossover between regions (i) and (ii) occurs when

$$\cos \theta_e < -\frac{4l}{b}. \quad (5.12)$$

It is interesting to note that the crossover point between the two regimes (Eq. (5.12)) will slide to larger l as the posts are made more hydrophobic.

We now revisit the assumption that the contact line is pinned at the outer edges of the posts. As we have discussed in chapter 4, the (theoretical) advancing contact angle is 180° and therefore the line will not move outwards. The receding angle in the quasi-static limit is θ_e and therefore it will not jump inwards if $\theta_c > \theta_e$ or, equivalently, $\sin^2 \theta_c < 1 - \cos^2 \theta_e$. Using Eqs. (5.3) and (5.9), this is equivalent to

$$\cos^2 \theta_e < \left[4 \left(\frac{m + 1/2}{b/a} + m \right)^2 + 1 \right]^{-1}. \quad (5.13)$$

Fig 5.4(c) shows the maximum value of θ_e at which collapse will occur for different m and

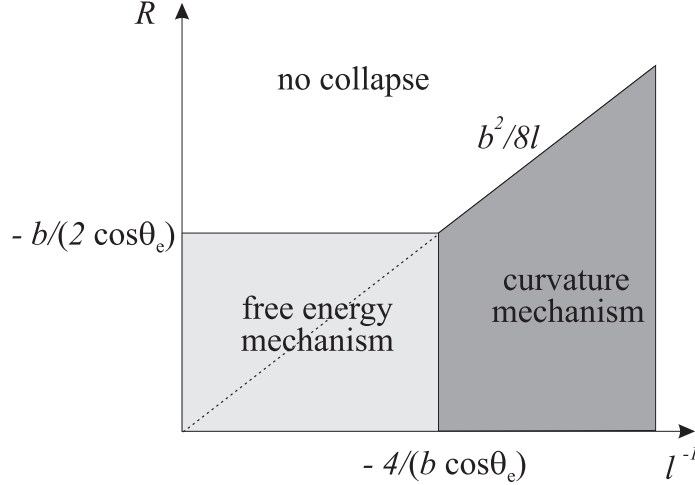


Figure 5.3: The crossover between the two different drop collapse mechanisms in two dimensions.

b/a . For small b/a collapse is strongly suppressed and only occurs for tiny drops on slightly hydrophobic surfaces. Even for $b/a \gg 1$ the tendency to depin is strong and the collapse occurs for small value of m unless θ_e is close to 90° . By setting $r = b$ in Eq. (5.7), we conclude that the transition will never occur spontaneously for $\theta_e > 120^\circ$.

In Fig. 5.4(a) and (b), we plot the critical radius of curvature at which a transition occurs R_c/a and the corresponding drop area (which we present as $\sqrt{S/\pi a^2}$) as a function of θ_e , m and b/a . As expected the critical radius of curvature does not depend on m ; it is a function of b/a and θ_e only. The critical base area of the drop does, however, depend on m and is smaller for larger values of m and a/b . The curves for increasing m terminate at decreasing values of θ_e corresponding to the contact line receding inwards before the drop is able to penetrate the posts.

5.2 Drop Collapse in Two Dimensions: Lattice Boltzmann Simulations

As we are considering the quasi-static problem, the drop is in equilibrium until the point of collapse and details of its dynamics should not affect the results. However we choose to implement physical equations of motion as this helps the drop to reach equilibrium quickly as its volume is decreased and for comparison to possible work on non-equilibrium collapse. The numerical results in this chapter were obtained using the liquid gas model discussed in section

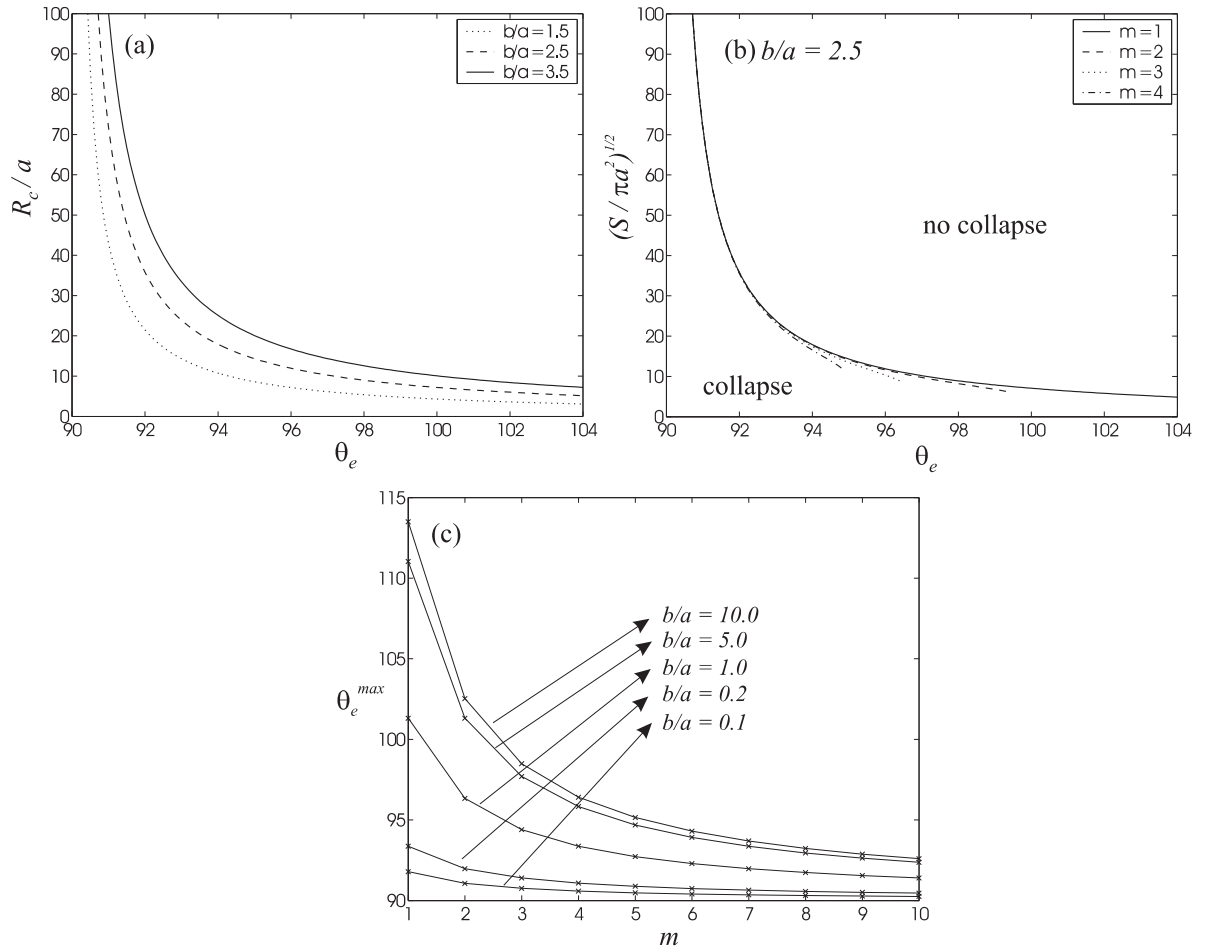


Figure 5.4: (a) Critical drop radius of curvature and (b) area (presented as $\sqrt{S/\pi a^2}$) for collapse as a function of the equilibrium contact angle θ_e for different substrate geometries and number of posts beneath the drop. (c) The maximum value of θ_e for which a spontaneous drop collapse can occur for different b/a and m .

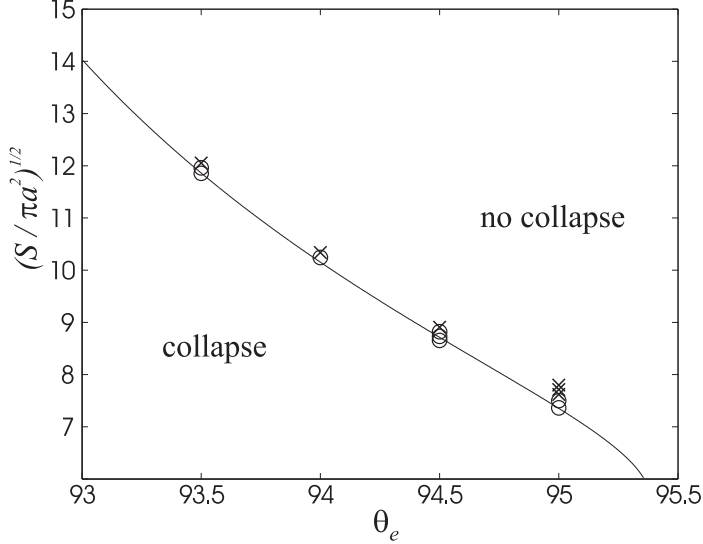


Figure 5.5: Critical drop area (presented as $\sqrt{S/\pi a^2}$) as a function of contact angle: comparison between the two-dimensional theory and simulations for $m = 3$, $a = 8$, $b = 12$. The circles and crosses represent drops which collapse and remain suspended respectively. The solid line is the theoretical prediction.

2.1.

To implement evaporation we need to slowly decrease the drop volume. To do this we vary the liquid density by -0.1% every 2×10^5 time steps to ensure that the evaporation timescale is well separated from the drop equilibration timescale. This in turn affects the drop volume as the system relaxes back to its coexisting equilibrium densities.

Results for two dimensions are compared to the analytic solution in Fig. 5.5, where we have used $a = 8$, $b = 12$, and $\theta_e = 95^\circ$. The critical drop area at which the collapse transition occurs is close to the theoretical value but critical radii obtained from simulations are typically too large by ~ 2 lattice spacings. This is because the liquid–gas interface is diffuse ($\sim 3 - 4$ lattice spacings). We checked that, as expected, R_c is independent of the post height and that h is the same everywhere underneath the drop.

5.3 Drop Collapse in Three Dimensions: Analytic Results for Circular Ridges

Analytic calculations in three dimensions are, in general, very difficult for several reasons. Firstly, the drop shape is not a spherical cap but is influenced by the underlying topological patterning. Secondly, the shape of the liquid–gas interface spanning the posts is complicated.

Thirdly, h , the distance the drop penetrates the substrate, is not necessarily the same everywhere. However, one example where analytical results are possible is when the surface is patterned with concentric circular ridges. This is our focus here. In the following section we shall consider a square lattice of hydrophobic posts, which is the more common experimental set-up. There we shall need to tackle the problem numerically.

Consider a drop lying on a surface patterned with concentric circular ridges of width a , height l , which are spaced a distance b apart. We take the centre of the drop and of the surface patterning to coincide and, as before, we assume that the contact line is pinned. In equilibrium, the Laplace pressure, and hence the curvature κ , is constant everywhere. Following [114],

$$\kappa = \frac{1}{\rho} \frac{g'(\rho)}{\sqrt{1 + (g'(\rho))^2}} + \frac{g''(\rho)}{(1 + (g'(\rho))^2)^{3/2}}, \quad (5.14)$$

where $z = g(\rho)$ is the height of the base of the drop at a radius ρ . For θ_e close to 90° , $g'(\rho)$ is small. Therefore we linearise Eq. (5.14). The solution subject to the boundary conditions

$$g(r_1)|_{r_1=(m+\frac{1}{2})a+mb} = 0 \quad (5.15)$$

$$g(r_2)|_{r_2=(m+\frac{1}{2})a+(m+1)b} = 0 \quad (5.16)$$

is

$$g(\rho) = \frac{\kappa}{4} \rho^2 - \frac{\kappa}{4} \frac{r_2^2 - r_1^2}{\ln r_2/r_1} \ln \rho - \frac{\kappa}{4} r_1^2 + \frac{\kappa}{4} \frac{r_2^2 - r_1^2}{\ln r_2/r_1} \ln r_1, \quad (5.17)$$

where r_1 and r_2 are the inner and outer radii of the $(m+1)$ th groove. Note that, in contrast to the two dimensional drop considered in section 5.1, the profile is not the same in all grooves. Therefore a drop collapsing via the curvature (shallow post) mechanism will first touch the base surface at the centre of the pattern.

If the posts are sufficiently long that curvature is not sufficient to induce collapse the interface starts to slide down the posts when $\theta = \theta_e$. This condition is first satisfied on the inner edge of a given groove and sequentially for $m = 0, 1, 2, \dots$. The boundary condition (Eq. (5.15)) is then replaced by

$$g'(r_1)|_{r_1=(m+\frac{1}{2})a+mb} = \cot \theta_e, \quad (5.18)$$

and the interface profile becomes

$$g(\rho) = \frac{\kappa}{4}(\rho^2 - r_2^2) + (\cot \theta_e r_1 - \frac{\kappa}{2}r_1^2) \ln(\rho/r_2). \quad (5.19)$$

Collapse occurs when the contact angle at the outer edge of a groove reaches θ_e . This occurs at a curvature

$$\frac{\kappa}{2}b + \cot \theta_e = 0. \quad (5.20)$$

Thus according to our linear approximation the drop penetrates all the grooves at the same time. For θ_e close to 90° this condition reduces to that for the striped surface (Eq. (5.7)) as expected.

If we now include the lowest order of the non linear terms, there is a correction to the curvature of the form

$$\Delta\kappa = -\frac{1}{2}\frac{g'(\rho)^3}{\rho} - \frac{3}{2}g'(\rho)^2g''(\rho) = \frac{3\cot^3 \theta_e}{b} - \frac{\cot^3 \theta_e}{r_2}. \quad (5.21)$$

Since $\Delta\kappa$ is larger for smaller r_2 , the drop will in fact first penetrate the grooves at the centre of the pattern. Nonetheless, since the correction is of order $\cot^3 \theta_e$ (and $\cot^3 \theta_e \ll 1$ for free energy driven collapse to occur) this differential depinning may not be noticeable in real experiments.

5.4 Drop Collapse in Three Dimensions: Square Lattice of Hydrophobic Posts

We now consider a square array of posts of widths $a = 3$ and spacing $b = 9$. Here analytical solutions are not possible and we tackle the problem numerically. We present results for both spherical drops and ‘cylindrical’ drops which demonstrate the relevant physics but are less demanding in computer time.

An important feature in three dimensions is that for a spherical (or cylindrical) drop on a square array of posts the base of the drop can form a bowl-shape where the lines of contact with the top of all but the peripheral posts depin and move down the posts leaving the drop suspended by just its outer rim. This was seen in simulations for drops of both cylindrical and spherical symmetry, and has recently been reported experimentally [115]. The depinning

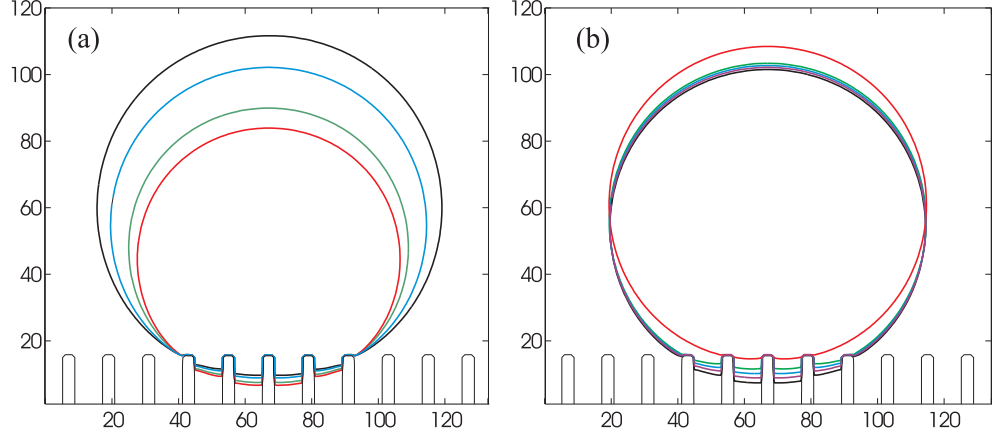


Figure 5.6: Equilibrium drop configurations. (a) $\theta_e = 95^\circ$ and varying volume. (b) Fixed volume and contact angles, $\theta = 93^\circ$ (black), 95° (purple), 97° (blue), 100° (green), and 110° (red).

occurs to reduce the distortion of the interface from spherical. Depinning is favoured for smaller drops and for contact angles close to 90° .

This is apparent in Fig. 5.6(a) which shows the equilibrium profile of the drop as its volume is varied with $\theta_e = 95^\circ$. As expected the drop penetrates further into the posts as the radius is decreased (corresponding to increasing curvature). Fig. 5.6(b) shows cross sections of the final states of 5 drops with volumes $V \simeq 4.5 \times 10^5$ (in the units of lattice spacing) equal to within $\sim 1\%$ but varying equilibrium contact angles in the range $\theta_e = 93^\circ$ to 110° . Although the drop penetrates deeper into the posts as the intrinsic contact angle approaches 90° there is no collapse (these values would give a collapse transition in two dimensions). Instead, for $\theta_e = 110^\circ$, the contact line depins and moves to cover 9 rather than 21 posts. Note that this jump also corresponds to a transition to the state when the drop is suspended on all the posts beneath it, not just those around its rim.

To explore the depinning further, and to try to find a collapse transition, we turned to the geometry of a cylindrical drop on a square array of posts. This preserves the physics whilst allowing us to exploit the quasi-two-dimensional geometry to run larger simulations. Results are shown in Fig. 5.7 for $\theta_e = 93^\circ$. Successive frames show how the drop profile evolves as its volume is quasi-statically decreased (note that they are drawn on different scales). Initially, the contact line is pinned at the edges of the posts and the drop penetrates further beneath the posts as the radius is decreased. However, as the drop continues to decrease in size, the drop contact angle reaches the receding angle and the contact line depins. As it depins we observe

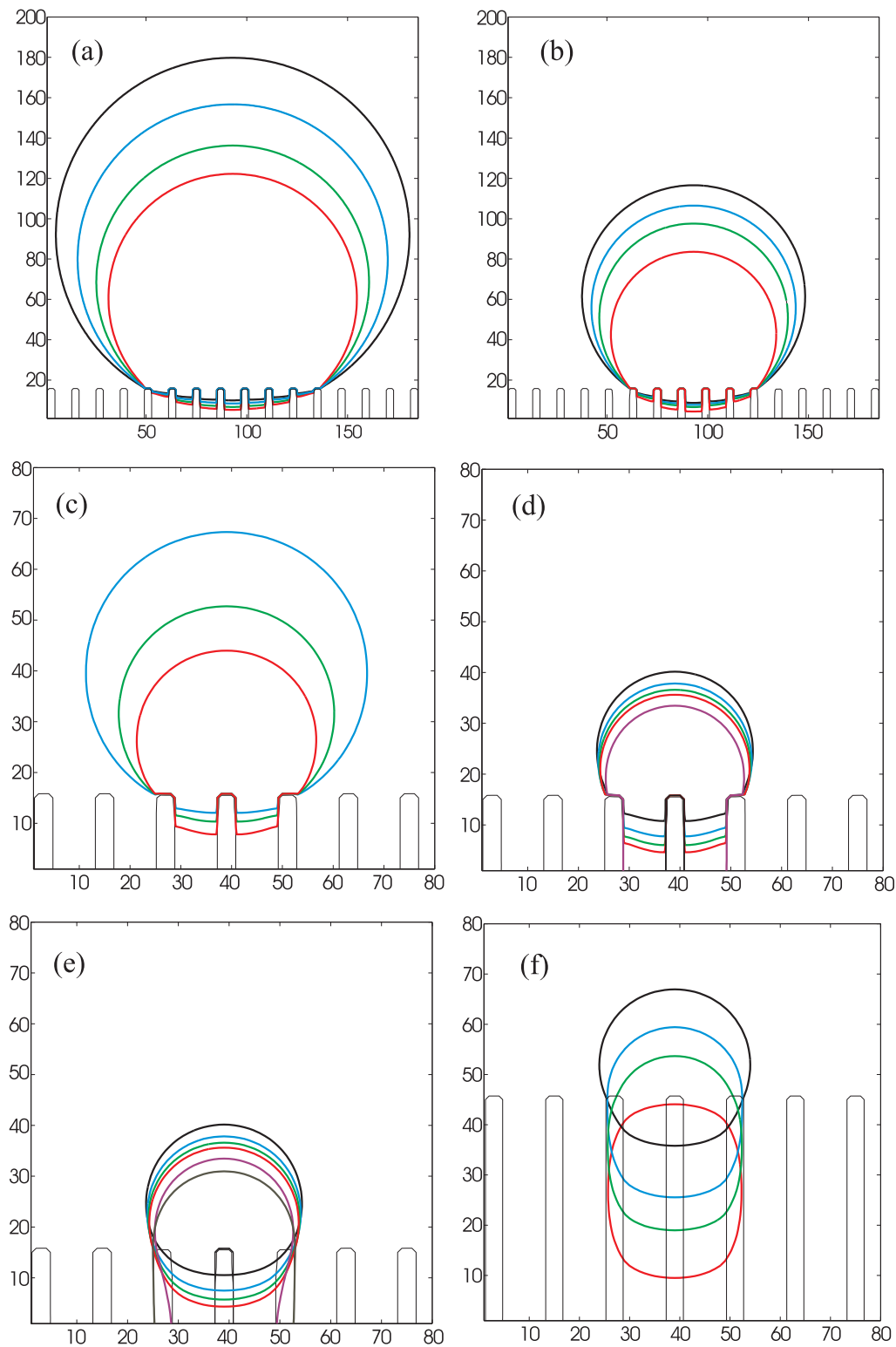


Figure 5.7: Evolution of a cylindrical drop on a square array of posts of width $a = 3$, spacing $b = 9$ and height $l = 15$. (a–c) Evolution before collapse showing depinning of the receding contact line (note the scale change between (b) and (c)). (d–f) Motion of the collapsing drop: (d) cross sections in the plane bisecting the posts. (e) same times as (d), but in the plane bisecting the gap between the posts. (f) cross sections in the plane bisecting the gap, but with $l = 45$ to enable the collapse to be followed to later times.

that the penetration into the posts decreases (because the drop is approximately spherical and the base area is reduced), thus moving the system away from the point where either a curvature or a free energy driven collapse is favourable. Eventually collapse is seen but only, for this example, when the drop spans just three posts. Note that for $l = 45$ the drop stops moving once it is fully inside the posts as its free energy becomes independent of height: it forms a liquid bridge connecting several neighbouring posts.

Indeed, we expect from the two dimensional calculations that collapse is preempted by depinning for posts with $b/a \sim 1$ until the drops are very small. In three dimensions depinning will be even more important because the receding contact angle is larger than θ_e , its value in two dimensions, because the distortion of the interface makes it more favourable for the drop to depin. From Fig. 5.7(a) and (b), we obtain $\theta_R \sim 120^\circ$.

5.5 Discussion

To conclude, we have studied the behaviour of an evaporating drop on a superhydrophobic surface. As the drop volume decreases quasi-statically it can move in three ways: (i) the drop attains its receding contact angle and the contact line moves inwards across the surface, (ii) the free energy barrier to collapse vanishes and the drop moves smoothly down the posts, and (iii) the drop touches the base of the surface patterning and immediately collapses. The depinning (i) is predominant and, unless the posts are widely spaced, or the surface is only very weakly hydrophobic, collapse occurs only for drops spanning a very small number of posts.

This suggests strategies that could be used to suppress transitions to the Wenzel state. Long enough posts are needed to prevent curvature-driven collapse, i.e. $l \gtrsim b^2/R$, and the free energy barrier to the transition can be enhanced by choosing θ_e as large as possible and using closely spaced posts, i.e. $b \lesssim a$. A mobile contact line will also help as this will relax any build up of curvature. Furthermore, since collapse occurs when the contact angle at the side of the posts reaches the equilibrium contact angle, we can fine-tune the shape of the posts so that the drop is in a meta-stable Cassie-Baxter state, even when the surface is intrinsically hydrophilic. Recently, this strategy has been shown to be successful in experiments by Tuteja *et al.* [13] and Cao *et al.* [14].

Our results are in line with recent experiments [112, 113, 115, 116]. In [113], for long posts, the contact line retreated as the drop shrank and collapsed only at the very end of

evaporation. For short posts, a few depinning events were followed by collapse at a radius consistent with a curvature-driven mechanism, $R_c \propto b^2/l$. It is not clear, however, whether the drop interface was suspended on all the posts or just those at the rim at the point of collapse: this detail is important in determining the constant of proportionality. In [115], the various drop configurations found here are also observed, including the depinning of the drop from all but the outer posts. In [116], for the somewhat different situation of drops bounced onto a surface, the critical pressure for impalement varied linearly with post height for short posts, as expected for curvature-driven collapse, and showed a clear crossover to a length-independent regime for longer posts, consistent with a drop overcoming a free energy barrier.

CHAPTER 6

Capillary Filling in Patterned Channels

“*Make the layouts rough and the ideas fancy.*”

- Stavros Cosmopoulos

Recent years have seen rapid progress in the technology of fabricating channels at micron length scales. Such microfluidic systems are increasingly finding applications, for example, in diagnostic testing and DNA manipulation and as microreactors. As narrower channels are used, to conserve space and reagents, surface effects will have an increasing influence on the fluid flow. In particular, it may be possible to exploit the chemical or geometrical patterning of a surface to control the flow within the channels. Indeed first steps in this direction have already been taken: for example, superhydrophobic surfaces were used to introduce slip lengths of the order a few μm [17–21] and oriented grooves were used to enhance mixing [117].

Our aim in this chapter is to describe the way in which a fluid penetrates a microchannel, when the motion is driven by the Laplace pressure across the liquid-gas interface. We first study the case where the surface is smooth in section 6.2. We use this as a benchmark against which to test our lattice Boltzmann models: the liquid gas model, the standard BGK binary model and the multiple relaxation time binary model. We then extend the study to microchannels patterned with posts or ridges in section 6.3 and find that the hysteretic behaviour that results from the surface patterning can be a substantial factor in controlling how the fluid moves down the channel. Ridges or posts oriented parallel to the flow speed up capillary filling while those perpendicular to the flow pin the interface and suppress, or sometimes prevent, filling. We investigate the rate at which the microchannel fills, finding that it is highly dependent on both the geometry and the spacing of the posts. In particular, we demonstrate that a patterned surface can act as a valve, allowing filling in one direction only.

6.1 Washburn's Law

The classical analysis of capillary penetration is due to Lucas [118] and Washburn [119].

Consider a capillary of height h with an infinite reservoir of liquid of dynamic viscosity $\eta = n\nu$ at one end. If the walls of the capillary are hydrophilic the liquid will move to fill it with a mean velocity (assuming two dimensional Poiseuille flow)

$$\bar{v} = -\frac{h^2}{12\eta} \frac{dp}{dx}, \quad (6.1)$$

where $\frac{dp}{dx}$ is the pressure gradient that sets up the flow. The driving force for the flow is provided by the decrease in free energy as the fluid wets the walls or, equivalently, the Laplace pressure across the interface. Hence

$$\frac{dp}{dx} = -\frac{\sigma_{LG}}{Rl}, \quad (6.2)$$

where σ_{LG} is the surface tension of the liquid interface and $R = h/2\cos\theta_A$ is its radius of curvature and l is the length of liquid in the tube. Substituting $\frac{dp}{dx}$ into the parabolic flow profile and using $\bar{v} = dl/dt$ gives Washburn's law

$$l = (\sigma_{LG}h \cos\theta_A / 3\eta)^{1/2} (t + t_0)^{1/2}, \quad (6.3)$$

where t_0 is an integration constant.

Note that it is appropriate to use, not the static, but the advancing contact angle θ_A , as this controls the curvature of the interface and hence the Laplace pressure. Washburn's law assumes that there is no resistance to motion from any fluid already in the capillary. Therefore it applies to a liquid displacing a gas or one liquid phase displacing a second only if the dynamic viscosity of the invading phase η_A is large compared to that of the displaced fluid η_B . If the dissipation in the displaced fluid is taken into account and assuming that the average velocity is the same in the two phases, the modified Washburn's law becomes

$$\eta_A \frac{l^2}{2} + \eta_B (Ll - \frac{l^2}{2}) = \frac{\sigma_{LG}h \cos\theta_A}{6} (t + t_0), \quad (6.4)$$

where L is the total length of the capillary. The derivation also assumes incompressibility, and neglects inertial effects [120, 121], gravity [122] and any deviations from a Poiseuille flow

profile at the inlet or the interface [121, 123–125].

6.2 Capillary Filling in Smooth Channels

We first consider capillary filling in smooth channels, before investigating the influence of patterned walls in section 6.3. When the dynamic viscosity of the liquid phase is considerably larger than that of the gas phase, we expect our lattice Boltzmann simulations to reproduce Washburn’s law (6.3). However, we find that this is not always the case. The liquid-gas model does not reproduce Washburn’s law due to the condensation of the gas phase at the interface. This condensation mechanism causes the asymptotic behaviour of the capillary penetration to be faster than $t^{1/2}$. This problem can be resolved by either increasing the liquid-gas density ratio [126] or by using the binary model. The latter is discussed in section 6.2.2 for both the standard BGK and the multiple relaxation time method.

6.2.1 Liquid Gas Model: The Evaporation-Condensation Problem

Numerical results showing capillary filling of a smooth channel are presented in Fig. 6.1(a) for the liquid-gas model. The plot is for a channel of length $L = 640$, infinite width and height $h = 50$. Reservoirs (480×200) of liquid and gas are attached at each end of the capillary. The two reservoirs are connected to ensure that they have the same pressure. The parameters of the system are chosen so that the equilibrium contact angle $\theta_e = 60^\circ$, $\sigma_{LG} = 7.7 \times 10^{-4}$, $n_{\text{liquid}} = 4.11$, $n_{\text{gas}} = 2.89$, $\eta_{\text{liquid}} = 3.43$ and $\eta_{\text{gas}} = 0.09$. The circles in Fig. 6.1(a) show the capillary penetration as a function of time. When compared against the theoretical prediction of Washburn (given by the solid line) we observe that agreement is very poor. One possible explanation behind this might be that viscous dissipation in the gas phase cannot be ignored. However, taking this into account only makes the predicted flow even slower.

The reason behind the large discrepancy between theory and simulation can be clearly seen if we observe the fluid flow profile near to the meniscus, as plotted in Fig. 6.1(b). We find that whilst fluid in the liquid phase is moving to the right and filling up the capillary, the fluid in the gas phase is moving *left* and condensing to form liquid, which helps to significantly increase the speed of the interface. Hence the Washburn’s law breaks down. This is seen even more clearly in Fig. 6.1(c), which shows the x component of the fluid velocity as a function of distance down the tube. Similar observation has also been reported by Diotallevi *et al.* [126].

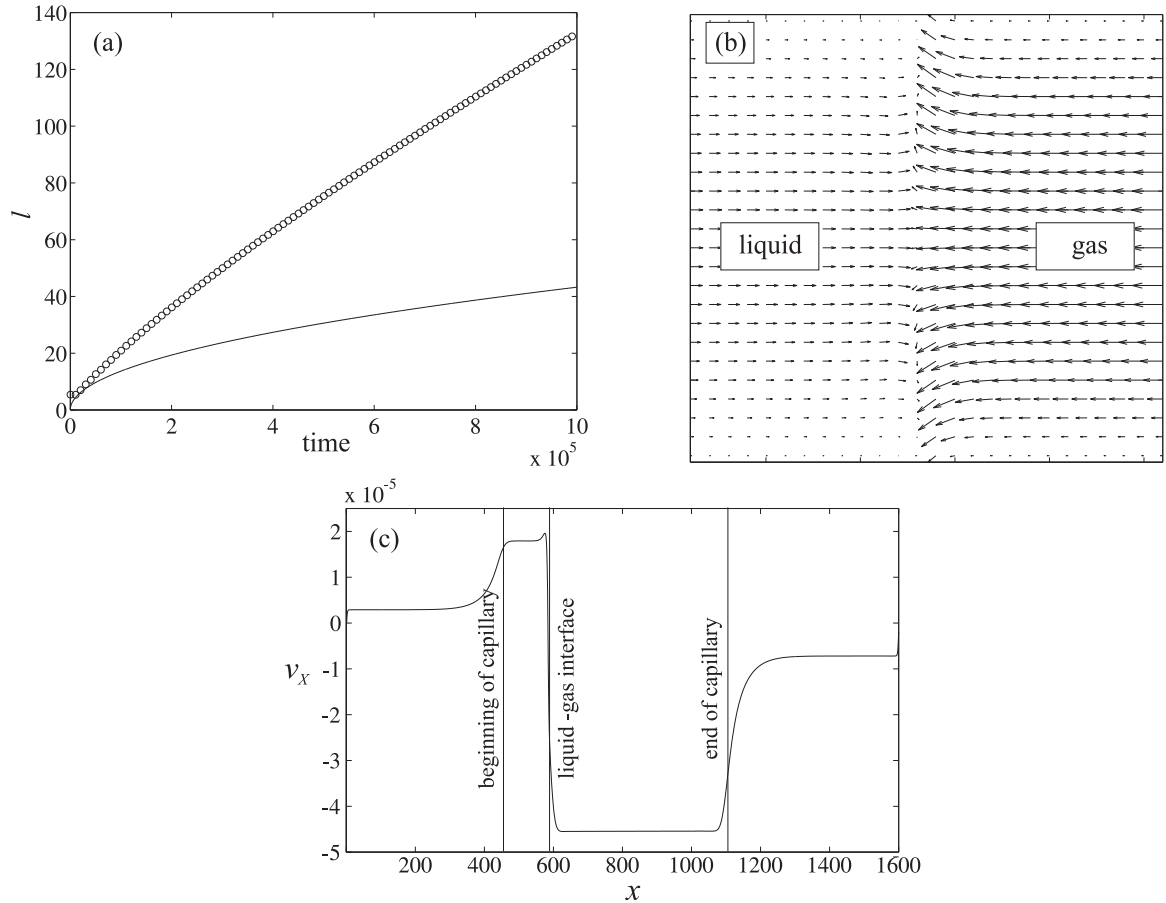


Figure 6.1: (a) The distance of the liquid-gas interface along the capillary as a function of time. Circles are the lattice Boltzmann simulation results for $\theta_e = 60^\circ$, $\sigma_{LG} = 7.7 \times 10^{-4}$, $n_{\text{liquid}} = 4.11$, $n_{\text{gas}} = 2.89$, $\eta_{\text{liquid}} = 3.43$ and $\eta_{\text{gas}} = 0.09$. The solid line is the Washburn's law (6.3). (b) The velocity field around the liquid-gas interface during capillary filling using the standard liquid-gas model. (c) The x component of the velocity as a function of x at the centre of the capillary.

It is possible that the condensation mechanism is important if the experiments are done near the critical point or when the gas phase is super-saturated. However, in typical experiments the liquid gas density ratio is of order 10^3 and gas condensation to liquid should be negligible compared to the advective flow driven by the laplace pressure. Furthermore, in many situations, the liquid and the gas phase are of different substances, rather than the liquid and gas phase of the same substance.

If we increase the density ratio in our simulations, the dynamics of the gas phase become less important and the discrepancy between the numerical results and analytical predictions become less significant. By fine-tuning our simulation parameters, we are able to reduce the effects of the gas phase and reproduce the Washburn's law. Nonetheless, we find that the dynamics of the gas phase depends sensitively on the density and viscosity of the liquid and gas phase. For example, changing the gas viscosity (and keeping everything else the same) may change the flow direction of the gas phase. Therefore, a typical simulation will have a small but still noticeable effect coming from the condensation of the gas phase. With this in mind, we turn to the binary model, which provides a superior way of removing the evaporation-condensation problem.

6.2.2 Binary Model

Unlike the liquid gas model, the binary model does not suffer from the evaporation-condensation problem. The particles are now of different types, and hence the gas phase can no longer condense to the liquid phase, and similarly, the liquid phase can not evaporate to the gas phase. This constraint also implies that the average velocity in the two phases are the same. This is an important assumption that we have used when deriving Eq. (6.4).

Numerical results showing capillary filling of a smooth channel are presented in Fig. 6.2(a) for the binary lattice Boltzmann model. The simulation setup is the same as in the liquid gas model and the parameters of the system are chosen so that $h = 50$, $L = 640$, $\theta_e = 60^\circ$, $\sigma_{LG} = 0.0188$, $\rho_A = \rho_B = 1.0$, $\eta_A = 0.83$, $\eta_B = 0.03$ and $M = 0.05$. The solid line in Fig. 6.2(a) is a fit to the Washburn's law using the measured values of the contact angle and correcting for the small viscosity of the displaced B -component. The fit is excellent, except very close to the beginning of the simulation where the expected deviations from Washburn's law due to inertial effects and deviations from a Poiseuille flow profile are observed. The fluid flow profile near to the meniscus is also shown in Fig. 6.2(b). Unlike the liquid gas model, in the binary

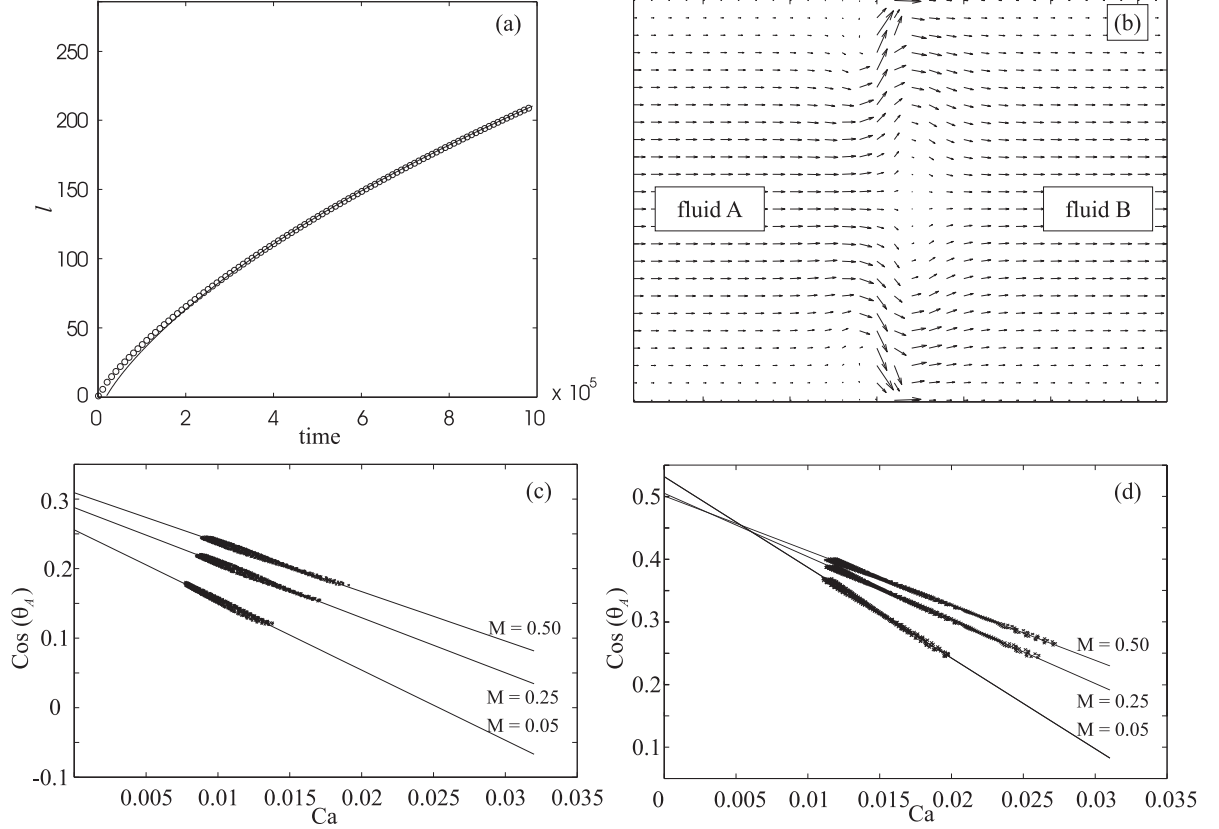


Figure 6.2: (a) The distance of the fluid-fluid interface along the capillary as a function of time. Circles are the lattice Boltzmann simulation results for $h = 50$, $\theta_e = 60^\circ$, $\sigma_{LG} = 0.0188$, $\rho_A = \rho_B = 1.0$, $\eta_A = 0.83$, $\eta_B = 0.03$ and $M = 0.05$. The solid line is a fit to the Washburn's law using the measured advancing contact angle and correcting for the small viscosity of the displaced B -component. (b) The velocity field around the fluid-fluid interface during capillary filling using the standard binary model. (c) and (d) The measured advancing contact angle using the standard BGK and multiple relaxation time lattice Boltzmann method. The crosses are the simulation results and the solid line is a linear fit of $\cos \theta_a$ with respect to the capillary number [127].

model, both fluid components are moving in the same direction and with the same average velocity.

The results shown in Fig. 6.2(a) are obtained using the standard BGK lattice Boltzmann method. While it reproduces the $t^{1/2}$ time-dependence expected from the Washburn's law, we find that capillary filling is considerably slower for the standard BGK method when compared to the multiple relaxation time lattice Boltzmann results, using exactly the same simulation parameters. This discrepancy is best explained by considering the advancing contact angle as a function of the capillary number (The variation in the capillary number comes from the fact that the liquid velocity decreases as a function of time as liquid A fills the capillary). Fig. 6.2(c) and (d) show that the measured advancing angle decreases linearly as the capillary number Ca decreases [127] for both the standard BGK and multiple relaxation time lattice Boltzmann simulations. To the lowest order in Ca , the advancing angle is related to the equilibrium angle and the capillary number by

$$\cos \theta_A = \cos \theta_e - Ca \log(Kh/l_s), \quad (6.5)$$

where K is a constant, h is the typical length scale of the system and l_s is the effective slip length at the three phase contact line.

In the multiple relaxation time lattice Boltzmann method, the advancing contact angle goes to the correct equilibrium contact angle as $Ca \rightarrow 0$. We obtain $\theta_A|_{Ca \rightarrow 0} = 58^\circ$, 60° and 60° respectively for $M = 0.05$, 0.1 and 0.5 . The role of the mobility M is to change the effective slip length l_s : l_s increases with M . In the standard BGK method, on the other hand, we obtain $\theta_A|_{Ca \rightarrow 0} = 75^\circ$, 73° and 72° for $M = 0.05$, 0.1 and 0.5 and the advancing angle is consistently higher for all values of Ca than in the multiple relaxation time lattice Boltzmann method. Since the speed of capillary filling depends on θ_A , this explains why capillary filling is considerably slower in the standard BGK method. This result is also consistent with those presented in section 2.2.3, where we obtain that the measured equilibrium angle is higher than that predicted analytically for the standard BGK approximation.

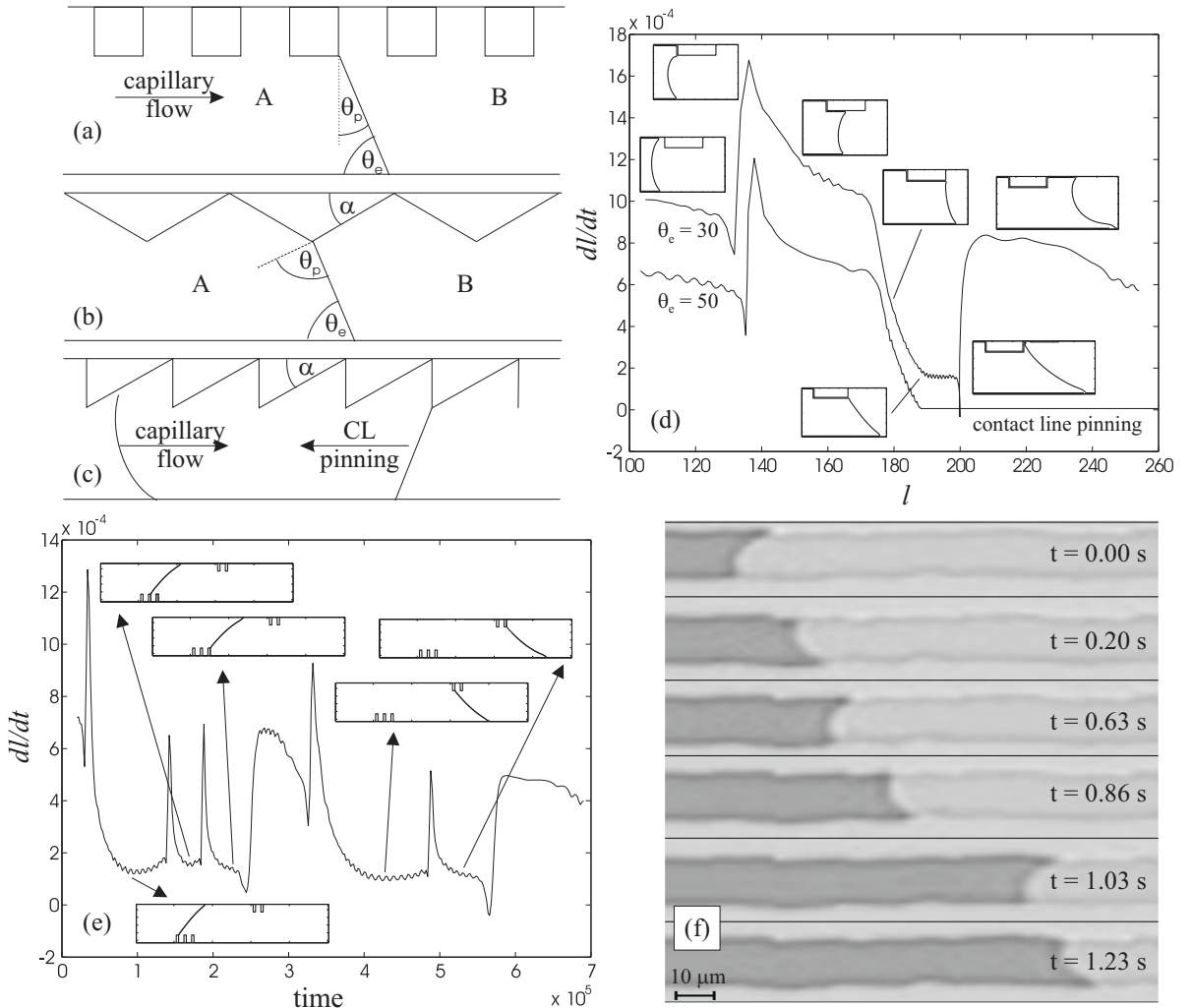


Figure 6.3: Pinning of the contact line during capillary filling when the top wall is patterned with (a) squares, (b) triangles, and (c) ratchets. (d) Interface velocity dl/dt when one of the walls is decorated with a single 40×10 post. (e) Interface velocity when the bottom wall is decorated with three posts and the top wall is decorated with two posts. The posts have height 10 and width 5. (f) Experimental results on capillary filling in patterned channels. Local pinning temporarily holds the capillary front on one of the two microchannel sidewalls, while the interface advances along the opposite sidewall. The experiments shown in panel (f) were performed by Mr Salvatore Girardo and Dr. Dario Pisignano.

6.3 Capillary Filling in Patterned Channels

6.3.1 Two Dimensional Results

We now discuss capillary filling in a channel with topological patterning on the surface. On stepped surfaces the driving force of the Laplace pressure must be sufficient to overcome any hysteresis due to the surface patterning. We shall assume that the contact angle of the *A*-component is $< 90^\circ$ i.e. this is the fluid that may fill the capillary, and that there is no intrinsic hysteresis.

We first consider two dimensions, and a channel where one of the walls is patterned by square posts, as shown in Fig. 6.3(a). (The same results apply for a three dimensional channel with ridges which are translationally invariant perpendicular to the flow.) According to the Gibbs' criterion, for an interface moving very slowly, the contact line will remain pinned on the edge of the posts until θ_p , the angle the interface makes with the side of the posts, reaches the equilibrium contact angle θ_e . It follows immediately (see Fig. 6.3(a)) that there will be no capillary filling unless

$$\theta_p \equiv 90^\circ - \theta_e < \theta_e, \quad (6.6)$$

that is, $\theta_e < 45^\circ$. If the surface is patterned by triangular posts, with sides at an angle α to the edges of the channel as shown in Fig. 6.3(b), the condition for capillarity is less stringent, namely $\theta_e < 90^\circ - \alpha/2$. Hence the surface in Fig. 6.3(c) will allow filling from left to right, but not from right to left if $45^\circ < \theta_e < 90^\circ - \alpha/2$.

Numerical results showing how the interface behaves as it approaches a post with finite velocity are presented in Fig. 6.3(d) for channel height $h = 50$, post height $h_p = 10$, post width $w_p = 40$ and equilibrium contact angles $\theta_e = 30^\circ$ and 50° . Here l , the length of the liquid column, is measured at the centre of the capillary channel. As the interface approaches the post, it is slowed down by dissipation caused by the post. However, once the interface is able to respond to the wetting potential of the post, it quickly wets the leading edge. The interface slows as it moves over the top the post – if the post was infinite in extent it would reach the speed appropriate to a channel of height $h - h_p$. Once the trailing edge of the post is reached there is a substantial decrease in velocity as the interface becomes pinned. For $\theta_e = 30^\circ$ the interface is able to proceed, but for $\theta_e = 50^\circ$ it remains pinned, consistent with the condition in Eq. (6.6). For the same value of θ_e , the variation in velocity is more pronounced for higher

posts.

Fig. 6.3(e) shows the dynamics as the interface moves along a capillary with groups of posts on both the top and bottom surfaces of the channel. This simulation demonstrates several features of the motion. First, as the interface reaches the three posts on the lower edge of the channel, it takes longer to depin from the first post it reaches. This is because the free end of the interface takes time to slide along the top of the capillary until it reaches an angle where it can pull the pinned end away from the trailing edge of the post. For the second and third posts the interface is already aligned diagonally across the channel and does not need to move so far. It is also worth noting here that if the posts are very high, the non-wetting liquid (or gas) can be trapped in between the posts. Once the interface reaches the posts at the top of the channel it remains pinned on the first of these for some time until the interface again takes up a diagonal configuration, but now with the bottom edge leading.

Such switching between two diagonally aligned interface configurations has been observed in experiments on capillary filling in channels with lateral root-mean-square roughness $1 \mu\text{m}$, as shown in Fig. 6.3(f). The channels were realised by optical lithography employing plastic photomasks patterned with a laser printer. Polymer microchannels were then obtained by subsequent replica molding with polydimethylsiloxane. A $2 \mu\text{l}$ drop of water was released at the entrance of the microchannels and the penetrating interface was imaged by a 320×240 pixels, 30 fps camera. Experiments have also shown the interface waiting longer at the beginning of a line of posts engineered to lie on one surface of a microchannel.

A microchannel with both walls regularly patterned with square posts is shown in Fig. 6.4(a). We take d and t to be the post width and height and p to be the period of the patterning. For simplicity we shall assume that the patterning on the second wall is identical, but with the surface pattern shifted by a distance s . The interface will remain pinned between the posts if any of the following conditions are met

$$\theta_e > 45^\circ, \quad \tan \theta_e > \frac{s}{h - 2t}, \quad \tan \theta_e > \frac{p - s}{h - 2t}. \quad (6.7)$$

This is illustrated in Fig. 6.4(b), where we have defined $h^* = h - 2t$. Note, in particular, that for posts aligned across the channel no capillary filling is possible for any value of the contact angle.

We now compare capillary filling dynamics in smooth and regularly patterned capillaries.

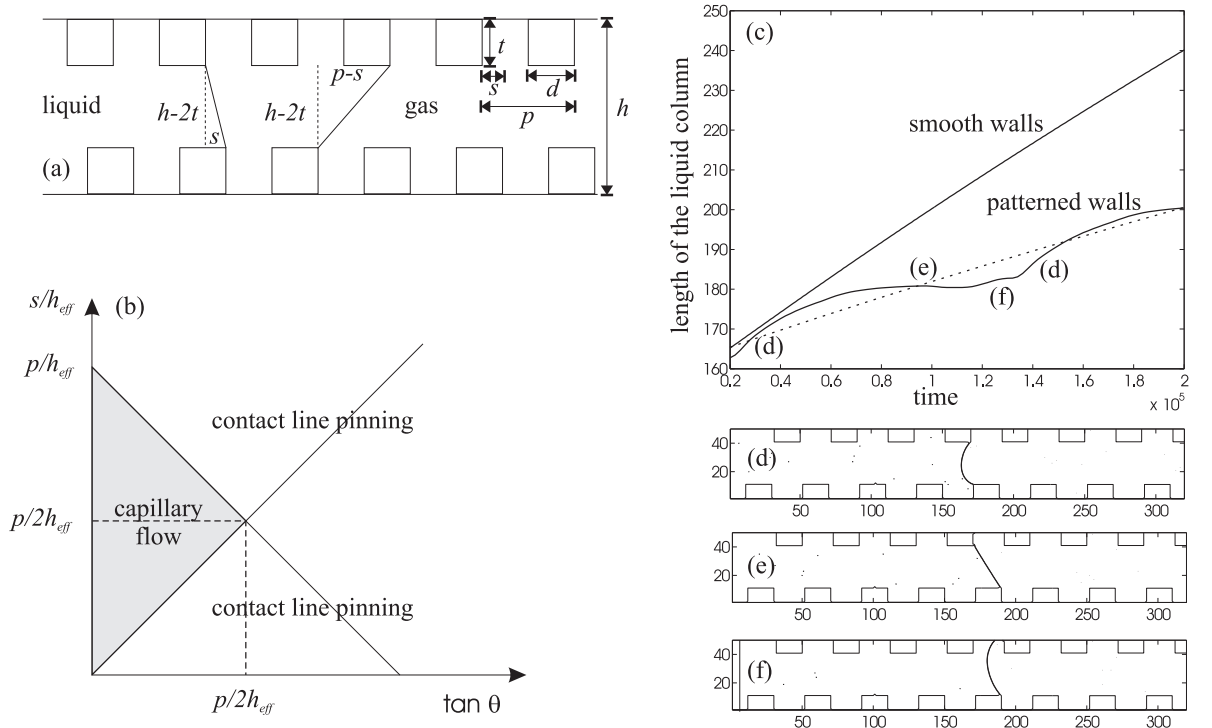


Figure 6.4: Patterned capillary walls: (a) schematic diagram of the channel geometry, (b) phase diagram showing regions of contact line pinning and capillary flow, (c) lattice Boltzmann simulation of patterned capillary rise dynamics for $\theta_e = 30^\circ$, $d = 20$, $t = 10$, $p = 40$, $h = 50$, $s = 20$, $\sigma_{LG} = 0.0188$, $\rho_A = \rho_B = 1.0$, $\eta_A = 0.83$, and $\eta_B = 0.03$. The dashed line corresponds to a fit to Washburn's like dynamics, $l = 0.3679 \times t^{1/2}$, which corresponds to $\theta_A = 69^\circ$. This dynamics is slower than that on smooth walls, which is also shown here for comparison. (d-f) The interface configuration at times indicated in panel (c).

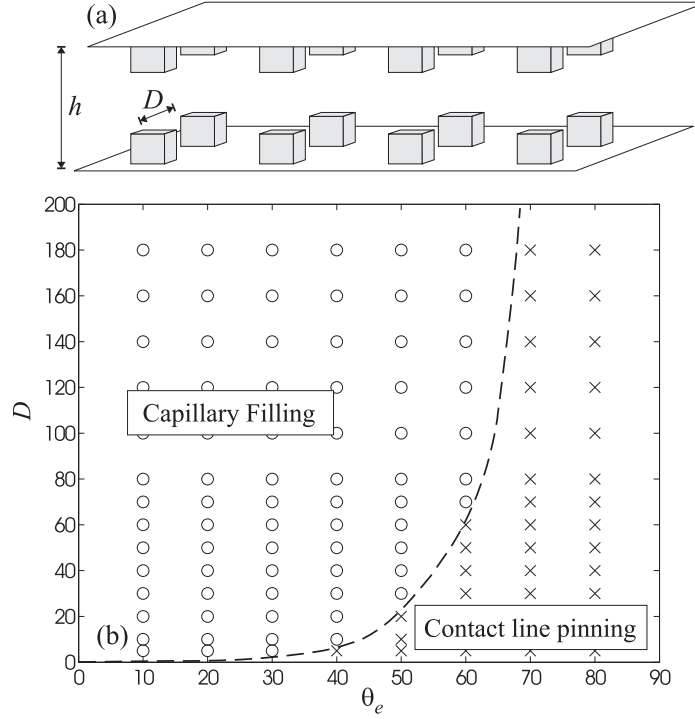


Figure 6.5: Two dimensional surface patterning: (a) the surface geometry; (b) regions of contact line pinning and capillary flow as a function of post separation and equilibrium contact angle. The channel height is kept constant at $h = 50$. The dashed line is a guide to the eye.

Therefore we choose $d = 20$, $t = 10$, $p = 40$, $h = 50$, $s = 20$, and $\theta_e = 30^\circ$. The penetration length as a function of time is shown in Fig. 6.4(c), and the simulations were run for $l > 160$ to ensure that we are far away from the inertial regime. Capillary flow persists but it occurs at a rate slower than that on smooth walls, which is also shown in Fig. 6.4(c) for comparison. Capillary penetration is particularly slowed down when A-liquid wets the side of the posts. Fig. 6.4(d-f) shows the interface configuration at various points on one of the Fig. 6.4(c) curves.

6.3.2 Three Dimensional Results

We now consider three-dimensional surface patterning. Both walls of the capillary are patterned with 20×20 square posts of height 10. The posts face each other across the channel, which is of height $h = 50$. They are separated by spaces of length D in the direction perpendicular to the flow. This geometry is illustrated in Fig 6.5(a), which shows a side view of the channel. For $D = 0$, the case corresponding to ridges across the channel, the Gibbs' criterion predicts that the interface will always remain pinned between the trailing edges of a pair of opposing posts. For $D \neq 0$, however, the motion can be driven by the portion of the interface that lies between the posts.

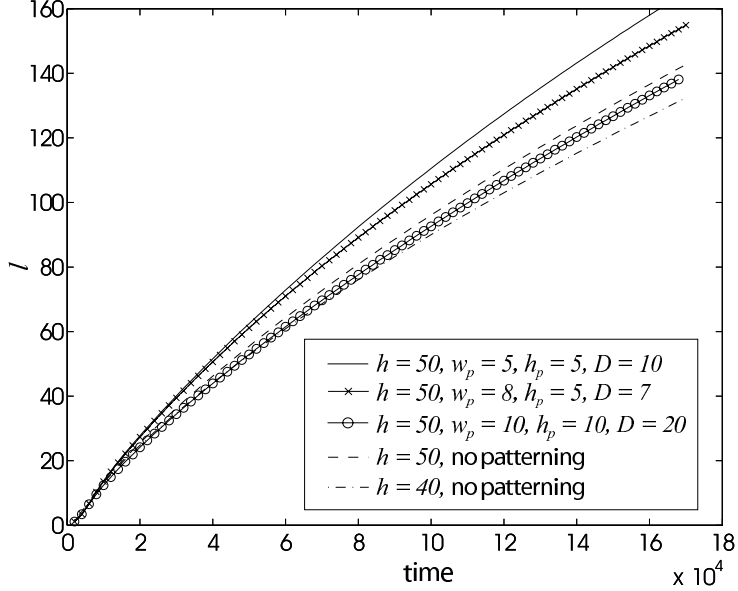


Figure 6.6: The length of the column of A -liquid plotted against time for different surface patterning. The channels' intrinsic contact angle is $\theta_e = 30^\circ$. Other parameters as in Fig. 6.2.

Fig 6.5(b) shows the crossover between capillary filling and contact line pinning as a function of D and θ_e . For $\theta_e \lesssim 30^\circ$, a small gap in between the posts is enough to allow filling. As the interface moves through the gap and protrudes beyond the posts, it is able to depin, initially from the side of the posts.

For $\theta_e \gtrsim 60^\circ$, however, filling is strongly suppressed. This is due to two complementary effects: the force driving the interface though the gaps becomes weaker and the pinning on the sides of the posts becomes stronger. Note that the part of the interface that lies in between the posts can bow out further as D is increased and it is possible that the leading interface could touch the next row of posts, thus providing an alternative mechanism to depin the interface from the edges of the posts.

We have also varied the relative height of the posts with respect to the channel width and find that the contact line pinning condition depends only very weakly on the channel height. This is because the interface behaviour is primarily determined by depinning from the side edges of the posts. It is also worth noting that we neglect fluctuations in our simulations.

So far, we have considered surfaces patterned with ridges oriented perpendicular to the flow and square posts, cases where pinning by the posts suppresses, or even prevents capillary filling. We now identify a situation where patterning can be used to speed up capillary flow, ridges aligned *along* the flow direction. In Fig. 6.6, we compare the lengths of the A column, plotted as a function of time, for a channel of height $h = 50$ with infinitely long ridges of width

(w_p), height (h_p) and separation (D) (i) 5, 5, and 10, (ii) 8, 5, and 7, and (iii) 10, 10, and 20 lying along the channel. In all these cases the channels have the same surface roughness $r = 1 + 2h_p/(w_p + D) = 5/3$. For comparison, we also show smooth channel simulations for $h = 40$ and $h = 50$. It is clear from Fig. 6.6, that it is possible to increase the rate of capillary filling by patterning the channels (cases (i) and (ii)). This occurs because there is no contact angle hysteresis in this geometry and because the total surface area per unit length wetted by the A -liquid is increased over the flat channel value by the roughness factor r . However, from Fig. 6.6 it is apparent that the rate of filling is not just controlled by r . This is because surface roughness distorts the liquid flow from a parabolic profile and hence increases the dissipation. As shown in Fig. 6.6, the dissipation increases as the distance between two neighbouring ridges is reduced (case (ii)) and as the size of the ridges relative to the channel height is increased (case (iii)). The filling speed is a competition between the increased energy gain of wetting a grooved channel and the additional dissipation caused by the distortion of the flow.

6.4 Discussion

In this chapter, we have considered capillary filling in smooth and patterned channels. We first used the problem of capillary filling in a smooth channel to benchmark the numerical methods. We assessed two different ways of simulating capillary flow. Firstly, using the liquid gas model, the filled length of a capillary tube was found to increase more rapidly than predicted by Washburn's law. This discrepancy was due to condensation of the gas phase at the interface. This is allowed within the formalism we used because the equation of state describes a liquid in equilibrium with its own vapour. The discrepancy can be minimised by increasing the liquid gas density ratio.

We then considered a binary fluid, comprising two different types of particles, where evaporation and condensation is not permitted. Very good agreement was achieved with the theoretical expression, as long as the dynamic contact angle was used in the fit and the dissipation in the gas phase was taken into account. We argued that the dynamic contact angle differed from the equilibrium value because of dissipation of energy from the flow field near to the meniscus. We further found that the standard BGK approximation does not reproduce the contact angle correctly, due to spurious effects described in section 2.2.3. The advancing angle obtained using the standard BGK approximation is always higher than that obtained from

the multiple relaxation time lattice Boltzmann simulations. Since the speed of capillary filling depends on θ_A , capillary filling is considerably slower in the standard BGK method.

Our results for the patterned channels suggest strategies that could be used to design surface patterning on microfluidics channels. To speed up capillary filling, one should introduce roughness which is elongated in the direction of the flow. However, additional surface area will only speed up filling if pinning is avoided by, for example, avoiding sharp edges and making the post inclinations as gentle as possible. Furthermore, any surface patterning should neither be too dense nor too large to minimise dissipation. Random arrangement of the posts may also be used to avoid cooperative interface pinning effect. Finally, the intrinsic contact angle of the materials $\theta_e \lesssim 60^\circ$ for capillary filling down a rough channel. These results are consistent with recent findings by Kohonen [128], where he found that the walls of the tracheids in the dry-habitat species are typically rougher than those in wet-habitat species, and with $\theta_e \sim 40^\circ$. Moreover, the set of design principles we describe above may help explain why certain types of wall sculpturing, such as helical thickening [129] found on tree capillaries, are more common than others.

CHAPTER 7

Concluding Remarks

“When you are solving a problem, don’t worry.

*Now, after you have solved the problem,
then that’s the time to worry.”*

- Richard Feynman

In this chapter, we shall comment on several recurrent topics that form the backbone of the thesis. We shall discuss the successes, failures, and challenges within each theme.

Throughout the thesis, we have used lattice Boltzmann simulations as a numerical method of choice for simulating wetting phenomena. By comparing the numerical results with experiments and theory, a quantitative match can be obtained when we are considering the static properties of the systems. For the dynamical behaviour, however, comparisons with experiments so far have shown that, while the dynamic pathways are correct, interfaces in the liquid gas model move too quickly. This is mainly caused by the evaporation-condensation mechanism that controls the dynamics of the three phase contact line. As a result, drops slide instead of roll, drops spread on a surface too quickly, and capillary filling scales linearly rather than reproducing the Washburn’s law.

The approach we have taken to remedy this problem is to model the system as a binary fluid. Because the particles are now of different types, the evaporation-condensation mechanism is no longer possible. The contact line moves via diffusion and the effective slip length is controlled by a parameter called the mobility. Using the binary model, we are able to reproduce the Washburn’s Law and we are also able to simulate drops that roll instead of sliding.

Modelling the system as a binary fluid has one additional complication. To correctly simulate the dynamics of a liquid-gas interface it is necessary for the liquid to be much more

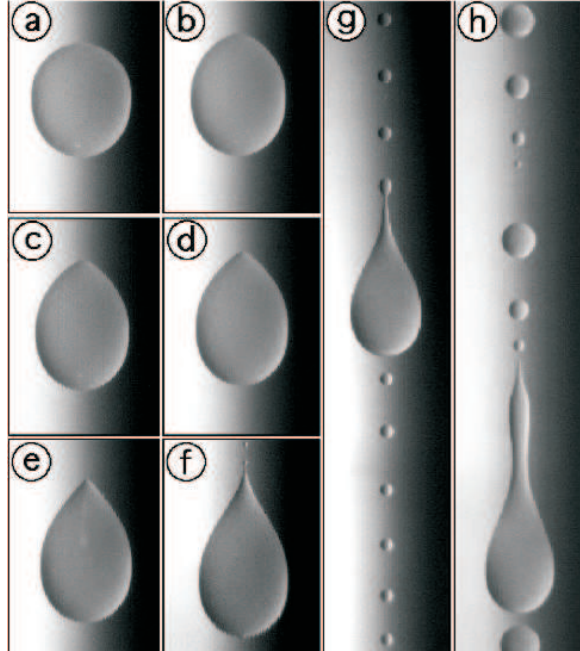


Figure 7.1: Different shapes of a drop running down a plate when the capillary number is increased. (a-b) Rounded drops. (c-e) Corner drops. (f-h) Pearling drops. The figures are taken from [130].

viscous than the gas. The standard BGK approximation is not adequate to model a viscosity difference and we need to apply an algorithm based on the multiple relaxation time lattice Boltzmann method to correctly captures the physics of the problem. For situations where inertia is important, we have also proposed a new binary liquid gas model, which allows both viscosity and density ratios to be simulated.

An important next step in the development of the binary model is to reproduce the liquid gas model results presented in chapter 3 in order to check whether this approach is able to match the experimental results without the need of time rescaling. We expect the contact line dynamics to play an important role in this problem, and matching simulation and experimental results will bring us to a better understanding of the role of the mobility parameter in our model. Once this comparison is performed, the potential for future applications is vast. For example, one potentially exciting problem is the formation of corners, cusps, and pearls in running liquid drops [130,131]. Limat and co-workers have shown that, when small drops slide down a partially wetting substrate, their shapes bifurcate depending on their capillary number Ca . This is shown in Fig. 7.1. At low Ca , the contact line is smooth and rounded, while it forms a corner at the trailing edge and exhibits a pearling instability when the Ca is increased.

Real surfaces are neither smooth nor chemically homogeneous. As a result of heterogeneities, the contact line can be pinned and the contact angle is not single-valued, leading to contact angle hysteresis. Understanding contact angle hysteresis quantitatively is still an open problem, because it is highly dependent on the details of the surface itself and any average over the area of the patterning or over the angle along the contact line is not sufficient to predict the hysteretic properties of the surface. Furthermore, due to the distorted drop shape, the advancing and receding contact angles depend on the direction in which the measurement is taken.

Nonetheless, despite these complications, we are still able to understand several interesting hysteretic phenomena. We argued, based on Gibbs' criterion [111], why suspended drops on superhydrophobic surfaces have much lower contact angle hysteresis than collapsed drops. The high receding angle of suspended drops also turns out to be important for explaining why spontaneous collapse only occurs when the drops span a very small number of posts: the depinning of the receding contact line often preempts the penetration of the liquid gas interface down the posts. Finally, we showed that contact line pinning plays an important role in the way a fluid penetrates a microchannel. In particular, ridges perpendicular to the flow direction introduce pinning which slows, or sometimes prevents, filling, whereas ridges parallel to the flow provide extra surface which may enhance filling.

We are continuing to work in this area. One of the most important challenges in current research into superhydrophobicity is to find ways to induce reversible transitions between the Wenzel and Cassie-Baxter states. The Cassie-Baxter state is appealing due to its high contact angle, low contact angle hysteresis and high mobility. Potential applications range from reducing drag in microfluidics and lab-on-a-chip devices to liquid-based cooling of micro-electronics. The Wenzel state, on the other hand, may be useful for a different set of applications, due to its high contact angle and high adhesive properties. Because the two states have different properties, it would be useful to be able to switch from one state to the other at will. This is normally not possible because of the high energy barrier that opposes the transition from the Wenzel to the Cassie-Baxter state. However, our preliminary results suggest that when a drop is placed on top of a grooved surface, because there is no contact line pinning (and hence hysteresis) in the direction parallel to the grooves, the drop is able to undergo a (reversible) transition from the Wenzel to the Cassie-Baxter state by continuously wetting or dewetting the grooves.

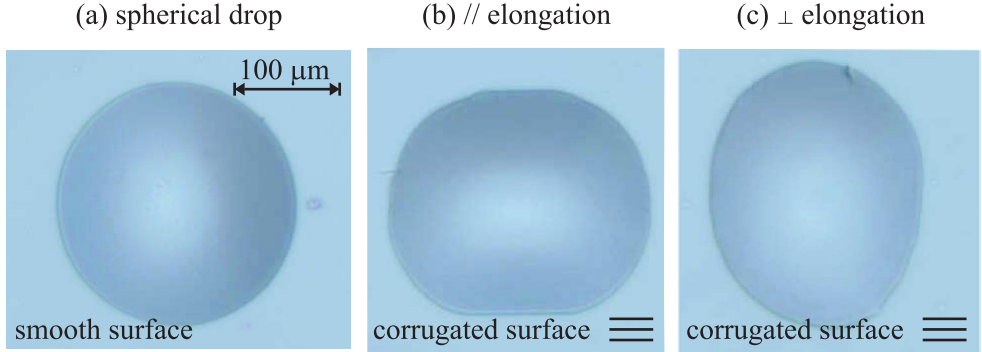


Figure 7.2: Typical drop shape observed in experiments when (a) there is no surface patterning, (b) the drop is sprayed onto the surface and spreads, and (c) the drop is stamped onto the surface and dewets [132]. Although not visible in this image, the surfaces of (b) and (c) were patterned with sub micron-scale ridges. Here the ridges are oriented in the horizontal direction.

The dynamics of drops moving across superhydrophobic surfaces is itself still not fully understood. It is commonly observed that suspended drops move very easily and quickly on superhydrophobic surfaces. This can be explained by the low contact angle hysteresis. However, it is less clear whether the drops' high velocity is primarily caused by their large contact angle or a large slip length. Previous work by Dupuis and Yeomans [50] suggests that large contact angle is the dominant effect, but their liquid gas model suffers from the evaporation-condensation problem, and it would be interesting to revisit the problem using the binary or the binary liquid gas model. It will also be interesting to study how the velocity of drops on superhydrophobic surfaces compares to equivalent liquid marbles [24] moving across a smooth surface.

Another interesting avenue for future research is to understand how surface heterogeneities influence spreading dynamics on a surface, especially when contact line pinning is strong and the surface patterning is anisotropic. When pinning is strong, the surface patterning is reflected in the shape of the drop, even when its size is an order of magnitude smaller than the drop size. This may be seen, for example, when a drop spreads on chemically striped surfaces, or, as shown in Fig. 7.2, on grooved surfaces. The typical final drop shape is no longer spherical and surprisingly, the elongation direction can be either parallel or perpendicular to the direction of the grooves, depending on the initial drop conditions [132]. When the contact line is advancing, the drop is found to be elongated parallel to the grooves. On the other hand, when the contact line is receding, the drop is elongated perpendicular to the grooves.

The anisotropy in the drop shapes may be exploited for microfluidic applications. For example, we showed in chapter 3 how it can be used to control the size and polydispersity

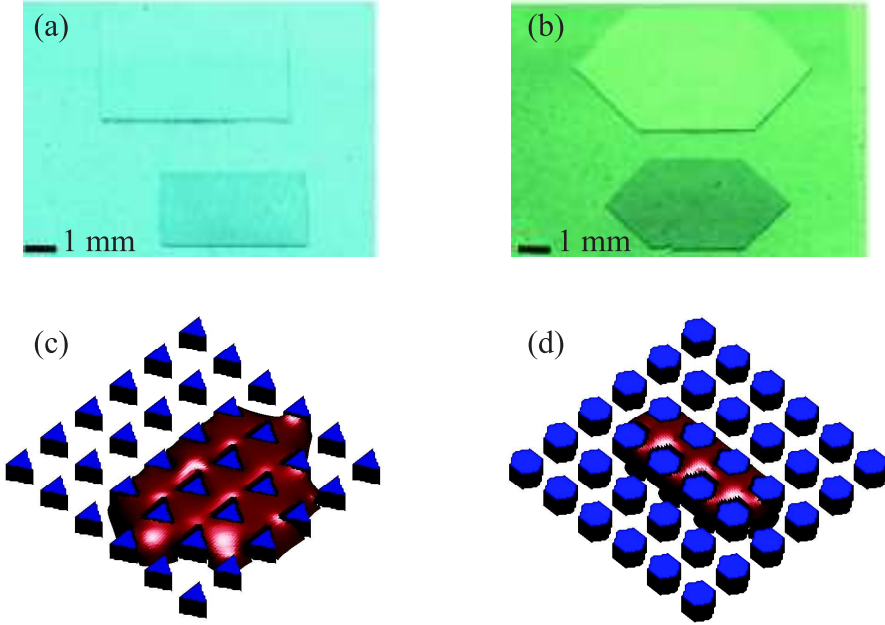


Figure 7.3: Different drop shapes depending on (a-b) the arrangement and (c-d) the shape of the posts. (a) Cylindrical posts which form a square lattice. (b) Cylindrical posts which form a hexagonal lattice. (c) Triangular posts on a square lattice. (d) Hexagonal posts on a square lattice. The figures in panels (a) and (b) are experimental results presented in [133], while those in panels (c) and (d) are simulations kindly provided by Matthew Blow.

of micron-scale drops. Courbin *et al.* [133] have recently demonstrated that the shape of spreading drops on surfaces patterned by posts can be selected by choosing the appropriate topographic features and contact angle. Experimental and numerical examples which illustrate how the shape of the drop depends on the shape and arrangement of the posts are shown in Fig. 7.3.

We are also currently simulating the ratchet effect observed on butterfly wings. Zheng *et al.* [10] showed that butterfly wings act as fluidic diodes where liquid drops roll easily in one direction and pin strongly when moving in the opposite direction. Our results so far indicate that, when a hydrophobic surface is patterned with ratchets, the shape of the liquid gas interface spanning the posts becomes asymmetric and this, in return, influences the contact line pinning and hysteresis. In the ‘easy’ direction, contact line pinning is weak and the drops behave in a way analogous to Cassie-Baxter drops, while in the ‘hard’ direction, contact line pinning is strong and they behave as collapsed drops. Furthermore, it is interesting to note that the ‘easy’ direction is opposite to that observed in section 6.3.1, where we consider capillary filling in ratcheted channels. This is because capillary penetration is influenced by the pinning of the advancing contact line, whereas in this case, it is the pinning of the receding contact

line which plays the dominant role. This sums up the main reason why drop morphologies on patterned surfaces are very rich. They occur not only because the contact line movement over the surface is anisotropic, but also because the motion of the advancing and receding contact lines is asymmetric.

Epilogue

Finally, we can only hope that this thesis has shown glimpses of how exciting the field of wetting is. Wetting phenomena are of great importance in nature and technology. At large scales, they play an important role in, for example, oil recovery and painting. On a smaller scale, which is the subject of this thesis, solutions based on the physics of wetting have been proposed to solve technological problems in microfluidics and inkjet printing, with many of the inspirations coming from nature. Wetting phenomena truly are an exciting playground where physics, chemistry, biology and engineering intersect.

REFERENCES

- [1] T. Young, “An Essay on the Cohesion of Fluids”, *Philos. Trans. R. Soc. London* **95**, 65 (1805).
- [2] P. Laplace, “Oeuvres complètes de Laplace”, *Paris : Gauthier-Villars* (1878).
- [3] W. Ming, D. Wu, R. van Benthem, and G. de With, “Superhydrophobic Films from Raspberry-Like Particles”, *Nano Lett.* **5**, 2298 (2005).
- [4] L. Zhu, Y. Xiu, J. Xu, P. Tamirisa, D. Hess, and C. Wong, “Superhydrophobicity on Two-Tier Rough Surfaces Fabricated by Controlled Growth of Aligned Carbon Nanotube Arrays Coated with Fluorocarbon”, *Langmuir* **21**, 11208 (2005).
- [5] X. Gao, X. Yao, and L. Jiang, “Effects of Rugged Nanoprotusions on the Surface Hydrophobicity and Water Adhesion of Anisotropic Micropatterns”, *Langmuir* **23**, 4886 (2007).
- [6] J. Leopoldes, A. Dupuis, D. Bucknall, and J. Yeomans, “Jetting Micron-Scale Droplets onto Chemically Heterogeneous Surfaces”, *Langmuir* **19**, 9818 (2003).
- [7] D. Quere, “Rough Ideas on Wetting”, *Physica A* **313**, 32 (2002).
- [8] W. Barthlott and C. Neinhuis, “Purity of the Sacred Lotus, or Escape from Contamination in Biological Surfaces”, *Planta* **202**, 1 (1997).
- [9] X. Gao and L. Jiang, “Water-Repellent Legs of Water Striders”, *Nature* **432**, 36 (2004).
- [10] Y. Zheng, X. Gao, and L. Jiang, “Directional Adhesion of Superhydrophobic Butterfly Wings”, *Soft Matter* **3**, 178 (2007).
- [11] A. Cassie and S. Baxter, “Wettability of Porous Surfaces”, *Trans. Faraday Soc.* **40**, 546 (1944).
- [12] J. Bico, C. Marzolin, and D. Quere, “Pearl Drops”, *Europhys. Lett.* **47**, 220 (1999).
- [13] A. Tuteja, W. Choi, M. Ma, J. Mabry, S. Mazzella, G. Rutledge, G. McKinley, and R. Cohen, “Designing Superoleophobic Surfaces”, *Science* **318**, 1618 (2007).
- [14] L. Cao, T. Price, M. Weiss, and D. Gao, “Super Water- and Oil-Repellent Surfaces on Intrinsically Hydrophilic and Oleophilic Porous Silicon Films”, *Langmuir* **24**, 1640 (2008).
- [15] R. Wenzel, “Resistance of Solid Surfaces to Wetting by Water”, *Ind. Eng. Chem.* **28**, 988 (1936).

- [16] B. He, N. Patankar, and J. Lee, “Multiple Equilibrium Droplet Shapes and Design Criterion for Rough Hydrophobic Surfaces”, *Langmuir* **19**, 4999–5003 (2003).
- [17] C. Cottin-Bizonne, C. Barentin, E. Charlaix, L. Bocquet, and J. Barrat, “Dynamics of Simple Liquids at Heterogeneous Surfaces: Molecular-Dynamics Simulations and Hydrodynamic Description”, *Eur. Phys. J. E* **15**, 427 (2004).
- [18] M. Sbragaglia, R. Benzi, L. Biferale, S. Succi, and F. Toschi, “Surface Roughness-Hydrophobicity Coupling in Microchannel and Nanochannel Flows”, *Phys. Rev. Lett.* **97**, 204503 (2006).
- [19] P. Joseph, C. Cottin-Bizonne, J. Benoit, C. Ybert, C. Journet, P. Tabeling, and L. Bocquet, “Slippage of Water Past Superhydrophobic Carbon Nanotube Forests in Microchannels”, *Phys. Rev. Lett.* **97**, 156104 (2006).
- [20] C. Ybert, C. Barentin, C. Cottin-Bizonne, P. Joseph, and L. Bocquet, “Achieving Large Slip with Superhydrophobic Surfaces: Scaling Laws for Generic Geometries”, *Phys. Fluids* **19**, 123601 (2007).
- [21] J. Ou and J. Rothstein, “Direct Velocity Measurements of the Flow Past Drag-Reducing Ultrahydrophobic Surfaces”, *Phys. Fluids* **17**, 103606 (2005).
- [22] C. Ishino, K. Okumura, and D. Quere, “Wetting Transitions on Rough Surfaces”, *Europhys. Lett.* **68**, 419 (2004).
- [23] N. Patankar, “Transition Between Superhydrophobic States on Rough Surfaces”, *Langmuir* **20**, 7097 (2004).
- [24] D. Quere, “Non-Sticking Drops”, *Rep. Prog. Phys.* **68**, 2495 (2005).
- [25] D. Jacqmin, “Contact-Line Dynamics of a Diffuse Fluid Interface”, *J. Fluid Mech.* **402**, 57 (2000).
- [26] P. Seppecher, “Moving Contact Lines in the Cahn-Hilliard Theory”, *Int. J. Eng. Sci.* **34**, 977 (1996).
- [27] A. Briant, A. Wagner, and J. Yeomans, “Lattice Boltzmann Simulations of Contact Line Motion. I. Liquid-Gas Systems”, *Phys. Rev. E* **69**, 031602 (2004).
- [28] A. Briant and J. Yeomans, “Lattice Boltzmann Simulations of Contact Line Motion. II. Binary Fluids”, *Phys. Rev. E* **69**, 031603 (2004).
- [29] R. Cox, “The Dynamics of the Spreading of Liquids on a Solid Surface. Part 1. Viscous Flow”, *J. Fluid Mech.* **168**, 169 (1986).
- [30] C. Huh and L. Scriven, “Hydrodynamic Model of Steady Movement of a Solid/Liquid/Fluid Contact Line”, *J. Colloid Interf. Sci.* **35**, 85 (1971).
- [31] T. Qian, X. Wang, and P. Sheng, “A Variational Approach to Moving Contact Line Hydrodynamics”, *J. Fluid Mech.* **564**, 333 (2006).
- [32] J. Yeomans, “Mesoscale simulations: Lattice Boltzmann and Particle Algorithms”, *Physica A* **369**, 159 (2006).

- [33] C. Denniston, D. Marenduzzo, E. Orlandini, and J. Yeomans, “Lattice Boltzmann Algorithm for Three-Dimensional Liquid-Crystal Hydrodynamics”, *Philos. Trans. R. Soc. A* **362**, 1745 (2004).
- [34] K. Furtado and J. Yeomans, “Lattice Boltzmann Simulations of Phase Separation in Chemically Reactive Binary Fluids”, *Phys. Rev. E* **73**, 066124 (2006).
- [35] K. Good, O. Kuksenok, G. Buxton, V. Ginzburg, and A. Balazs, “Effect of Hydrodynamic Interactions on the Evolution of Chemically Reactive Ternary Mixtures”, *J. Chem. Phys.* **121**, 6052 (2004).
- [36] A. Ladd and R. Verberg, “Lattice-Boltzmann Simulations of Particle-Fluid Suspensions”, *J. Stat. Phys.* **104**, 1191 (2001).
- [37] S. Succi, “The Lattice Boltzmann Equation for Fluid Dynamics and Beyond”, *Oxford: Oxford University Press* (2001).
- [38] M. Swift, E. Orlandini, W. Osborn, and J. Yeomans, “Lattice Boltzmann Simulations of Liquid-Gas and Binary Fluid Systems”, *Phys. Rev. E* **54**, 5041 (1996).
- [39] M. Swift, W. Osborn, and J. Yeomans, “Lattice Boltzmann Simulation of Nonideal Fluids”, *Phys. Rev. Lett.* **75**, 830 (1995).
- [40] X. Shan and H. Chen, “Lattice Boltzmann Model For Simulating Flows with Multiple Phases and Components”, *Phys. Rev. E* **47**, 1815 (1993).
- [41] V. Kendon, M. Cates, I. Pagonabarraga, J. Desplat, and P. Bladon, “Inertial Effects in Three-Dimensional Spinodal Decomposition of a Symmetric Binary Fluid Mixture: a Lattice Boltzmann Study”, *J. Fluid Mech.* **440**, 147 (2001).
- [42] J. Cahn, “Critical-Point Wetting”, *J. Chem. Phys.* **66**, 3667 (1977).
- [43] C. Pooley and K. Furtado, “Eliminating Spurious Velocities in the Free-Energy Lattice Boltzmann Method”, *Phys. Rev. E* **77**, 046702 (2008).
- [44] R. Benzi, L. Biferale, M. Sbragaglia, S. Succi, and F. Toschi, “Mesoscopic Modeling of a Two-Phase Flow in the Presence of Boundaries: The Contact Angle”, *Phys. Rev. E* **74**, 021509 (2006).
- [45] J. Zhang and D. Kwok, “Contact Line and Contact Angle Dynamics in Superhydrophobic Channels”, *Langmuir* **22**, 4998 (2006).
- [46] J. Hyvaluoma, A. Koponen, P. Raiskinmaki, and J. Timonen, “Droplets on Inclined Rough Surfaces”, *Eur. Phys. J. E* **23**, 289 (2007).
- [47] A. Wagner and C. Pooley, “Interface Width and Bulk Stability: Requirements for the Simulation of Deeply Quenched Liquid-Gas Systems”, *Phys. Rev. E* **76**, 045702 (2007).
- [48] Z. Guo, C. Zheng, and B. Shi, “Discrete Lattice Effects on the Forcing Term in the Lattice Boltzmann Method”, *Phys. Rev. E* **65**, 046308 (2002).
- [49] A. Wagner and Q. Li, “Investigation of Galilean Invariance of Multi-Phase Lattice Boltzmann Methods”, *Physica A* **362**, 105 (2006).
- [50] A. Dupuis and J. Yeomans, “Modeling Droplets on Superhydrophobic Surfaces: Equilibrium States and Transitions”, *Langmuir* **21**, 2624 (2005).

- [51] D. d'Humieres, I. Ginzburg, M. Krafczyk, P. Lallemand, and L. Luo, "Multiple-Relaxation-Time Lattice Boltzmann Models in Three Dimensions", *Philos. Trans. R. Soc. A* **360**, 437 (2002).
- [52] K. Premnath and J. Abraham, "Three-Dimensional Multi-Relaxation Time (MRT) Lattice-Boltzmann Models for Multiphase Flow", *J. Comput. Phys.* **224**, 539 (2007).
- [53] R. Du, B. Shi, and X. Chen, "Multi-Relaxation-Time Lattice Boltzmann Model for Incompressible Flow", *Phys. Lett. A* **359**, 564 (2006).
- [54] C. Pooley, H. Kusumaatmaja, and J. Yeomans, "Contact Line Dynamics in Lattice Boltzmann Simulations", *in preparation* (2008).
- [55] P. Lenz and R. Lipowsky, "Morphological Transitions of Wetting Layers on Structured Surfaces", *Phys. Rev. Lett.* **80**, 1920 (1998).
- [56] H. Gau, S. Herminghaus, P. Lenz, and R. Lipowsky, "Liquid Morphologies on Structured Surfaces: From Microchannels to Microchips", *Science* **283**, 46 (1999).
- [57] A. Darhuber, S. Troian, S. Miller, and S. Wagner, "Morphology of Liquid Microstructures on Chemically Patterned Surfaces", *J. Appl. Phys.* **87**, 7768 (2000).
- [58] A. Darhuber and S. Troian, "Principles of Microfluidic Actuation by Modulation of Surface Stresses", *Annu. Rev. Fluid Mech.* **37**, 425 (2005).
- [59] M. Brinkmann and R. Lipowsky, "Wetting Morphologies on Substrates with Striped Surface Domains", *J. Appl. Phys.* **92**, 4296 (2002).
- [60] A. Dupuis, J. Leopoldes, D. Bucknall, and J. Yeomans, "Control of Drop Positioning Using Chemical Patterning", *Appl. Phys. Lett.* **87**, 024103 (2005).
- [61] M. Gleiche, L. Chi, E. Gedig, and H. Fuchs, "Anisotropic Contact-Angle Hysteresis of Chemically Nanostructured Surfaces", *ChemPhysChem* **2**, 187 (2001).
- [62] S. Daniel, M. Chaudhury, and J. Chen, "Fast Drop Movements Resulting from the Phase Change on a Gradient Surface", *Science* **291**, 633 (2001).
- [63] M. Chaudhury and G. Whitesides, "How to Make Water Run Uphill", *Science* **256**, 1539 (1992).
- [64] D. Link, S. Anna, D. Weitz, and H. Stone, "Geometrically Mediated Breakup of Drops in Microfluidic Devices", *Phys. Rev. Lett.* **92**, 054503 (2004).
- [65] T. Squires and S. Quake, "Microfluidics: Fluid Physics at the Nanoliter Scale", *Rev. Mod. Phys.* **77**, 977 (2005).
- [66] O. Kuksenok, D. Jasnow, J. Yeomans, and A. Balazs, "Periodic Droplet Formation in Chemically Patterned Microchannels", *Phys. Rev. Lett.* **91**, 108303 (2003).
- [67] G. Mo and D. Kwok, "Multiple Separation of Self-Running Drops by Pinching a Three-Phase Contact Line", *Appl. Phys. Lett.* **88**, 064103 (2006).
- [68] P. Dittrich and P. Schwille, "An Integrated Microfluidic System for Reaction, High-Sensitivity Detection, and Sorting of Fluorescent Cells and Particles", *Anal. Chem.* **75**, 5767 (2003).

- [69] A. Fu, H. Chou, C. Spence, F. Arnold, and S. Quake, "An Integrated Microfabricated Cell Sorter", *Anal. Chem.* **74**, 2451 (2002).
- [70] M. Wang, E. Tu, D. Raymond, J. Yang, H. Zhang, N. Hagen, B. Dees, E. Mercer, A. Forster, I. Kariv, P. Marchand, and W. Butler, "Microfluidic Sorting of Mammalian Cells by Optical Force Switching", *Nat. Biotechnol.* **23**, 83 (2005).
- [71] K. Ahn, C. Kerbage, T. Hunt, R. Westervelt, D. Link, and D. Weitz, "Dielectrophoretic Manipulation of Drops for High-Speed Microfluidic Sorting Devices", *Appl. Phys. Lett.* **88**, 024104 (2006).
- [72] Y. Tan, J. Fisher, A. Lee, V. Cristini, and A. Lee, "Design of Microfluidic Channel Geometries for the Control of Droplet Volume, Chemical Concentration, and Sorting", *Lab Chip* **4**, 292 (2004).
- [73] M. Pollack, A. Shenderov, and R. Fair, "Electrowetting-Based Actuation of Droplets for Integrated Microfluidics", *Lab Chip* **2**, 96 (2002).
- [74] J. Schwartz, J. Vykovkal, and P. Gascoyne, "Droplet-Based Chemistry on a Programmable Micro-Chip", *Lab Chip* **4**, 11 (2004).
- [75] S. Sugiura, M. Nakajima, S. Iwamoto, and M. Seki, "Interfacial Tension Driven Monodispersed Droplet Formation from Microfabricated Channel Array", *Langmuir* **17**, 5562 (2001).
- [76] A. Ganan-Calvo, "Generation of Steady Liquid Microthreads and Micron-Sized Monodisperse Sprays in Gas Streams", *Phys. Rev. Lett.* **80**, 285 (1998).
- [77] S. Anna, N. Bontoux, and H. Stone, "Formation of Dispersions Using "Flow Focusing" in Microchannels", *Appl. Phys. Lett.* **82**, 364 (2003).
- [78] Y. Xia and G. Whitesides, "Soft Lithography", *Angew. Chem. Int. Ed.* **37**, 551 (1998).
- [79] R. Blossey, "Self-Cleaning Surfaces - Virtual Realities", *Nat. Mater.* **2**, 301 (2003).
- [80] A. Parker and C. Lawrence, "Water Capture by a Desert Beetle", *Nature* **414**, 33 (2001).
- [81] B. Zhao, J. Moore, and D. Beebe, "Pressure-Sensitive Microfluidic Gates Fabricated by Patterning Surface Free Energies Inside Microchannels", *Langmuir* **19**, 1873 (2003).
- [82] B. Zhao, J. Moore, and D. Beebe, "Surface-Directed Liquid Flow Inside Microchannels", *Science* **291**, 1023 (2001).
- [83] K. Handique, D. Burke, C. Mastrangelo, and M. Burns, "Nanoliter Liquid Metering in Microchannels Using Hydrophobic Patterns", *Anal. Chem.* **72**, 4100 (2000).
- [84] L. Fidalgo, C. Abell, and W. Huck, "Surface-Induced Droplet Fusion in Microfluidic Devices", *Lab Chip* **7**, 984 (2007).
- [85] F. Mugele, A. Klingner, J. Buehrle, D. Steinhauser, and S. Herminghaus, "Electrowetting: A Convenient Way to Switchable Wettability Patterns", *J. Phys.: Condens. Matter* **17**, S559 (2005).
- [86] F. Mugele and J. Baret, "Electrowetting: From Basics to Applications", *J. Phys.: Condens. Matter* **17**, R705 (2005).

- [87] A. Alexeev, R. Verberg, and A. Balazs, "Patterned Surfaces Segregate Compliant Microcapsules", *Langmuir* **23**, 983 (2007).
- [88] O. Usta, A. Alexeev, and A. Balazs, "Fork in the Road: Patterned Surfaces Direct Microcapsules to Make a Decision", *Langmuir* **23**, 10887 (2007).
- [89] D. Oner and T. McCarthy, "Ultrahydrophobic Surfaces. Effects of Topography Length Scales on Wettability", *Langmuir* **16**, 7777 (2000).
- [90] L. Gao and T. McCarthy, "The "Lotus Effect" Explained: Two Reasons Why Two Length Scales of Topography are Important", *Langmuir* **22**, 2966 (2006).
- [91] L. Gao and T. McCarthy, "Contact Angle Hysteresis Explained", *Langmuir* **22**, 6234 (2006).
- [92] G. McHale, N. Shirtcliffe, and M. Newton, "Contact-Angle Hysteresis on Superhydrophobic Surfaces", *Langmuir* **20**, 10146 (2004).
- [93] C. Extrand, "Model for Contact Angles and Hysteresis on Rough and Ultraphobic Surfaces", *Langmuir* **18**, 7991 (2002).
- [94] C. Dorrer and J. Ruehe, "Advancing and Receding Motion of Droplets on Ultrahydrophobic Post Surfaces", *Langmuir* **22**, 7652 (2006).
- [95] P. deGennes, "Wetting - Statics and Dynamics", *Rev. Mod. Phys.* **57**, 827 (1985).
- [96] M. Iwamatsu, "Contact Angle Hysteresis of Cylindrical Drops on Chemically Heterogeneous Striped Surfaces", *J. Colloid Interf. Sci.* **297**, 772 (2006).
- [97] R. Johnson and R. Dettre, "Contact-Angle Hysteresis. 3. Study of an Idealized Heterogeneous Surface", *J. Phys. Chem.* **68**, 1744 (1964).
- [98] C. Huh and S. Mason, "Effects of Surface-Roughness on Wetting (Theoretical)", *J. Colloid Interf. Sci.* **60**, 11 (1977).
- [99] R. Dettre and R. Johnson, "Contact Angle Hysteresis. I. Study of an Idealized Rough Surface", *Adv. Chem. Ser.* **43**, 112 (1964).
- [100] A. Marmur, "Contact-Angle Hysteresis on Heterogeneous Smooth Surfaces", *J. Colloid Interf. Sci.* **168**, 40 (1994).
- [101] S. Brandon and A. Marmur, "Simulation of Contact Angle Hysteresis on Chemically Heterogeneous Surfaces", *J. Colloid Interf. Sci.* **183**, 351 (1996).
- [102] J. Oliver, C. Huh, and S. Mason, "Resistance to Spreading of Liquids by Sharp Edges", *J. Colloid Interf. Sci.* **59**, 568 (1977).
- [103] W. Li and A. Amirfazli, "A Thermodynamic Approach for Determining the Contact Angle Hysteresis for Superhydrophobic Surfaces", *J. Colloid Interf. Sci.* **292**, 195 (2005).
- [104] L. Schwartz and S. Garoff, "Contact-Angle Hysteresis on Heterogeneous Surfaces", *Langmuir* **1**, 219 (1985).
- [105] L. Schwartz and S. Garoff, "Contact-Angle Hysteresis and the Shape of the 3-Phase Line", *J. Colloid Interf. Sci.* **106**, 422 (1985).

- [106] J. Joanny and P. deGennes, "A Model for Contact-Angle Hysteresis", *J. Chem. Phys.* **81**, 552 (1984).
- [107] S. Brandon, A. Wachs, and A. Marmur, "Simulated Contact Angle Hysteresis of a Three-Dimensional Drop on a Chemically Heterogeneous Surface: A Numerical Example", *J. Colloid Interf. Sci.* **191**, 110 (1997).
- [108] D. Chatain, D. Lewis, J. Baland, and W. Carter, "Numerical Analysis of the Shapes and Energies of Droplets on Micropatterned Substrates", *Langmuir* **22**, 4237 (2006).
- [109] B. Kong and X. Yang, "Dissipative Particle Dynamics Simulation of Contact Angle Hysteresis on a Patterned Solid/Air Composite Surface", *Langmuir* **22**, 2065 (2006).
- [110] E. Decker, B. Frank, Y. Suo, and S. Garoff, "Physics of Contact Angle Measurement", *Colloids Surf., A* **156**, 177 (1999).
- [111] J. Gibbs, "The Scientific Papers of J. Willard Gibbs", *New York: Dover Publications* (1961).
- [112] G. McHale, S. Aqil, N. Shirtcliffe, M. Newton, and H. Erbil, "Analysis of Droplet Evaporation on a Superhydrophobic Surface", *Langmuir* **21**, 11053 (2005).
- [113] M. Reyssat, J. Yeomans, and D. Quere, "Impalement of Fakir Drops", *Europhys. Lett.* **81**, 26006 (2008).
- [114] R. Kamien, "The Geometry of Soft Materials: A Primer", *Rev. Mod. Phys.* **74**, 953 (2002).
- [115] S. Moulinet and D. Bartolo, "Life and Death of a Fakir Droplet: Impalement Transitions on Superhydrophobic Surfaces", *Eur. Phys. J. E* **24**, 251 (2007).
- [116] D. Bartolo, F. Bouamrire, E. Verneuil, A. Buguin, P. Silberzan, and S. Moulinet, "Bouncing or Sticky Droplets: Impalement Transitions on Superhydrophobic Micropatterned Surfaces", *Europhys. Lett.* **74**, 299 (2006).
- [117] A. Stroock, S. Dertinger, A. Ajdari, I. Mezic, H. Stone, and G. Whitesides, "Chaotic Mixer for Microchannels", *Science* **295**, 647 (2002).
- [118] R. Lucas, "Rate of Capillary Ascension of Liquids", *Kolloid Z.* **23**, 15 (1918).
- [119] E. Washburn, "The Dynamics of Capillary Flow", *Phys. Rev.* **17**, 273 (1921).
- [120] D. Quere, "Inertial Capillarity", *Europhys. Lett.* **39**, 533 (1997).
- [121] F. Diotallevi, L. Biferale, S. Chibbaro, A. Lamura, G. Pontrelli, M. Sbragaglia, S. Succi, and F. Toschi, "Capillary Filling Using Lattice Boltzmann Equations: The Case of Multi-Phase Flows", *arXiv nlin.CG: 0707.0945v1* (2007).
- [122] P. Raiskinmaki, A. Shakib-Manesh, A. Jasberg, A. Koponen, J. Merikoski, and J. Timonen, "Lattice-Boltzmann Simulation of Capillary Rise Dynamics", *J. Stat. Phys.* **107**, 143 (2002).
- [123] S. Levine, J. Lowndes, E. Watson, and G. Neale, "Theory of Capillary Rise of a Liquid in a Vertical Cylindrical Tube and in a Parallel-Plate Channel - Washburn Equation Modified to Account for the Meniscus with Slippage at the Contact Line", *J. Colloid Interf. Sci.* **73**, 136 (1980).

- [124] J. Szekely, A. Neumann, and Y. Chuang, “Rate of Capillary Penetration and Applicability of Washburn Equation”, *J. Colloid Interf. Sci.* **35**, 273 (1971).
- [125] D. Dimitrov, A. Milchev, and K. Binder, “Capillary Rise in Nanopores: Molecular Dynamics Evidence for the Lucas-Washburn Equation”, *Phys. Rev. Lett.* **99**, 054501 (2007).
- [126] F. Diotallevi, L. Biferale, S. Chibbaro, G. Pontrelli, F. Toschi, and S. Succi, “Lattice Boltzmann Simulations of Capillary Filling: Finite Vapour Density Effects”, *arXiv nlin.CG: 0801.4223v1* (2008).
- [127] M. Latva-Kokko and D. Rothman, “Scaling of Dynamic Contact Angles in a Lattice-Boltzmann Model”, *Phys. Rev. Lett.* **98**, 254503 (2007).
- [128] M. Kohonen, “Engineered Wettability in Tree Capillaries”, *Langmuir* **22**, 3148 (2006).
- [129] A. Jeje and M. Zimmermann, “Resistance to Water-Flow in Xylem Vessels”, *J. Exp. Bot.* **30**, 817 (1979).
- [130] T. Podgorski, J. Flesselles, and L. Limat, “Corners, Cusps, and Pearls in Running Drops”, *Phys. Rev. Lett.* **87**, 036102 (2001).
- [131] N. L. Grand, A. Daerr, and L. Limat, “Shape and Motion of Drops Sliding Down an Inclined Plane”, *J. Fluid Mech.* **541**, 293 (2005).
- [132] H. Kusumaatmaja, R. Vrancken, C. Bastiaansen, and J. Yeomans, “Anisotropic drop morphologies on corrugated surfaces”, *Langmuir* **24**, 7299 (2008).
- [133] L. Courbin, E. Denieul, E. Dressaire, M. Roper, A. Ajdari, and H. Stone, “Imbibition by Polygonal Spreading on Microdecorated Surfaces”, *Nat. Mater.* **6**, 661 (2007).